TÉCNICO LISBOA

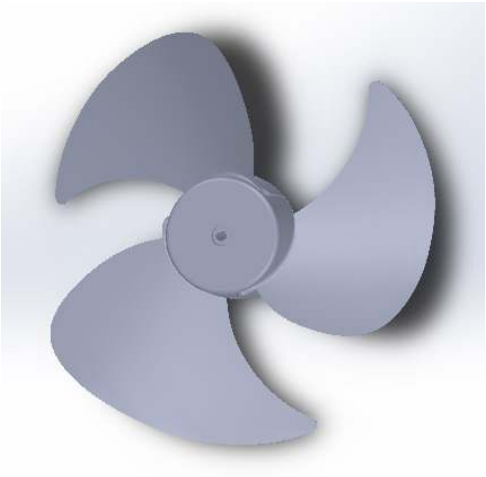

Aeroacoustic Optimization of a Low-Speed Fan

João Miguel Rebelo Branco

Thesis to obtain the Master of Science Degree in

Aerospace Engineering

Supervisor: Prof. André Calado Marta

Examination Committee

Chairperson: Prof. Fernando José Parracho Lau
Supervisor: Prof. André Calado Marta
Member of the Committee: Prof. Luís Manuel Braga da Costa Campos

June 2015

I would like to dedicate this work to all the people who helped me become the person I am today.

Acknowledgments

First of all, I would like to thank Prof. André Calado Marta for his teachings, patience, availability and for being an overall excellent supervisor throughout the development of this thesis. Also, the author would like to express a special appreciation to Prof. Luís Braga Campos for his valuable input and scientific review during various stages of this work. I have to thank the support of my family, especially my mother and my father, for being so supportive and always present for the good and the bad and for making me believe that every goal is attainable, one step at a time. I have also to thank my colleague Simão Santos Rodrigues for his patience and guidance towards the understanding of the original aeroacoustic framework. On a final note, I have to thank my long time teacher, Prof. Cesina Bona, without whom this work and all my present accomplishments would not be possible.

Resumo

O uso de sistemas de ar condicionado registou um crescimento nas últimas décadas devido ao aumento do poder de compra no mundo desenvolvido e ao conforto que estes sistemas proporcionam, tendo aumentado também a consciencialização sobre o seu impacto negativo na saúde pública. Muitos estudos foram realizados para prever e minimizar o ruído das ventoinhas presentes nestes sistemas. Neste trabalho, uma ferramenta aeroacústica baseada na teoria de elementos de pás-momento linear para efeitos de previsão aerodinâmica foi acoplado aos modelos aeroacústicos baseados nos trabalhos de Carolus et al (2007) e Brooks et al (1989) e ao XFOIL para a computação dos parâmetros de camada limite. Esta ferramenta foi validada usando dados experimentais de uma ventoinha axial conhecida e os níveis de ruído de um modelo de ventoinha AC foram determinados. A pá foi parametrizada usando curvas de Bézier para descrever as distribuições de corda e torção e os perfis 2D. Foi realizado um estudo paramétrico onde se estudou o impacto do diâmetro e do número de pás no ruído. O código aeroacústico foi acoplado ao módulo de optimização pyOpt e usando o algoritmo genético NSGA-II, um conjunto de optimizações mono e multi-objectivo foram realizadas na ventoinha de base, usando a corda, torção e curvatura como design variables. Verificou-se uma redução máxima de 4.1% no ruído e um aumento máximo de 5.3% na eficiência da ventoinha.

Palavras-chave: Projecto Aeroacústico, Redução de Ruído, Ar Condicionado, Optimização Multi-Objectivo, Algoritmos Genéticos.

Abstract

The use of air conditioning systems has increased in the recent decades due to the growth of the purchasing power in the developed world and the confort they provide, whereas the awareness regarding the negative health impacts of these systems has also increased. Many studies were conducted to predict and minimize the noise of the fans present in most of these systems. In this work, a noise prediction framework based on the Blade Element Momentum method for aerodynamic prediction was coupled to the empirical aeroacoustic models based on the works of Carolus et al (2007) and Brooks et al (1989) and to XFOIL for boundary layer parameter calculations. This framework was validated against experimental data of a known axial impeller and an existing air conditioning fan model was analyzed and its baseline noise values were characterized. A blade parameterization method was developed where the chord and twist distributions and airfoil sections were described by Bézier curves. A parametric study to determine the impact of fan diameter and blade number on the produced noise was conducted. The aeroacoustic code was coupled to the optimization framework pyOpt, and by using the NSGA-II genetic algorithm, a set of single and multi-objective optimizations, with chord, twist and curvature as design variables were performed on the baseline fan and on the minimum noise fan resultant from the parametric study. The optimal solutions indicated a maximum reduction of 4.1% in noise and a maximum increase of 5.3% in efficiency. Introducing diameter and blade number changes, a significant noise reduction is possible but with a moderate aerodynamic penalty.

Keywords: Aeroacoustic Design, Noise Reduction, Air Conditioning, Multi-objective Optimization, Genetic Algorithms

Contents

List of Tables

List of Figures

Nomenclature

Greek symbols

α	Effective angle of attack
α_{TIP}	Effective angle of attack at blade tip
δ^*	Boundary layer displacement thickness
ξ_1, ξ_3	Coordinates of the rotating system in TI noise
Γ	Attached airfoil circulation
Λ	Turbulence length scale
ω	Rotational speed
ϕ	Inflow angle
Ψ	Trailing edge angle
Θ_e, Ψ_e	Angles used in directivity functions

Roman symbols

a, a'	Axial and radial induction factors
A, B	Spectral shape functions for TBL-TE noise
A_c	Correlation area
$\mathbf{B}(t)$	Bézier curve
$b_{i,n}(t)$	Bernstein polynomials
c	Airfoil chord
c_0	Speed of sound
c_x	Axial flow velocity
$\bar{D}_\ell, \bar{D}_h$	Low and high frequency directivity functions
f	Sound frequency

F Loss factor

G_1 Peak level function for TEB-VS noise

G_2 Spectral shape function for TEB-VS noise

G_3, G_5 Spectral shape functions for LBL-VS noise

G_4 Peak level shape function for LBL-VS noise

h Trailing edge bluntness thickness

K_1, K_2 Amplitude functions for the TBL-TE

L Airfoil section span

ℓ Length of separation due to tip vortex

L_p Sound pressure level

M Mach number

M_{TIP} Tip Mach number

N_{az} Number of azimuthal divisions

N_B Number of blades of the fan

$\mathbf{P}_i$ Bézier control points

PSD_F Force fluctuation on a blade

PSD_{sp} Fluctuating surface pressure distribution

PSD_W Spectral density of acoustic power

Q Torque

r_a Fan radius

r_e Effective observer distance

r_i Hub radius

St Strouhal number

St_{peak} Peak Strouhal number

T Thrust

Tu Turbulence intensity

w_1 Local blade element speed

w_2 Velocity fluctuations due to turbulent eddies

Chapter 1

Introduction

Since the beginning of times, Humans have adapted to the surrounding environment and at the same time changing it in order to suit their basic needs. With the advent of the housing concept, the need for shelter was satisfied, but given the different climates that exist around the world and the relatively narrow spectrum of temperatures required for the normal functioning of the human body, there was always the need to have an efficient way of maintaining a uniform and comfortable room temperature inside of an house, regardless of the outside temperature.

In the 2nd century, a Chinese inventor named Ding Huan built a manually powered rotary fan with a 3 meter diameter in order to recirculate a great volume of air in an attempt to decrease the room temperature [1].

Only sixteen centuries after, in 1758, has Benjamin Franklin taken an interest in the concept of air cooling, when he discovered that it was possible to use the principle of evaporation as a way to rapidly cool an object, using alcohol as a refrigeration fluid and in 1902, Willis Haviland Carrier, considered the father of air conditioning, invented the first modern air conditioning system based on the previously discovered mechanical refrigeration principles by forcing the air to pass through cold coils filled with cold water.

Later on, in 1933, Willis improved his system by adding the following general components which, until today, form the basis of any modern air conditioning system:

- **Evaporator** Set of coils which holds a refrigerant in liquid state and it is evaporated, consuming heat in the process, therefore cooling the air that passes through the coils
- **Condenser** Set of coils holding the same refrigerant but compressed and in vapor state, where it is condensed into the liquid state, releasing heat and heating the surrounding air
- **Expansion valve** It expands the refrigerant that exits the condenser
- **Compressor** It compresses the refrigerant exiting the evaporator

All of the components listed above can be found in Figure 1.1, where a common outdoor AC unit is represented. Besides these components, usually there are also two fans, each one installed near the

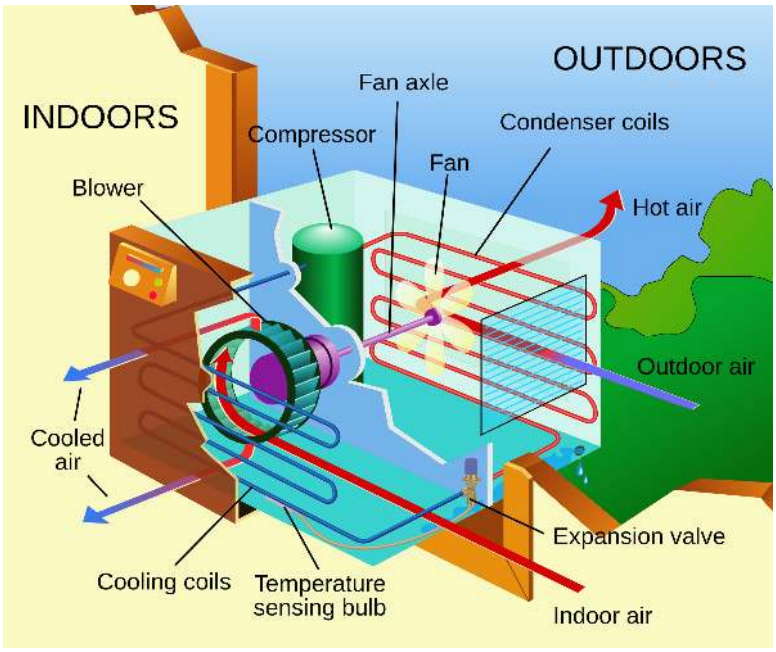

Figure 1.1: Schematics of an outdoor AC unit [2].

condenser and the evaporator in order for the heat exchanges happening in each component to be more efficient. An example of the placement of one of these fans can be found in a real model presented in Figure 1.2.

Since modern systems can also humidify and dehumidify the air, the fans also help in speeding up this process, depending on their speed which is variable according to needs of the user [3]. These fans are called low-speed fans due to their relatively low speed of operation when compared to the fans used in turbofan and turboprop engines, for example. A typical range of tip speeds for these fans is around $35 \sim 45$ m/s. These fans are also known as axial flow fans because the direction of the flow that passes through them is forced to be parallel to the fan rotation axis. The reason is that the design objective of these fans is to have a high flow rate through them and not to create propulsive force like the propellers seen on aircrafts. Another common use for these type of fans (although smaller in diameter) is in computers where the fan is needed in order to cool down the components which can achieve temperatures of 90° C.

1.1 Air Conditioning Worldwide

Although it is recent, this modern system is now used widely around the world and the forecasts of most experts is that the demand for air conditioning is due to increase even more globally. In 2000 the global energy demand for air conditioning was around 300 TWh and it is predicted to increase to 4000 TWh until 2050 and up to 10000 TWh in 2100 [4].

Nowadays, most of this energy is used for heating but due to the growing impact of global warming, there is a tendency for the demand for cooling to catch up with the heating demand, as shown by the prediction that there will be a decrease of 30% in heating demand while an increase of 70% is to be

Figure 1.2: Fan mounted on the external component of an AC system (Copyrighted by Haier).

observed regarding cooling demand.

In Table 1.1, a comparison between heating degree days (HDD) and cooling degree days (CDD) is shown for some major cities and hubs around the world. Cooling degree days are calculated in the following way: the value of 18 C° is subtracted from each day mean temperature and all results that are positive are summed. This final sum is the CDD. The calculations for HDD are the same, except that the mean temperature is now subtracted from the value of 18 C° . This value is used because the mean temperature around the world where it is observed the least consumed energy for climate changes is 18 C° . Therefore, these numbers can be used as a first order indicator of the energy demand for both cases.

1.2 Environmental Impact of Air Conditioning

Given its widespread use and as with most of the mechanical technological advances in the 20^{th} century, it is bound for air conditioning to have an impact in the environment.

One of the main issues is the use of coolants which generally are greenhouse gases and therefore contribute for the global warming effect, gradually making the world unnaturally warm and increasing the energy demand for air conditioning, which will then add even further to the global warming effect, creating a sort of diverging spiral.

There are also some health issues regarding air conditioning, in which the levels of humidity and poor cleaning involved in these systems can promote the development and spread of bacterias, being a potentially hazardous mean of infections. Its excessive use can also cause skin dehydration and pneumonia, if it causes a sudden temperature drop.

One less advertised effect of air conditioning, but not less important, is the noise impact. An air conditioner is a multi-component system and its noise originates mainly from the condenser and the fan. In residential areas, this noise can be a nuisance and if it is too intense, it can have a negative impact on the health of the residents. Given the low speed of the fan, one of the most prominent component

Metropolitan area	CDD	HDD	CDD+HDD	(CDD/(CDD+HDD))*100
Saint Petersburg	73	5028	5101	1
Moscow	138	4668	4806	3
Toronto	259	4059	4318	6
Chicago	461	3610	4071	11
Madras	3954	0	3954	100
Bangkok	3884	0	3884	100
Karachi	3136	631	3767	83
Ho Chi Minh	3745	0	3745	100
Beijing	840	2842	3682	23
Tianjin	965	2676	3641	27
Ahmadabad	3514	14	3528	100
Seoul	746	2706	3452	22
Manila	3438	0	3438	100
Jakarta	3390	0	3390	100
Mumbai	3386	1	3387	100
Philadelphia	686	2644	3330	21
New York	639	2641	3280	19
Hyderabad	3221	2	3223	100
Calcutta	3211	10	3221	100
Delhi	2881	238	3119	92
Lahore	1309	1753	3062	43
Baghdad	2142	884	3026	71
Tehran	1282	1705	2987	43
Wuhan	1277	1679	2956	43
Paris	157	2684	2841	6
Shanghai	1129	1703	2832	40
London	84	2679	2763	3
Osaka	1180	1524	2704	44
Madrid	805	1891	2696	30
Lagos	2653	0	2653	100
Dhaka	2560	0	2560	100
Tokyo	938	1590	2528	37
Miami	2423	83	2506	97
Istanbul	567	1885	2452	23
Guangzhou	2072	377	2449	85
Rio de Janeiro	2401	5	2406	100
Hong Kong	2107	267	2374	89
Shenzhen	2107	267	2374	89
Chongqing	1189	1142	2331	51
Bangalore	2280	1	2281	100
Cairo	1833	424	2257	81
Kinshasa	2098	0	2098	100
Buenos Aires	512	1544	2056	25
Bogotá	0	1787	1787	0
Santiago	290	1481	1771	16
Belo Horizonte	1654	35	1689	98
São Paulo	1187	216	1403	85
Los Angeles	837	516	1353	62
Lima	906	105	1011	90
Mexico City	245	584	829	30

Table 1.1: Comparison between cooling degree days (CDD) and heating degree days (HDD) in the 50 largest metropolitan areas in the world [5].

of its sound is the low-frequency noise, which also comes from traffic, aircraft and industrial machinery. Although little research has been done about this subject, it is a dangerous health hazard and it should be taken seriously, as shown in [6].

1.3 Noise Legislation

Given the hazardous effects of noise, there are laws which define the maximum noise levels allowed in certain areas and in given periods of time along a 24-hour day, although there are not any international noise standards defined. Taking as an example the Portuguese Law, the maximum noise values allowed are presented in Table 1.2. A ”sensitive” zone is defined as a residential, school or hospital area where

Zone	L_{den}(dB(A))	L_n(dB(A))
Mixed	65	55
Sensitive	55	45
Other	63	43

Table 1.2: Maximum noise levels per area in Portuguese territory [7].

normal activities can be easily disturbed by excessive noise whereas a ”mixed” zone is defined as an area where there are simultaneously industrial or large commercial businesses which have more leeway for noise and sectors that belong to the sensitive category. Any zone that does not meet any of the criteria defined above is labeled as ”other”.

L_{den} is defined as a noise indicator or sound pressure level associated to general nuisance and it is given by

$$L_{den} = 10 \log \frac{1}{24} [13 \times 10^{\frac{L_d}{10}} + 3 \times 10^{\frac{L_e+5}{10}} + 8 \times 10^{\frac{L_n+10}{10}}] \quad , \tag{1.1}$$

where L_d, L_e and L_n are the daytime, afternoon and night noise indicators.

The country which consumes more energy for air conditioning is the United States, so much that New York has a specific noise code for air conditioning, where it is stated that a single AC device cannot produce more than 42 dB(A) measured three feet from the noise source and the cumulative noise level of multiple devices cannot exceed 45 dB(A) with the same measuring standards as before [8].

There is also specific air conditioning noise legislation in Canada, also a high AC consuming country, where the noise limits are 45 db(A) and 50 dB(A) for rural and urban areas, respectively. In more noisy areas such as near railway tracks and highways, there is an exceptional limit of 55 db(A) [9].

1.4 Objectives

The main objective of this work is to minimize the noise produced by an existing air conditioning fan, in close collaboration with a world leading air conditioning manufacturer, while maximizing its aerodynamic efficiency by performing an aeroacoustic optimization of the fan blades, with the blade geometry as the driving design variable.

An existing and tested aeroacoustic tool will be adapted to the case in study and used to characterize the initial fan, in order to have a baseline to compare the final results to.

1.5 Thesis Outline

In Chapter 2, some basic aeroacoustic concepts are defined and an extensive overview of the most relevant noise mechanisms in a fan are presented. The numerical models implemented in the aeroacoustic tool and used throughout this work to model the noise mechanisms are also introduced, along with the BEM method to be used for aerodynamic predictions.

In Chapter 3, the characteristics and functioning principles of the custom aeroacoustic tool that will be used are described. The validation of the tool using known data from a typical axial flow fan is presented.

In Chapter 4, an overview of the most common airfoil parametrization methods is done and one is chosen to parametrize the blade airfoils. Also the used 3D parametrization method for building any blade geometry is described.

In Chapter 5, the baseline fan geometry and the process of inputing it in the aeroacoustic tool is defined. Also, the baseline noise levels are characterized and the used final method is explained.

In Chapter 6, a parametric study is conducted to evaluate the impact of fan diameter and blade number on the noise produced.

In Chapter 7, a final aeroacoustic optimization is performed on the baseline fan and on the best case obtained in chapter 6 and the respective results are presented and discussed.

The thesis ends in Chapter 8 with overall conclusions and remarks and comments on future work.

Chapter 2

Fan Aeroacoustics

In this chapter, the concepts of sound and noise are briefly defined and the underlying theory of some of the noise generation mechanisms of low speed fans is presented, along with how the theory will be modeled in the noise prediction tool that will be used. A section detailing the method to predict some aerodynamic parameters is also present.

2.1 Sound and Noise

Sound is a physical phenomena that consists on the propagation of a pressure oscillation through a given medium, consisting of successive cycles of expansion and contraction of air with changes in air density related to the pressure change created by the sound source. The intensity and frequency of these cycles can be sensed and measured in order to characterize the sound, so that sound is modeled as a wave with a given frequency f and velocity v.

Noise is related to the comfort levels of the human ear. If a given sound becomes annoying or repetitive in such a way that causes discomfort or impacts the normal functioning of the human being in its environment, then that sound is defined as noise. Noise is present in most of the everyday appliances such as computer fans, air conditioning systems and in situations like traffic.

2.2 Sound Pressure Level and Noise Scales

The spectrum of pressure disturbances detectable as sound by the human ear is very wide, therefore it was required to define a scale that characterizes the intensity of sound within a more practical range of values.

Knowing that the human perceived intensity is not linear, such that a sound with double the pressure disturbance will not *feel* two times more intense, this scale was defined logarithmically and it was named

Sound Pressure Level (SPL). SPL is defined by equation (2.1) [10] and it is expressed in decibels (dB)

$$SPL = 10 \log_{10} \left(\frac{p_{rms}^2}{p_{ref}^2} \right) \quad , \tag{2.1}$$

where p_{ref} is a pressure reference value, usually defined at 2×10^{-5} Pa, and p_{rms}^2 is the sound pressure root mean square defined by

$$p_{rms}^2 = \lim_{t \to \infty} \frac{1}{t} \int_0^t p^2(t) \mathrm{d}s \quad . \tag{2.2}$$

Therefore, from equation (2.1), it is possible to observe that if the intensity of a sound is doubled, its SPL increases by 3 dB.

In order to make an assessment on typical values in this scale, the sound pressure levels for some example sounds are presented in table 2.1.

Sound Pressure Level (dB)	Sound Examples
10	Human breathing (3m away)
20	Falling leaf
30	Empty cinema room
60	Conversation between two people
70	Urban traffic
80	Vacuum cleaner
90	Factory work environment
100	Pneumatic hammer (2m away)
110	Motorcycle engine revving(5m away)
120	Rock concert
130	Pain threshold
140	Jet engine (3m away)

Table 2.1: Examples of sounds and their respective SPL [10].

The Sound Pressure Level quantifies objectively the intensity of a sound, but it does not account for the impact of sound frequency in its perception by the human ear. A 100 Hz sound will be perceived with an intensity level 20 dB lower than its original intensity level while the perceived intensity of a 1000 Hz sound will remain the same. To account for this effect, the A-,B- and C-weightings were created in order to correct the original SPL scale and to have an objective way to measure how tones of sounds with the same intensity are perceived differently. The relation between the sound frequency and the change in intensity is shown in figure 2.1. The A-weighting is the most commonly used, being suited for low to medium levels, while the B- and C-weighting are used more for higher intensity levels. When the A-weighting correction is applied, the sound pressure level is measured in dB(A).

2.3 Tonal and Broadband Noise

In common knowledge, it is usual to associate high frequency sound to high pitched tones, such as a whistle and low frequency sound to low pitched tones, such as a drum beat. Although this association is not wrong, it is only completely true for a pure tone, which is a sound consisting in a pure sinusoidal wave with a fixed frequency.

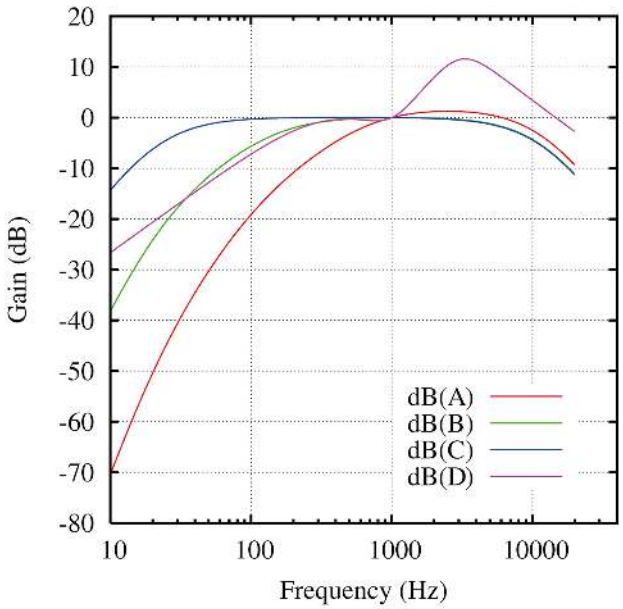

Figure 2.1: Representation of the different noise scale corrections.

Pure tones are produced only artificially by electronic oscillators and do not exist in Nature. In reality, all the sounds that we know are a complex combination of sound components of various frequencies and intensities which compose what is known as the sound spectrum. An example of a spectrum is shown in figure 2.2. It is common to define the range for the frequency axis in a spectrum plot between 100 Hz and 16$\sim$17 kHz, since the spectrum of human audible frequencies is comprised between 20 Hz and 20 kHz, but as it can be seen in figure 2.1 considering A-weighting, the ear is less sensitive to sounds with frequency less than 100 Hz and higher than 12 kHz.

After a sound spectrum is obtained, there may exist some spikes in certain frequency bands that stand out from the rest of the spectrum. These spikes are referred to as tonal noise (or narrow band noise) and if they have fundamental high relative amplitude, the overall noise may be dominated by tonal noises. In most cases, tonal noises are harmonic, consisting of a fundamental frequency f, which is the frequency where the first spike is detected, plus the harmonics are multiples of f usually with smaller amplitude than the fundamental, but nonetheless higher when compared to the rest of the spectrum, in frequencies of $2f$,$3f$, etc.

What until now has been referred as the rest of the spectrum, is called broadband noise, because it is not defined in a single frequency band like tonal noise, being instead a distributed noise along the frequency spectrum. Good examples for broadband noise are the wind noise, traffic noise or any kind of background noise. The distinction between tonal and broadband noise is also represented in figure 2.2.

2.4 Fan Noise Mechanisms

The two major sources of noise in a low speed fan, as with any other fan, are mechanical and aeroacoustic sources, as shown in figure 2.3.

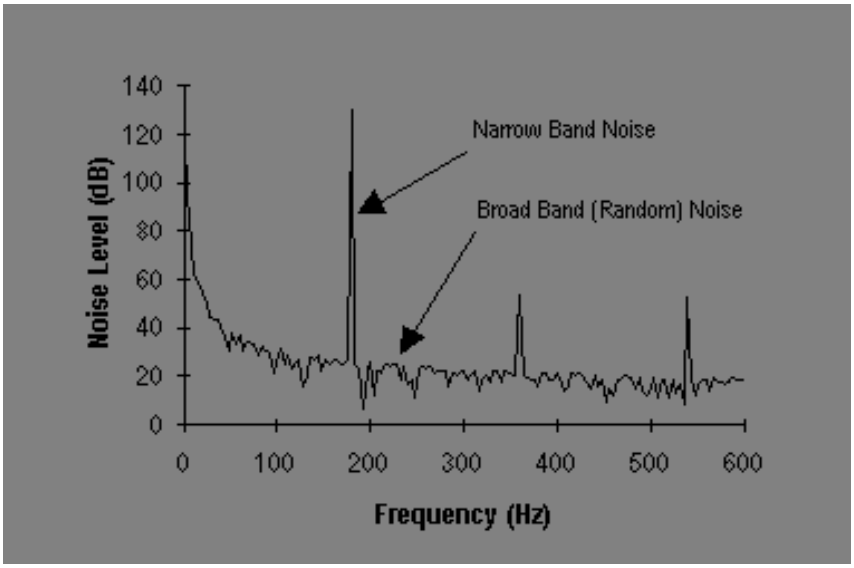

Figure 2.2: Frequency spectrum of a sound [11].

2.4.1 Mechanical Noise

As with any mechanical system with moving parts, the dynamic interaction between each component creates noise. In an air conditioning system, this noise derives mainly from the engine and driver belts responsible for the motion of the fan and also from the compressor [12].

Despite these sources, modern systems have very efficient noise reduction techniques and with modern manufacturing materials and technology, mechanical noise in fans is just a small fraction of the total noise.

2.4.2 Aeroacoustic Noise

Aeroacoustic noise is the major source for the total noise of a low speed fan, with the fan geometry (e.g. airfoils and blade twist) as the main design driver which has an impact on reducing this type of noise. Aeroacoustic noise in fans can be divided in three groups: low frequency noise, turbulent inflow noise and airfoil self-noise.

Low frequency noise is related to the Blade Passing Frequency or BPF of the fan, which will be defined later in this section. Turbulent inflow noise is created when there is an interaction between the airfoil and the incoming turbulent flow and airfoil self-noise is a consequence of the interaction between the self-produced boundary layer and wake and the airfoil itself. There are five known self-noise mechanisms which are Trailing Edge Bluntness Vortex Shedding (TEB-VS), Tip Vortex Formation (TVF), Separation/Stall, Laminar Boundary Layer Vortex Shedding (LBL-VS) and Turbulent Boundary Layer Trailing Edge (TBL-TE).

Low Frequency Noise

Whenever a rotating body, such as the blade of a fan, rotates at a constant angular velocity in an air flow, it experiences aerodynamic forces. In turn, the reaction forces from the rotating body accelerate

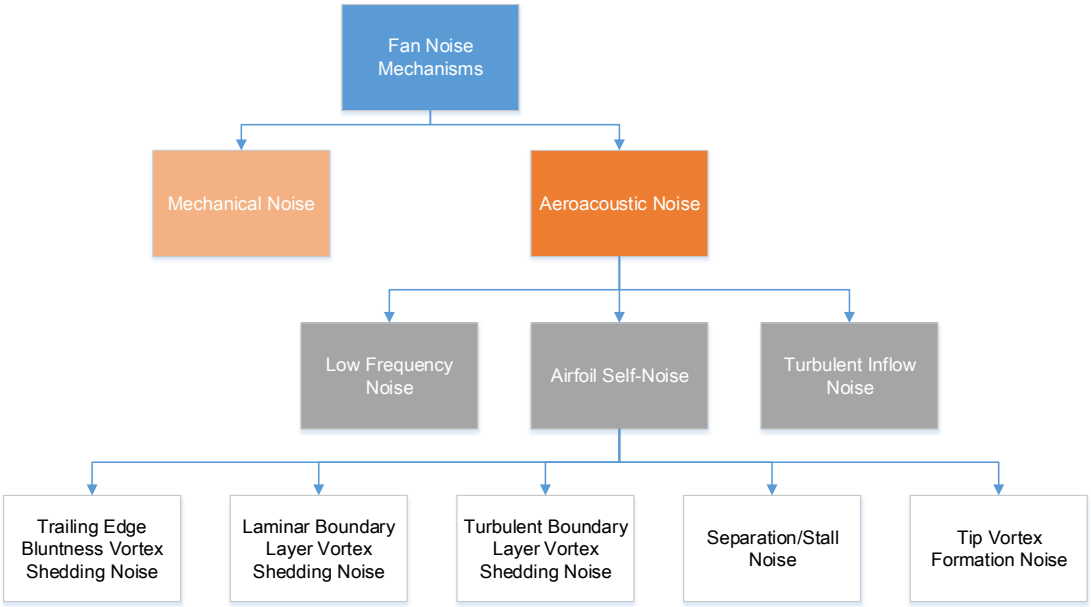

Figure 2.3: Fan noise sources.

the surrounding air, which generates pressure disturbances and therefore produces sound [13].

If a fixed point in space is considered, the sound produced by a rotating blade can be thought out as an impulse in the air located in that point, whenever the blade passes through that point. So, if the number of times a blade passes through a given point is increased, the impulses and the produced sound also increases, being generated a sound wave with a frequency equal to the number of impulses created in a second.

In a fan or any rotor-like mechanism, this phenomena is characterized by the Blade Passing Frequency (BPF) which translates the amount of times that all the blades pass through a generic point in a second, such that a fan with an high rotating speed and number of blades will have an high BPF. BPF is given by

$$BPF = \frac{NZ}{60} \quad , \tag{2.3}$$

with N as the fan rotating speed in RPM and Z as the number of blades.

For low speed fans, this frequency is usually very low, between 40 and 100 Hz, due to the low rotating speed which turns the BPF noise or low frequency noise, in this case, almost inaudible due to belonging in the low end of the human audible frequency spectrum. Therefore, although it is a tonal noise, low frequency noise in low speed fans becomes almost irrelevant.

Trailing Edge Bluntness Vortex Shedding Noise

Although the trailing edge of an airfoil is idealized as being just a point where the pressure and suction surfaces connect in the rear end, in reality there is always an edge with finite thickness in the end of the airfoil, due to manufacturing constraints.

This trailing edge with thickness creates a coherent vortex shedding, also known as a Von Kármán vortex sheet [14], due to the differential of pressure between the two surfaces of the airfoil. As these vortexes are shed, a varying pressure fluctuation is generated along the trailing edge, producing a radiating noise of tonal nature of varying discrete frequencies, which is called Trailing Edge Bluntness Vortex Shedding noise.

The noise produced by this mechanism is correlated to the trailing edge thickness and angle, being extremely sensitive to changes in any of these variables, such that one effective method of reducing this noise is to minimize the thickness and smooth the trailing edge angle as physically possible. However, it is important to notice that any change in the trailing edge will affect the lift produced by the airfoil, since a variation on the trailing edge thickness will impact the circulation that relates to the lift as

$$L = -\rho U \Gamma \quad , \tag{2.4}$$

where ρ is the air density, U is the air speed and Γ is the attached circulation in the airfoil. Therefore, there is a compromise to be had between the reduction of the noise produced by this mechanism and the impact in the overall lift. A schematic representation of this phenomenon is presented in figure 2.4.

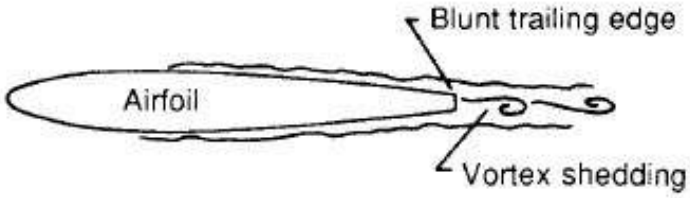

Figure 2.4: Trailing edge bluntness noise [15].

Tip Vortex Formation Noise

In a way analogous to the Trailing Edge Bluntness noise, Tip Vortex Formation noise is a consequence of the shedding of vortexes in the tip of the blade due to the pressure difference between the upper and lower surfaces. The interaction between these vortexes and the blade tip produces a pressure fluctuation which radiates a broadband noise [15]. This noise mechanism is highly sensitive to the topology of the tip geometry. A schematic representation of this noise producing mechanism is presented in figure 2.5.

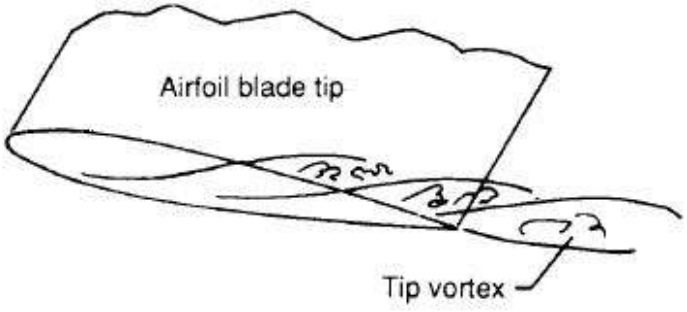

Figure 2.5: Tip vortex noise [15].

Separation/Stall Noise

When the angle of attack of an airfoil is very high, the flow separates from the suction surface, creating a zone with highly recirculating and unsteady flow containing turbulent eddies. When these eddies interact with the airfoil wake, a broadband noise is produced with the name of Separated Stall noise [15]. A schematic representation of this noise producing mechanism is presented in figure 2.6.

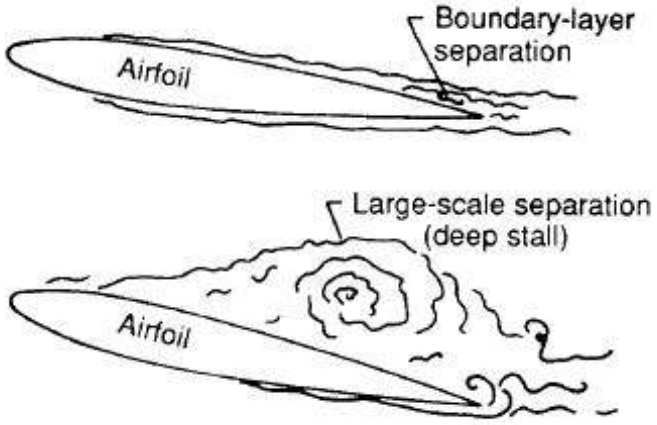

Figure 2.6: Separation/stall noise [15].

Laminar Boundary Layer Vortex Shedding Noise

Any airfoil subject to a flow will develop a boundary layer in all of the extent of its surface between the leading and the trailing edge, which for low Reynolds number and angles of attack, is denominated as a laminar boundary layer.

This boundary layer is created due to the existence of an adverse pressure gradient that is found along the airfoil surfaces in the streamwise direction, which creates pressure instabilities along the layer.

When these instabilities interact with the vortexes shed by the trailing edge, a sound is radiated from the TE, being defined as the Laminar Boundary Layer Vortex Shedding Noise [15]. A schematic representation of this noise is presented in figure 2.7.

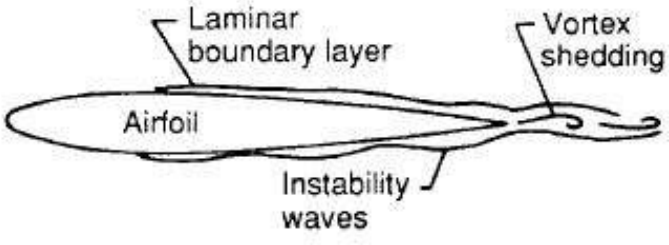

Figure 2.7: Laminar boundary layer vortex shedding noise [15].

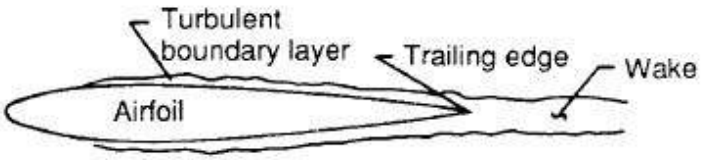

Figure 2.8: Turbulent boundary layer trailing edge noise [15].

Turbulent Boundary Layer Trailing Edge

If certain conditions are met such as an high Reynolds number and a given angle of attack, the existing boundary layer in the airfoil will transition from laminar to turbulent at a given chordwise position.

In a turbulent boundary layer, there is an high recirculation of flow which induces a pressure fluctuation zone and analogously to LBL-VS noise, when these fluctuations interact with the vortexes shed by the trailing edge, a broadband noise is emitted. This noise is named as Turbulent Boundary Layer Trailing Edge Noise [15] and it is depicted schematically in figure 2.8.

Turbulent Inflow Noise

In most industrial fan applications, it is rarely found a situation where the inflow that goes through the fan is perfectly uniform, most often including sheared flow with different velocity profiles which creates turbulent eddies of various sizes and speeds.

In the specific case of outdoor air conditioning units, the turbulent inflow is mainly a consequence of the inlet and its geometrical characteristics (e.g open versus grid inlet), and when the turbulent inflow encounters the fan, it produces a broadband, vibrating sound which is called the Turbulent Inflow Noise [15].

This noise is characterized by two quantities; the turbulence intensity, which is a numerical indicator of the turbulence fluctuations and it is defined as the ratio between the eddies velocity standard deviation and the mean flow speed, and the turbulence length scale, which is the characteristic dimension related to the eddies size.

While it is a broadband noise, there is a correlation between the frequency of the noise produced and the size of the eddies. If the eddies are large, they will affect the airfoil and change its response as a whole, therefore producing low frequency noise. If the eddies are small, it will produce a localized response which will radiate an high frequency noise [15].

2.5 Noise Prediction Method

The method used in this work to predict the fan noise consists in dividing the blades into segments with a given span length, measured radially and defined by the airfoil shapes where the blade is sectioned. Given these segments, the numerical noise prediction models are then applied to the airfoil shapes, since in the 2D approximation presented in [16], the noise radiated by a blade segment can be assumed to be similar to the noise radiated by an equivalent airfoil section. This approximation is valid assuming

that the blade elements are not too close the hub and tip areas. For the elements that have proximity to these zones, a hub and tip correction is applied and it will be presented in Section 2.6.1.

Therefore, assuming mutually incoherent radiation from the blades [17], the sound pressure level of each blade segment can be computed and the total sound power level of the rotor for each frequency band is the sum of the noise produced by each noise element, given by

$$L^i_{p,total} = 10\log_{10}\left(\frac{N_B}{N_{az}}\sum_j 10^{\frac{L^i_{p,j}}{10}}\right) \quad , \tag{2.5}$$

where N_B is the number of blades of the fan, N_{az} is the number of azimuthal positions where the blade is sectioned and $L^i_{p,j}$ is the sound power level computed in the j blade segment for the i frequency band.

With the sound power level computed for a spectrum of frequency bands, it is possible to calculate the total sound power level for the fan by adding the SPL for each frequency band,

$$L_{p,overall} = 10\log_{10}\left(\sum_i 10^{\frac{L^i_{p,total}}{10}}\right) \quad , \tag{2.6}$$

being the sum defined as the Overall Sound Pressure Level (OASPL).

In order to compute the noise produced by each blade segment, a numerical noise prediction model or set of models has to be chosen, considering the objectives of the work and the required level of accuracy. In Computational Aeroacoustics, noise prediction numerical schemes for axial flow fans can be classified in the following way:

- **Class I methods** Predictions giving an estimate of overall noise level as a simple algebraic function of basic machine parameters, such as, diameter, speed, flow rate, among others;
- **Class II methods** Predictions based on separate consideration of the various mechanisms causing fan noise, using selected fan parameters, being required some assumptions to simplify the problem;
- **Class III methods** Predictions using full information about the noise mechanisms requiring a detailed description of geometry and aerodynamics, being necessary the use of an advanced CFD tool.

While Class III methods are those that produce the most accurate results, they are very resource-intensive and time-consuming and are not suited for the preliminary design phase of a fan, being commonly used by academic researchers. Class I methods are very fast, but exceedingly simple with a risk to over or under-predict the noise levels with an high error level. Therefore, for the sake of compromise between speed and accuracy, the best choice for this work are Class II methods.

These methods consist mainly in semi-empirical schemes, which are a set of formulas determined by coupling analytic analysis and experimental data, by fitting the data into an expression which allows for a quick and simple replication of that data through the input of some selected parameters.

In order for these schemes to maintain their simplicity, some assumptions and simplifications have to made, such as acoustic compactness, which means that the dimensions of the noise sources, which in this case is the chord and span length of the blade segments, have to be smaller that the wavelength of the sound emitted. So, the higher the frequency for which it is desired that the methods are valid, the smaller the blade segments have to be. For example, in order for a calculation for 10 kHz to be valid, the chord and span length of a blade segment cannot exceed 3.4 centimeters.

Another simplification is to assume that the flow is mainly two dimensional, since most of the presented semi-empirical methods in this section, are applicable to airfoil in two dimensional flows. This is largely true for outboard, but not too close to the hub and tip area, blade sections, which tend to dominate the noise production. Additionally, in [18] it is argued that the sound spectrum of a rotating broadband source is not strongly affected by its rotation, if the angular velocity is low enough, which means, for noise prediction purposes, that stationary, single surface, two dimensional methods can be applied to a rotating fan.

Despite these assumptions, the accuracy of these prediction schemes is satisfactory, considering the low amount of resources and time required for the computation of the prediction, being suited to use in an optimization procedure, which requires a fast and simple calculation method in order to be used in a high number of iterations in a short time.

2.5.1 TEB-VS Noise Prediction Model

Brooks and Marcolini [15] derived a formula from experimental data obtained by Brooks and Hodgson [19] to predict Trailing Edge Bluntness noise,

$$L_{Blunt} = 10\log\left(\frac{hM^{5.5}L\bar{D}_h}{r_e^2}\right) + G_1\left(\frac{h}{\delta^*_{avg}}, \Psi\right) + G_2\left(\frac{h}{\delta^*_{avg}}, \Psi, \frac{St'''}{St'''_{peak}}\right) \quad , \tag{2.7}$$

where h is the bluntness thickness, M is the airfoil local Mach number, L is the blade element length, r_e is the effective observer distance, $\bar{D}_h$ is a directivity function which is defined in Subsection 2.5.7, δ^*_{avg} is the average between the pressure and suction surfaces boundary layer displacement thicknesses, $(\delta^*_p + \delta^*_s)/2$ and Ψ is the trailing edge angle.

The characteristic length used to define the Strouhal number St''' is the trailing edge thickness,

$$St''' = \frac{fh}{U} \quad , \tag{2.8}$$

with f as the frequency for which the noise is computed and U as the mean flow velocity.

The peak Strouhal number is defined by the following relations:

$$St'''_{peak} = \begin{cases} \dfrac{0.212 - 0.0045\Psi}{1 + 0.235\left(h/\delta^*_{avg}\right)^{-1} - 0.0132\left(h/\delta^*_{avg}\right)^{-2}} & \left(h/\delta^*_{avg} \geq 0.2\right) \\ 0.1\left(h/\delta^*_{avg}\right) + 0.095 - 0.00243\Psi & \left(h/\delta^*_{avg} < 0.2\right) \end{cases} \tag{2.9}$$

The function G_1 determines the peak level of the spectrum and it is a function of the thickness ratio

and trailing edge angle,

$$G_1\left(\frac{h}{\delta^*_{avg}}, \Psi\right) = \begin{cases} 17.5\log\left({}^{h}/_{\delta^*_{avg}}\right) + 157.5 - 1.114\Psi & \left({}^{h}/_{\delta^*_{avg}} \leq 5\right) \\ 169.7 - 1.114\Psi & \left({}^{h}/_{\delta^*_{avg}} > 5\right) \end{cases} \quad , \tag{2.10}$$

and the spectral shape function G_2 involves an interpolation between angles $\Psi = 14°$ and $\Psi = 0°$,

$$G_2\left(\frac{h}{\delta^*_{avg}}, \Psi, \frac{St'''}{St'''_{peak}}\right) = (G_2)_{\Psi=0°} + 0.0714\Psi\left[(G_2)_{\Psi=14°} - (G_2)_{\Psi=0°}\right] \quad . \tag{2.11}$$

Due to being overly extensive, functions $(G_2)_{\Psi=14°}$ and $(G_2)_{\Psi=0°}$ are presented in Appendix A.1.

2.5.2 Tip Vortex Formation Noise Prediction Model

The prediction for Tip Vortex noise is given by the following formula, defined by Brooks [15]:

$$L_{Tip} = 10\log\left(\frac{M^2 M^3_{max}\ell^2\bar{D}_h}{r_e^2}\right) - 30.5\left(\log St'' + 0.3\right)^2 + 126 \quad , \tag{2.12}$$

where ℓ is the spanwise extent of the separation caused by the tip vortex at the trailing edge.

The Strouhal number is

$$St'' = \frac{f\ell}{U_{max}} \quad . \tag{2.13}$$

In the case of a rounded tip, ℓ can be estimated by

$$\frac{\ell}{c} \approx 0.008\alpha_{TIP} \quad , \tag{2.14}$$

where α_{TIP} is the angle of attack of the tip of the blade. For the case of a flat tip,

$${}^{\ell}/_{c} = \begin{cases} 0.0230 + 0.0169\alpha'_{TIP} & (0° \leq \alpha'_{TIP} \leq 2°) \\ 0.0378 + 0.0095\alpha'_{TIP} & (2° < \alpha'_{TIP}) \end{cases} \quad , \tag{2.15}$$

with α'_{TIP} given by

$$\alpha'_{TIP} = \left[\left(\frac{{}^{\partial L'}/_{\partial y}}{\left({}^{\partial L'}/_{\partial y}\right)_{ref}}\right)_{y\to TIP}\right]\alpha_{TIP} \quad . \tag{2.16}$$

The maximum Mach number M_{max} of the flow within or about the separated flow region at the trailing edge and the respective maximum speed U_{max} are

$${}^{M_{max}}/_{M} \approx (1 + 0.036\alpha_{TIP}) \tag{2.17a}$$

and

$$U_{max} = c_0 M_{max} \tag{2.17b}$$

A representation of some of the referred variables above is shown in figure 2.9.

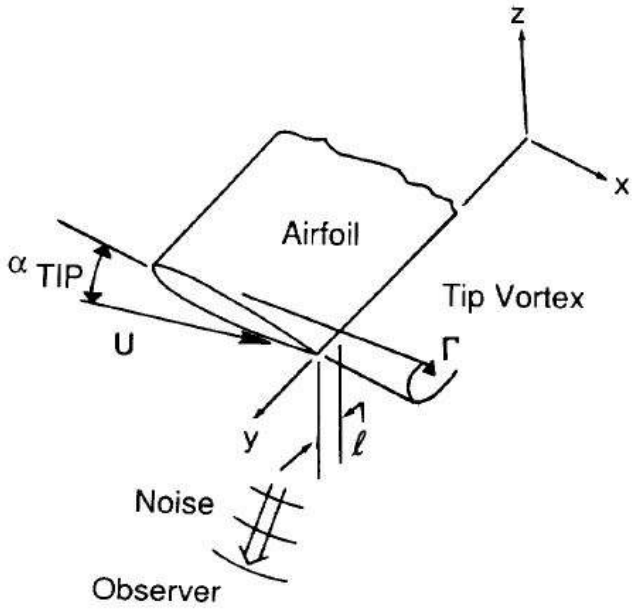

Figure 2.9: Variables used in tip vortex noise prediction [15].

2.5.3 LBL-VS Noise Prediction Model

The proposed model for prediction of Laminar Boundary Layer Vortex Shedding Noise, defined by Brooks and Hodgson [19], is described by,

$$L_{LBL-VS} = 10\log\left(\frac{\delta_p M^5 L \bar{D}_h}{r_e^2}\right) + G_3\left(\frac{St'}{St'_{peak}}\right) + G_4\left[\frac{R_c}{(R_c)_0}\right] + G_5(\alpha_*) \quad , \tag{2.18}$$

where δ_p is the boundary layer thickness in the pressure side, G_3, G_4 and G_5 are spectral functions which are defined in Appendix A.2, R_c is the chordwise Reynolds number and α_* is the local effective angle of attack.

The Strouhal number St' is defined as

$$St' = \frac{f\delta_p}{U} \tag{2.19}$$

and

$$St'_1 = \begin{cases} 0.18 & \left(R_c \leq 1.3\times10^5\right) \\ 0.001756 R_c^{0.3931} & \left(1.3\times10^5 < R_c \leq 4\times10^5\right) \\ 0.28 & \left(4\times10^5 < R_c\right) \end{cases} \quad , \tag{2.20}$$

with

$$St'_{peak} = St'_1 \times 10^{-0.04\alpha_*} \quad . \tag{2.21}$$

2.5.4 TBL-TE Noise Prediction Model

The scaling effort done by Brooks and Hodgson[15], based on the work from Ffowcs Williams and Hall [20] in order to predict Turbulent Boundary Layer Trailing Edge Noise results in,

$$L_{TBL-TE} = 10\log\left(10^{L_\alpha/10} + 10^{L_s/10} + 10^{L_p/10}\right) \quad , \tag{2.22}$$

where L_α, L_s and L_p are the sound pressure levels for each contribution.

The pressure side contribution is given by

$$L_p = 10\log\left(\frac{\delta_p^* M^5 L \bar{D}_h}{r_e^2}\right) + A\left(\frac{St_p}{St_1}\right) + (K_1 - 3) + \Delta K_1 \quad , \tag{2.23}$$

the suction side by

$$L_s = 10\log\left(\frac{\delta_s^* M^5 L \bar{D}_h}{r_e^2}\right) + A\left(\frac{St_s}{St_1}\right) + (K_1 - 3) \tag{2.24}$$

and separation/stall by

$$L_\alpha = 10\log\left(\frac{\delta_s^* M^5 L \bar{D}_h}{r_e^2}\right) + B\left(\frac{St_s}{St_2}\right) + K_2 \quad , \tag{2.25}$$

where δ^* is the boundary layer displacement thickness and A, B, K_1 and K_2 are empirical spectral shape and amplitude functions described in Appendix A.3.

Since most of the models developed by Brooks and Hodgson are based on the NACA 0012 airfoil, they defined that for angles of attack higher than $12.5°$, which is stall angle for the same airfoil, the TBL-TE noise mechanism consists mainly in the separation/stall contribution, being the equations (2.23) to (2.25) replaced by

$$L_p = -\infty \quad , \tag{2.26}$$

$$L_s = -\infty \tag{2.27}$$

and

$$L_\alpha = 10\log\left(\frac{\delta_s^* M^5 L \bar{D}_\ell}{r_e^2}\right) + A'\left(\frac{St_s}{St_2}\right) + K_2 \quad , \tag{2.28}$$

where A' is the shape function A for a Reynolds number three times the actual Reynolds number.

The Strouhal numbers are defined by these set of equations:

$$St_p = \frac{f\delta_p^*}{U} \quad , \tag{2.29}$$

$$St_s = \frac{f\delta_s^*}{U} \quad , \tag{2.30}$$

$$St_1 = 0.02M^{-0.6} \tag{2.31}$$

and

$$St_2 = St_1 \times \begin{cases} 1 & (\alpha_* < 1.33) \\ 10^{0.0054(\alpha_* - 1.33)^2} & (1.33 \leq \alpha_* \leq 12.5) \\ 4.72 & (\alpha_* > 12.5) \end{cases} \quad . \tag{2.32}$$

2.5.5 Turbulent Inflow Noise Prediction Model

For the prediction of Turbulent Inflow Noise, a semi-empirical method developed by Carolus and Schneider in [21] specifically for axial flow fans was chosen.

The basis of this method consists on the prediction of the spectral density of the acoustic power W radiated from Z uncorrelated broadband sources, which in this work will be considered as the number of blades, and it is given by

$$PSD_W(f) \equiv \frac{\mathrm{d}W(f)}{\mathrm{d}f} = \frac{\pi}{4} \frac{Z}{\rho c_0^2} \frac{f}{r_a(1 - (r_i/r_a)^2)^2} \Psi PSD_F(f) \quad , \tag{2.33}$$

where r_i is the hub radius, $r_a = \dfrac{D}{2}$, D is the diameter of the fan, ρ is the fluid density (in this case, air) and c_0 is the speed of sound. The radiation factor Ψ accounts for mean flow in both the $+x$ and $-x$ directions, but due to the case in study being a low axial flow Mach number, this factor is set to 1.

In this model, the aeroacoustic sources are represented by the force fluctuation on a blade, PSD_F, which can be expressed in terms of the fluctuating surface pressure distribution, PSD_{sp}, and the correlation area A_c, as

$$PSD_F(f) = \iint_A PSD_{sp}(f, \xi_1, \xi_3) A_c(f, \xi_1, \xi_3) \mathrm{d}\xi_1 \mathrm{d}\xi_3 \quad . \tag{2.34}$$

In this work, equation (2.34) is approximated by using the blade division which was described in the beginning of Section 2.5 and evaluating and summing the product between the integrand and the projected area of each blade segment. This projected area is calculated using a numerical integration scheme, more specifically, the Simpson's rule.

The coordinates ξ_1 and ξ_3 are part of the rotating frame of reference defined in the model which is shown in figure 2.10, along with the used stationary coordinate system.

As it was previously referred, this noise mechanism is due to the turbulent eddies approaching the fan which cause a fluctuating pressure difference between the two sides of a blade. This fluctuation is due to an imposing and varying velocity, consequence of the eddies turbulence, w_2' which is perpendicular to the blade surface and $w_2' \ll w_1$, with w_1 as the local speed of the blade segment in the rotating frame of reference.

Defining the spectral density of the imposed velocity fluctuation as $PSD_{w2} \equiv \dfrac{\mathrm{d}\overline{w_2'}}{\mathrm{d}f}$, the desired fluctuating pressure distribution PSD_{sp} will be given by

$$PSD_{sp} \equiv \frac{\mathrm{d}\overline{\Delta p'^2}}{\mathrm{d}f} = \frac{1}{4}(0.9\pi)^2 \rho^2 w_1^2 PSD_{w2} \quad . \tag{2.35}$$

For small angles γ, PSD_{w2} can be approximated by the one-dimensional energy spectrum $PSD_{cx} \equiv$

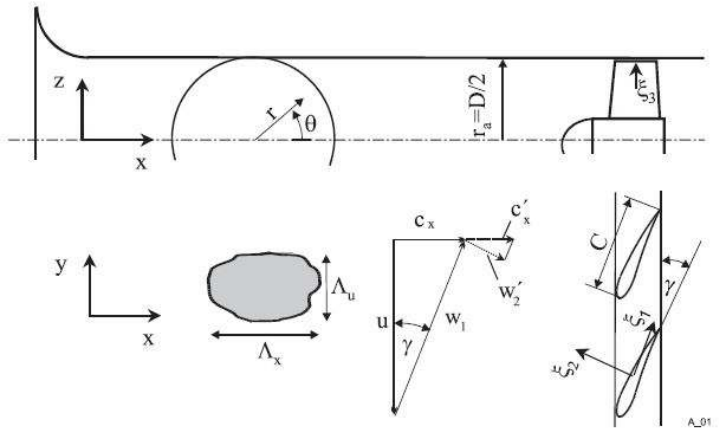

Figure 2.10: Coordinate systems and variables used in the prediction of Turbulent Inflow noise [21].

$\frac{\mathrm{d}\overline{c_x'^2}}{\mathrm{d}f}$, with c_x' as the mean flow velocity fluctuation caused by the turbulent eddies. This energy spectrum can be determined by the non-dimensional spectrum,

$$PSDL_{cx}^{*} = 10\log\left(\frac{PSD_{cx}}{c_x T u^2 \Lambda_x}\right) dB \quad , \tag{2.36}$$

where Tu and Λ_x are the turbulence intensity and length scale, respectively.

There are several published empirical correlations which give this spectrum, being chosen a polynomial curve fit to an extensive series of measurements by Költzsch in [22],

$$PSDL_{cx}^{*}(Sr_{\Lambda x}) = \sum_{k=1}^{4} a_k (\log(Sr_{\Lambda x}))^{k-1} dB \quad , \tag{2.37}$$

with $a_1 = -9.784$, $a_2 = -19.001$, $a_3 = -5.548$ and $a_4 = -0.06$. This correlation is a function of the Strouhal number,

$$Sr_{\Lambda x} = \frac{f\Lambda_x}{c_x} \quad . \tag{2.38}$$

As it can be seen from equations (2.36) and (2.38), there is a dependence on the turbulence parameters Tu and Λ_x in order for this model to work. Therefore, the authors of the model realized an experimental evaluation in order to characterize statically these quantities, for several inflow configurations, such as Natural Inflow (NI), where there was not any type of turbulence control, Boundary Layer Removal (BLR) by suction flow through a porous wall section, Turbulence Control Screen (TCS), which is an hemispherical device surrounding the intake nozzle used to generate an inflow with extremely low turbulence and the placement of a grid array upstream of the fan, a configuration the authors named RPG1, for a fine grid mesh or RPG2, for a coarse one, among others. A schematic image of the test and the different inflow configurations used in this experimental assessment is shown in figure 2.11, alongside a representation of the RPG1 inflow configuration in figure 2.12.

Since the RPG1 configuration has the most resemblance to a typical outdoor AC unit grid inflow, it was the chosen configuration to characterize the baseline fan. However, since the turbulence parameters are available for various inflow conditions, a study can be made to evaluate the impact of these

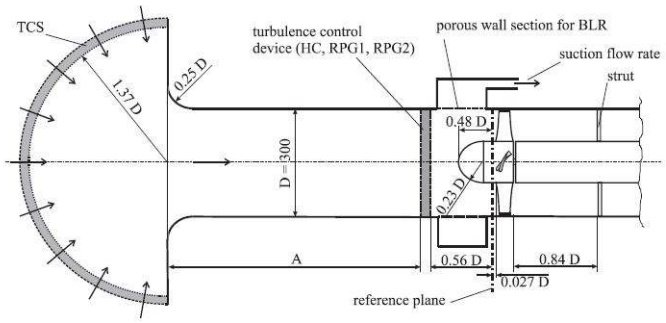

Figure 2.11: Schematic of the test stand used to determine the turbulence parameters [21].

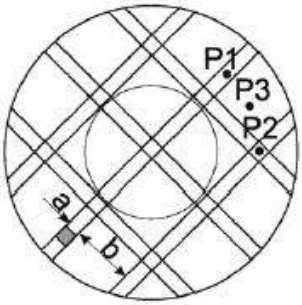

Figure 2.12: Representation of the RPG1 inflow configuration [17].

conditions in the fan aerodynamic performance and noise production. Therefore, the range of values for the turbulence parameters for various inflow conditions are shown in table 2.2.

Configuration type	Λ_x (mm)	Tu (%)
RPG1	9-16	12.5-20.9
Natural Inflow (NI)	12-35	0.6-14.2
Honeycomb (HC)	3-15	1.4-13.5
RPG2	10-18	16.7-21.3
TCS	7-28	0.4-8
TCS + BLR	1-8	0.5-5

Table 2.2: Turbulence parameters for multiple inflow configurations (adapted from [17]).

These range of values will allow for a study on the impact of the inlet grid configuration in the overall noise produced by the fan, which is considerable, as it will be shown in subsequent sections.

The correlation area A_c is assumed to be in the order of the size of an incoming turbulent eddy, $A_c \propto \Lambda^2$ and the frequency associated to an eddy with a speed w is $f = \frac{w}{\Lambda}$, such that $A_c \propto \left(\frac{w}{f}\right)^2$. Sharland [23] eventually proposed that

$$A_c = \frac{w_1}{2\pi f} \quad . \tag{2.39}$$

2.5.6 TBL and TE Alternative Models

Although a numerical model to predict Turbulent Boundary Layer and Trailing Edge Noise was already described in this chapter, two alternative models, one for each noise mechanism, are presented due to their simplicity and to diversify the noise models upon which the tool used in this work relies. This will

allow the fine tuning of the tool for the characterization of the baseline fan.

These models have the same basis as the Turbulent Inflow Noise prediction model, such that equations (2.33) and (2.34) also apply, with the difference residing in the computation of the PSD_{sp} and A_c terms.

Turbulent Boundary Layer Noise Model

In the case of ducted fans, the wall pressure fluctuations generated within the Turbulent Boundary Layer must be estimated in order to predict the noise produced by this mechanism. In this model, this is done by doing a polynomial curve fit to measured wall pressure fluctuations on a flat blade [24] and introducing an empirical constant to adapt the data to rotating turbomachinery blades according to Költzsch [22], resulting in the following expression to compute the fluctuating surface pressure distribution in the TBL,

$$PSD_{sp}(f) = \rho^2 w_1^3 \delta^* \left(\frac{0.01}{1 + 4.1985 Sr_{\delta^*} + 0.454 Sr_{\delta^*}^6} \right) \quad , \tag{2.40}$$

where δ^* is the boundary layer displacement thickness, and in this case, it is estimated by the flat plate approximation

$$\delta^* = 0.0518 C Re_C^{-0.2} \quad , \tag{2.41}$$

with C as the chord of the noise element.

The Strouhal number Sr_{δ^*} is defined as

$$Sr_{\delta^*} = \frac{f\delta^*}{w_1} \quad . \tag{2.42}$$

The correlation area A_c is computed by

$$A_C(f) = \begin{cases} \frac{1}{5\pi} w_1 \frac{1}{f} C^2 (r_a - r_i) & \text{for} \quad \pi Sr_C \leq 2 \\ \frac{2}{5\pi^2} w_1^2 \frac{1}{f^2} C (r_a - r_i) & \text{for} \quad 2 \leq \pi Sr_C \leq \frac{15}{\pi} \\ \frac{6}{\pi^4} w_1^3 \frac{1}{f^3} (r_a - r_i) & \text{for} \quad \frac{15}{\pi} \leq \pi Sr_C \end{cases} \quad , \tag{2.43}$$

with the relevant Strouhal number defined as

$$Sr_C = \frac{fC}{w_1} \quad . \tag{2.44}$$

Trailing Edge Noise Model

In this model, Lowson [16] developed an empirical correlation of the 1/3-octave sound pressure due to the turbulent TE flow in a distance r from the TE, based in the measurements done by Brooks et al. [15]

$$\overline{p_{TE}^2}(f) = 7.079 \times 10^{12} p_0^2 \delta^* Ma^5 (r_a - r_i) \frac{1}{r^2} G(f) \quad , \tag{2.45}$$

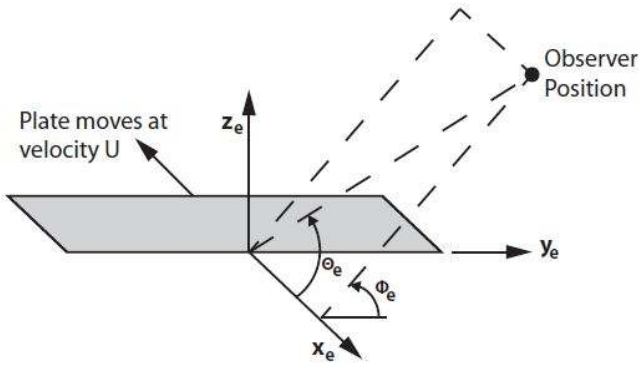

Figure 2.13: Angles used in sound directivity functions.

with p_0 as a reference pressure of 2×10^{-5} Pa, Ma is the tip Mach number and the spectrum shape function $G(f)$ given by

$$G(f) = \frac{4(f/f_{peak})^{2.5}}{(1 + (f/f_{peak})^{2.5})^2} \tag{2.46}$$

and the peak frequency

$$f_{peak} = \frac{0.02 w_1 Ma^{-0.6}}{\delta^*} \quad . \tag{2.47}$$

If the sound power is integrated as if the sound is radiated from the trailing edge as a spherical wave, the total Sound Power Spectral Density of trailing edge noise is given by

$$PSD_{TE}(f) = 7.079 \times 10^{12} P_0 \delta^* Ma^5 (r_a - r_i) \frac{4\pi}{\Delta f_{1/3oct}} G(f) \quad , \tag{2.48}$$

where P_0 is the reference sound power, 10^{-12} W and $\Delta f_{1/3oct}$ is the bandwidth of each 1/3-octave band. To calculate the sound power produced by this mechanism of the complete fan, equation (2.48) must be multiplied by the number of blades. The result of this computation will be added to the one obtained from equation (2.33) in order to have the sum of the contributions of all the noise mechanisms to which the equation applies.

2.5.7 Directivity Functions

Following the work of Amiet [25], Brooks and Hodgson [15] presented the directivity functions for high and low frequencies, which are functions that take into account the relative perception of different noise mechanisms from different points in the airfoil by the observer in its position. These functions are normalized by the trailing edge noise emitted in the $\Theta_e = 90°$ and $\Phi_e = 90°$ direction, which means that $D_h(90°, 90°) = 1$, meaning that sound directivity reaches its maximum in the TE. The angles Θ_e and Φ_e are defined in figure 2.13.

For high frequencies, the directivity is given by

$$\bar{D}_h(\Theta_e, \Psi_e) \approx \frac{2 \sin^2(\Theta_e/2) \sin^2 \Phi_e}{(1 + M \cos \Theta_e)[1 + (M - M_c) \cos \Theta_e]^2} \quad , \tag{2.49}$$

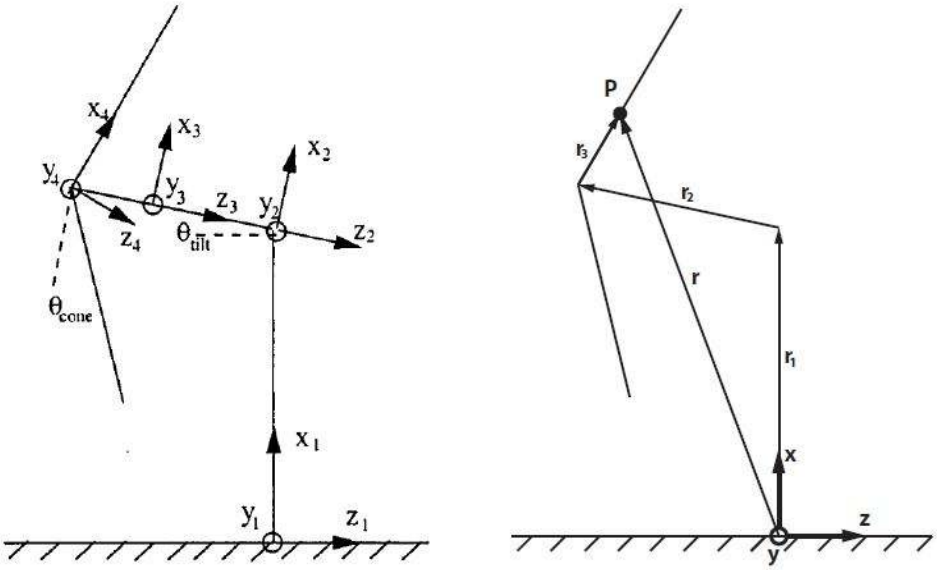

(a) (b)

Figure 2.14: Set of coordinate systems.

where $M_c \approx 0.8M$. For low frequencies, the directivity is given by

$$\bar{D}_\ell(\Theta_e, \Psi_e) \approx \frac{\sin^2\Theta_e \sin^2\Psi_e}{(1 + M\cos\Theta_e)^4} \quad . \tag{2.50}$$

When an airfoil is fixed in space, relatively to the observer, the computation of the directivity becomes a simple task, since the angles and distances are constant and easily calculated. But when trying to predict the noise of a fan, the blade rotation causes additional complications, since the observer does not follow it, being necessary to perform extra calculations to obtain the angles Θ_e and Ψ_e and observer distance r_e, used in most of the models described in this section.

In order to solve this problem, a set of coordinate systems needs to be defined. The first coordinate system (system 1) is placed on the ground, where the observer is standing. System 2 is non-rotating and its z-axis is aligned with the rotation axis of the fan. System 3 is attached to the rotating shaft and rotates along with the shaft and it is aligned with one the blades and system 4 is system 3 rotated about its x-axis with origin in the hub, in order to account for the blade twist.

This approach was originally used for a wind turbine and it is here adapted to the present case. In figure 2.14a, the referred systems are shown for a wind turbine, but by setting θ_{tilt} and θ_{cone} equal to 0 and interpreting the wind turbine tower as just the height where the axial fan is installed, the systems are valid for an axial fan case. In Appendix B, the transformation matrices between the various systems are defined.

With these systems defined, any point in the blades can be described by a vector **r** which is obtained by a sum of vectors, as shown in figure 2.14b,

$$\mathbf{r} = \mathbf{r_1} + \mathbf{r_2} + \mathbf{r_3} \quad . \tag{2.51}$$

Having the vector **r** defined, the directivity angles Θ_e and Ψ_e can be computed as shown in figure 2.13.

2.5.8 Boundary Layer Parameters

With the exception of the TBL-TE noise model, all of the numerical models used in this work to predict the several noise mechanisms need boundary layer parameters as input. While the authors of those models provided correlations to compute these parameters, they were determined based on experimental results from the NACA 0012 airfoil, and therefore are not suited for more general airfoil, such as cambered ones.

Therefore, the noise prediction method in this work is complemented with an external calculation of the boundary layer parameters using the XFOIL code [26] or the RFOIL code [27].

One shortcoming when using XFOIL is that the code does not compute the boundary layer thickness δ, being necessary the use of the relation given by Drela and Giles [28],

$$\delta = \theta \left(3.15 + \frac{1.72}{H_k - 1} \right) + \delta^* \quad , \tag{2.52}$$

with θ being the boundary layer momentum thickness and the definition of H_k from [29] for adiabatic flow in air,

$$H_k = \frac{H - 0.290M^2}{1 + 0.113M^2} \quad , \tag{2.53}$$

where H is the boundary layer shape factor.

2.6 Blade Element Momentum Theory

All of the models presented in this chapter require some aerodynamic parameters as input, such as local angles of attack or relative velocities and in order to estimate the aerodynamic performance of a fan, a prediction method is chosen.

While a full Computational Fluid Dynamics simulation using the Navier-Stokes equations would provide the referred input, it is computationally expensive and complex. Therefore, the Blade Element Momentum method is chosen for its simplicity, speed and for being the most widely used theory in rotor preliminary design.

Although the BEM method is frequently used for wind turbine applications [30] [31], it is equally valid to apply it in axial fans and propellers. Since the underlying theory for this method is extensively described by many authors [32] [33] [34], only a summarized version will be presented in here.

This method consists in equalizing the thrust and torque relations given by the blade element theory and the momentum theory, in order to achieve a mathematical expression that models the axial and tangential induction factors, a and a' given by

$$a = \frac{u}{V} \quad \text{and} \quad a' = \frac{u'}{\omega r} \tag{2.54}$$

where u is the axial induced velocity, u' is the radial induced velocity, V is the mean flow speed, ω is the

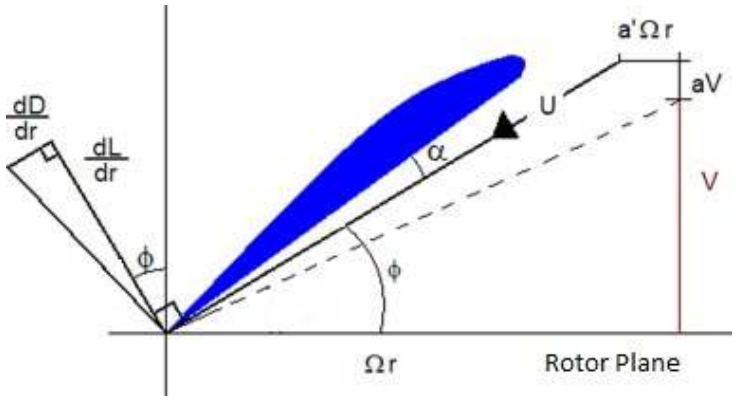

Figure 2.15: Velocities and angles in the rotor plane.

rotational speed of the fan, in radians per second and r is the radial distance of the element where the method is being applied.

As it can be seen from figure 2.15, the axial induced velocity increases the total axial speed by a factor of aV and the radial induced velocity decreases the total radial speed by a factor of $a'\omega r$, thus specifying the axial and radial components of the relative velocity U given by $V(1+a)$ and $\omega r(1-a')$, respectively. Therefore, it can be stated that

$$\tan\phi = \frac{V(1+a)}{\omega r(1-a')} \quad , \tag{2.55}$$

where ϕ is the inflow angle, the angle between the relative velocity and the rotor plane.

The momentum theory states that for a rotor annulus with a width dr and in the radial location r, the thrust produced is

$$dT = 4\pi r\rho V^2(1+a)aFdr \quad , \tag{2.56}$$

while the torque produced is given by

$$dQ = 4\pi r^3\rho V(1+a)a'\omega Fdr \quad , \tag{2.57}$$

where F is a factor taking into account the hub and tip losses, which will be explained in Section 2.6.1.

The same thrust and torque for the same rotor annulus is also predicted by the blade element theory, using

$$dT = \frac{1}{2}\rho N_B \frac{V^2(1+a)^2}{\sin^2\phi} cC_n dr \tag{2.58}$$

and

$$dQ = \frac{1}{2}\rho N_B \frac{V(1+a)\omega r(1-a')}{\sin\phi\cos\phi} cC_t r dr \quad , \tag{2.59}$$

where N_B is the number of blades, c is the element chord and C_n and C_t are, respectively, the coefficients of the resulting aerodynamic forces in the normal and tangent direction with respect to the rotor plane and are given by

$$C_n = C_l\cos\phi - C_d\sin\phi \tag{2.60}$$

and

$$C_t = C_l \sin\phi + C_d \cos\phi \quad . \tag{2.61}$$

The aerodynamic coefficients C_l and C_d are usually read from an aerodynamic table, or in the case of this work, aerodynamic polars obtained by computer simulations can be used. The quality of results produced by the BEM method is very sensitive to the quality of the input aerodynamic data.

By equating equation (2.56) and equation (2.58), the expression for the axial induction factor can be found as

$$a = \frac{1}{\frac{4F\sin^2\phi}{\sigma C_n} - 1} \quad , \tag{2.62}$$

where $\sigma = \frac{c(r)N_B}{2\pi r}$ is the local solidity. If the same procedure is done for equations (2.57) and (2.59), the radial induction factor is given by

$$a' = \frac{1}{\frac{4F\sin\phi\cos\phi}{\sigma C_t} + 1} \quad . \tag{2.63}$$

2.6.1 BEM Corrections

Tip Loss

In the original BEM theory, the losses due to the effect of blade tip vortex shedding in the induced velocity field were not accounted for. Therefore, Prandtl [35] [36] defined a loss factor to correct the BEM theory as

$$F = \frac{2}{\pi}\cos^{-1}(e^{-f}) \quad , \tag{2.64}$$

where

$$f = \frac{N_B}{2}\frac{R-r}{r\sin\phi} \tag{2.65}$$

and R is the blade radius.

Hub Loss

Since there are also vortexes that are shed near the hub, a correction factor for the hub can also be derived. This factor is computed by the same procedure that the tip loss factor, with the exception of replacing the equation (2.65) by

$$f = \frac{N_B}{2}\frac{r-R_{hub}}{r\sin\phi} \quad . \tag{2.66}$$

With these two loss factors computed, the total loss factor to be used is given by their product,

$$F = F_{tip}F_{hub} \quad . \tag{2.67}$$

2.6.2 Fan Efficiency

The main task of an axial flow fan is to push the most volume of air possible while using the least amount of energy to support its rotation. The power imparted by the fan to the flow can be expressed by the

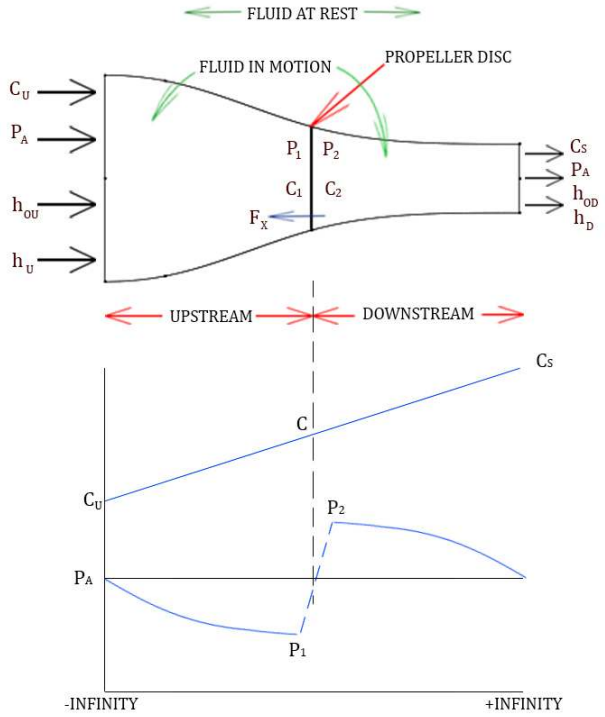

Figure 2.16: Actuator disk (propeller).

product of the total pressure rise through the fan with the volumetric flow rate delivered by the fan, $\Delta p\dot{q}$.

This pressure rise can be explained by the fact that the fan accelerates the flow while it passes from the back to the front of the fan, so that the number of air particles is higher in the front that in the back. That will create a pressure rise between the both sides of the fan.

The basic aerodynamic principles of the axial fan, which in theory can be idealized as propeller disk, can be described the actuator disk concept, represented in figure 2.16. If the fan is modeled as a uniform disk with infinite blades, the pressure rise $P_2 - P_1$ can be thought of as a reaction force applied in the fan, or in other words, the thrust produced by the fan and it is expressed by

$$T = A(P_2 - P_1) \quad , \tag{2.68}$$

where A is the area of the disk.

Since the volumetric flow can be given by AV, the power of the flow provided by the fan is given by

$$\Delta p\dot{q} = \frac{T}{A} AV = TV \quad . \tag{2.69}$$

The supplied power required to rotate the fan is given the Euler turbomachinery equation, $P = Q\omega$, where Q is the torque produced by the fan. Therefore, if the fan efficiency is the division between the

power transferred to the flow and the power used by the fan, it is given by

$$\eta = \frac{TV}{Q\omega} \quad . \tag{2.70}$$

The total thrust and torque produced by the fan can be calculated by summing the thrust and torque computed in each blade element, given by equations (2.56) and (2.57).

Chapter 3

Aeroacoustic Tool

For the purposes of this work, an existing custom made aeroacoustic tool is adapted [37]. This tool was developed using the C++ and Python programming languages and in this chapter a brief description of its functionalities is presented. Since the program was originally built with the intent of analyzing wind turbines, some adaptations were required to be introduced into the tool in order to be used for a low speed axial fan case. With these changes to the program, a validation using the acoustic results of a known axial fan case is necessary and therefore, also described in this chapter.

3.1 Brief Description

The code used in the tool is written in C++ and Python, taking advantage of the speed of C++ and the inherent flexibility of an high-level programming language such as Python. Also, being both object-oriented languages, the code is highly modular, being possible the addition of aeroacoustic or aerodynamic modules with relatively low effort.

An interface code which links C and C++ to several other high-level programming languages named SWIG (Simplified Wrapper and Interface Generator) [38] is used to connect the code developed in each language, eliminating the need for files to transfer data from one to another. Therefore, any code produced in C++ can be used as a dynamic shared library by Python.

The code can be divided in three major groups:

- **Geometry** Where all geometry manipulating classes are defined, such as *Rotor*, *Blade* and *Section*, which define the rotor to be analyzed, its blade and the radial sections which define it;
- **Aerodynamic** Section which creates and modifies the polars required for the BEM aerodynamic input (see Section 2.6) and computes the Boundary Layer parameters necessary for the models described in Section 2.5, using XFOIL or RFOIL and it is composed by classes *Polar* and *BLayer*;
- **Analysis** Where the aerodynamic and aeroacoustic analysis functions are defined and executed, being all condensed in the class *Analysis* and using the C++ libraries *BEM* and *NOISE* where the BEM equations and noise models are implemented, respectively.

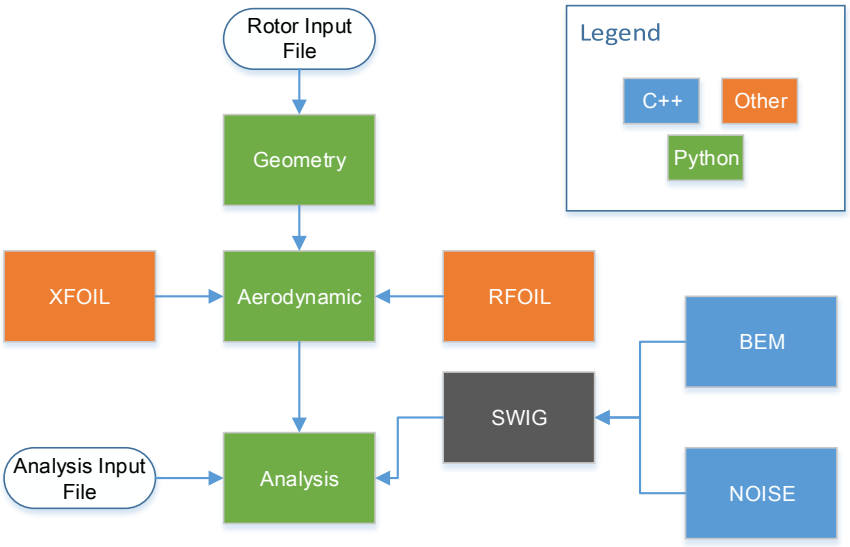

Figure 3.1: Work-flow of the aeroacoustic tool.

In figure 3.1, is shown a diagram with the relation among the code modules, the libraries and external software upon which they depend and the inputs. The rotor input file is a text file which contains all the relevant parameters to define the fan geometry to be analyzed, such as hub and maximum radius, number of blades and the sections which define the blade radially, among others. The analysis input file is where all the analysis conditions are specified, for example, the number of radial elements upon which the noise calculations will be performed and the respective noise models to be used or the physical constants pertaining to the circumstances of the situation to be analyzed, such as air density, sound speed or the mean inflow speed.

After the analysis is concluded, the code can output all of the results of the BEM calculations, such as the radial distribution of angle of attack, local Reynolds, relative velocities, etc. in a CSV (Comma Separated Value) file along with all the noise computations, such as the sound spectra for each noise mechanism and the total noise spectrum, either as sound pressure level or sound power level, with the option to be A-weighted or not.

3.2 Adaptation for a Low Speed Fan Case

Originally, the code was created with the intent to analyze wind turbines, but since an axial fan is similar to a wind turbine in some physical aspects, the code can be used in the axial fan case, given that some adaptations are made. It has to be noted that instead of altering the original functionalities of the code, the adaptations here described were added to the code, being given the option to the user to choose between a wind turbine or axial fan analysis.

The main function of a wind turbine is to remove energy from the flow that passes through it, hence reducing the flow speed. The opposite happens in axial flow fans, where the objective is to push a given

volume of air by increasing its kinetic energy, or in other words, by increasing the passing flow speed. These changes in flow speed are reflected by the axial induced velocity present in the BEM theory, namely the wind turbine induces a velocity opposite to the flow direction, slowing it down and the axial fan induces a velocity along the flow direction, increasing its speed. Therefore the underlying equations of the BEM theory originally implemented in the aeroacoustic tool had to be changed in order to reflect the functioning of an axial fan, regarding what is presented in Section 2.6.

The tool uses a turbulent inflow noise model of atmospheric nature, due to height of the wind turbine tower, which does not apply for the case in study, since axial flow fans are usually enclosed in duct-type housings or in confined spaces, where the wind turbulence is not present. Therefore, the noise model described in Section 2.5.5 was added to the program for prediction of turbulent inflow noise.

Also, in an effort to speed up the input of any blade geometry into the aeroacoustic tool, the Bézier parameterization scheme described in Chapter 4 was implemented in the code.

3.3 Validation

Although the code was originally validated in [37], the major alterations introduced in this work need to be validated, which in this case, is the model for turbulent inflow noise. Also, the overall behavior of the code including this new model needs to be studied and, if need be, the tool has to be fine tuned in order to best correlate with the experimental data to be a reliable tool.

3.3.1 Turbulent Inflow Numerical Model Validation

In order to validate the added model, the turbulent inflow noise prediction model is applied to an axial fan present in [21] and the results obtained by the custom code are compared to the predicted results by the semi-empirical method (SEM) described in the cited article. The geometrical characteristics of the fan and the parameters used in the analysis are described in figure 3.2 and table 3.1. The fan geometry reproduced by the custom code is presented in figure 3.3.

Parameter	Value
Number of blades	6
Rotational speed (rpm)	3000
Axial flow velocity (m/s)	10.554
Fan diameter (m)	0.299
Hub radius (m)	0.0675
Speed of sound (m/s)	340.46
Air density (kg/m^3)	1.225
Trailing edge angle (deg)	1.858
TE Thickness (% chord)	0.83

Table 3.1: Analysis parameters for turbulence inflow noise model validation.

The data used for the validation was measured under a Natural Inflow configuration, as stated in the aforementioned article. While a closed range of values is defined in table 2.2 for turbulence intensity and turbulence length scale for this inflow configuration, the *exact* values used in the test are not provided.

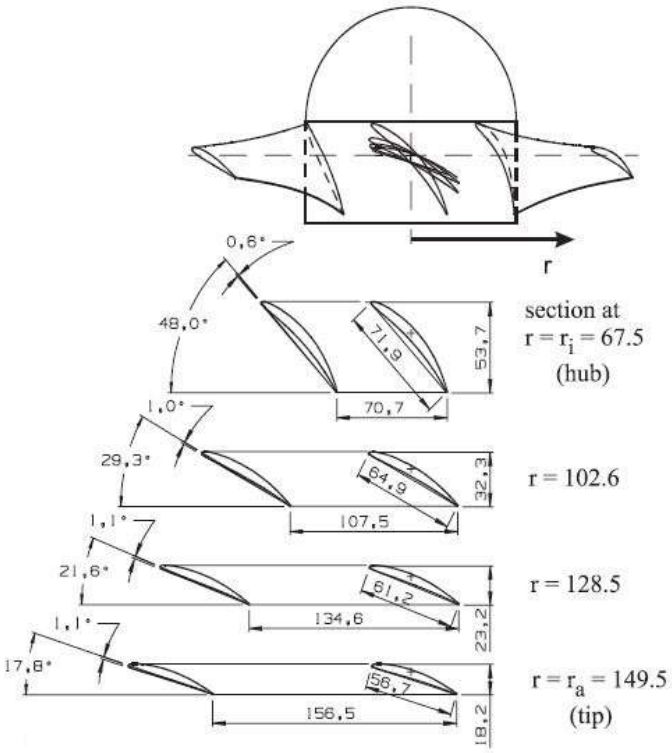

Figure 3.2: Radial distribution of section geometry of fan used for validation [21].

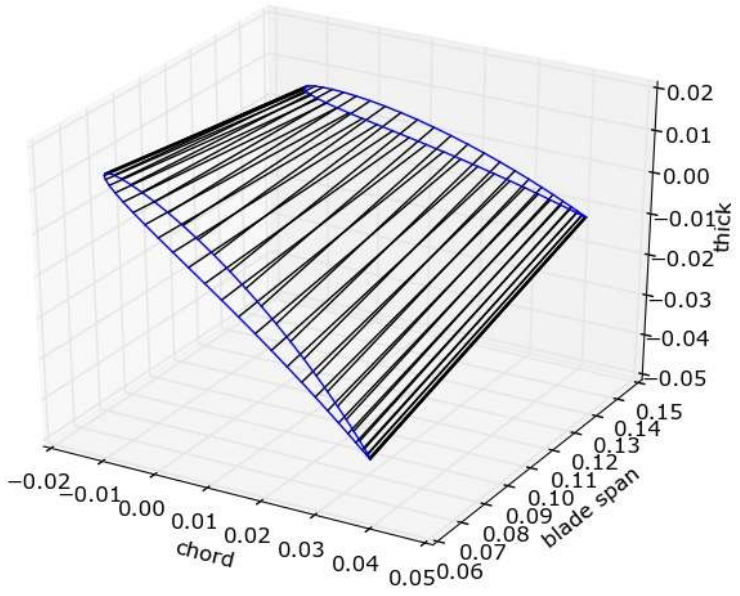

Figure 3.3: Reproduction of the geometry of the tested fan by the custom code.

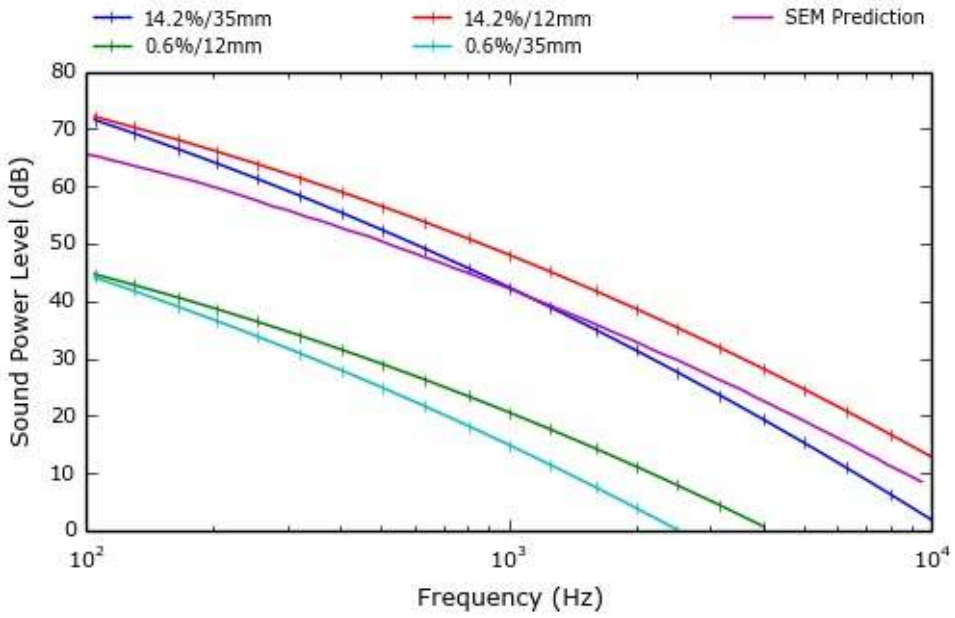

Figure 3.4: Parametric study to determine the turbulence parameters which have the best fit to the provided data.

Therefore, a parametric study with the four boundary values in the ranges for the turbulence parameters was realized in order to determine the combination which produced the sound power spectrum most similar to the one obtained by the SEM prediction. The results of the study and the respective comparison are presented in figure 3.4.

It can be seen that the increase in the turbulence intensity results in an increase in the sound produced by turbulence inflow, as expected, and that the turbulence length scale controls the decay rate of sound power along with the frequency, showing that for an high length scale of 35 mm the decay rate is higher than for a scale of 12 mm. This can be explained by the fact that an higher turbulence length scale implies eddies with less turbulence which results in less produced noise.

The results obtained with a turbulence intensity of 14.2% are the ones which resemble the most with the SEM prediction and the decay rate is similar to the prediction when the turbulence length scale is 12 mm. Therefore, a new parametric study was made, with the length scale fixed at 12 mm, to discover the turbulence intensity which produces the desired results. The results of the study are shown in figure 3.5.

The boundary values of 0.6% and 14.2% were maintained, for comparison reasons. From figure 3.5, it can be seen that the results produced with a turbulence intensity of 8% are the ones which have the best correlation with the prediction. In order to confirm that, a last test comparing the sound power spectrum computed by the custom code with a turbulence intensity of 7.5% and a turbulence length scale of 12 mm with the spectrum results present in [21] was executed, with the respective outcome presented in figure 3.6.

The results are satisfactory, with a very high correlation between the both spectra, so that the turbulent inflow numerical prediction model is validated. Also, these series of tests showed the importance and influence the turbulence parameters have in predicting with accuracy the sound produced by this

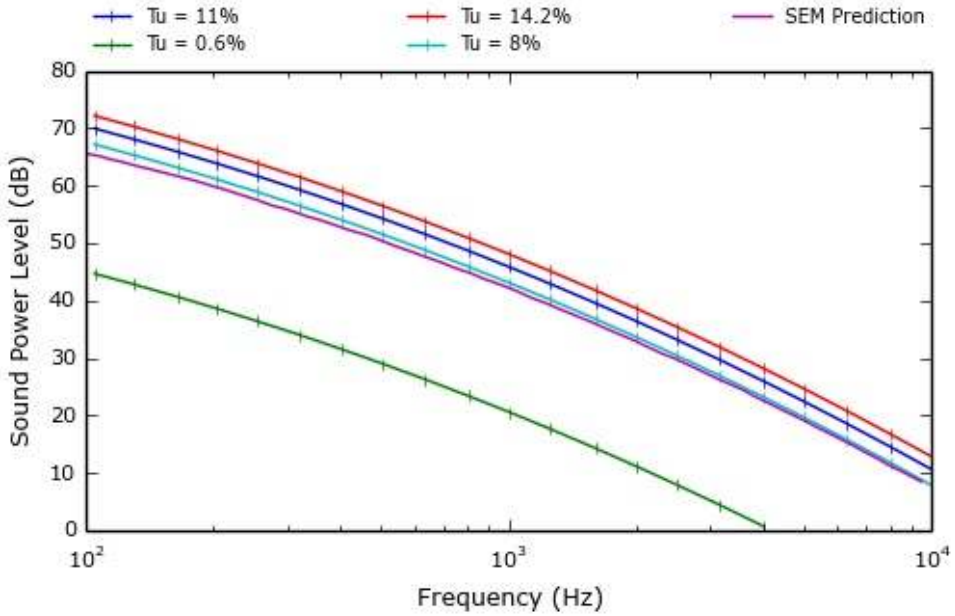

Figure 3.5: New parametric study to determine the turbulence intensity to properly fit the provided data.

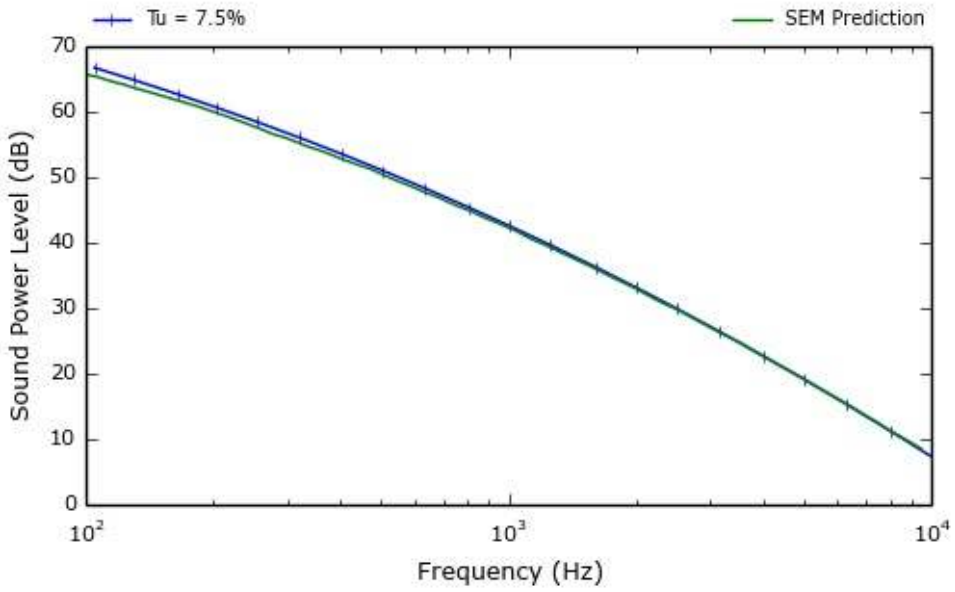

Figure 3.6: Final validation of turbulent inflow prediction code.

sound producing mechanism.

3.3.2 Overall Spectrum Validation

With the turbulent inflow numerical model validated, the inclusion of this model with the rest of the models described from Section 2.5.1 to 2.5.4 is studied. The fan presented in the previous section remains the object of study and an overall sound analysis was executed, with the same parameters presented in table 3.1 and for an observer position of $(x, y, z) = (0, 0, 1)$.

The total sound power spectrum of the fan computed by the tool is presented in figure 3.7 along with the contribution of each of the various noise mechanisms introduced in the tool. These results are compared with experimentally obtained data from the same fan with TCS+BLR inflow conditions (refer to table 2.2).

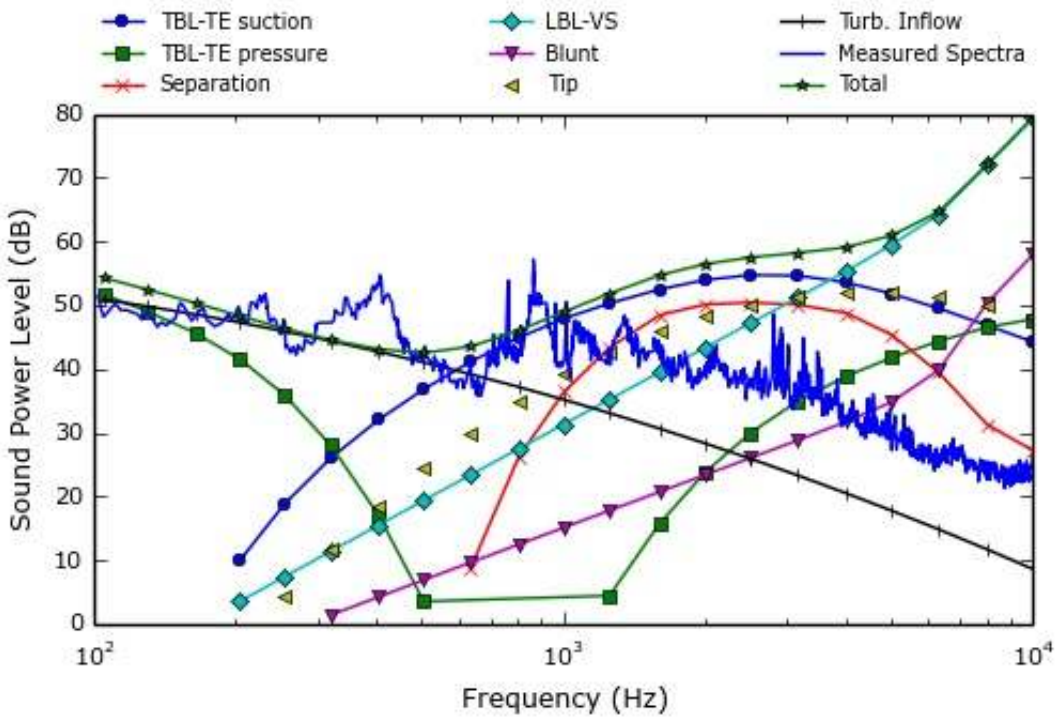

Figure 3.7: Comparison between experimental and tool computed sound power spectra.

In the low frequency range, from 100 Hz to 600 Hz, there is a clear domination of the turbulent inflow noise over the rest of the noise mechanisms, while in the mid frequency range, from 600 Hz to around 4000 Hz, it is the turbulent boundary layer-trailing edge noise from the suction part of the blade that is the most relevant and in the high frequency zone (4000 to 10000 Hz), the laminar boundary layer-vortex shedding noise mechanism creates a sharp increase in the overall produced noise.

While the total sound power spectrum has good agreement with the experimental results in the frequency range from 100 Hz to 1000 Hz, in the remaining frequency values, the tool overestimates the noise. This could be explained by the fact that most of the implemented noise mechanisms in the code are based in empirical measurements in free field conditions, while the presented experimental results are for a ducted fan.

Since the over-prediction happens in its majority in the high frequency range and it is mostly due to the LBL-VS noise mechanism, a second test where this specific model is removed was executed. The results are shown in figure 3.8.

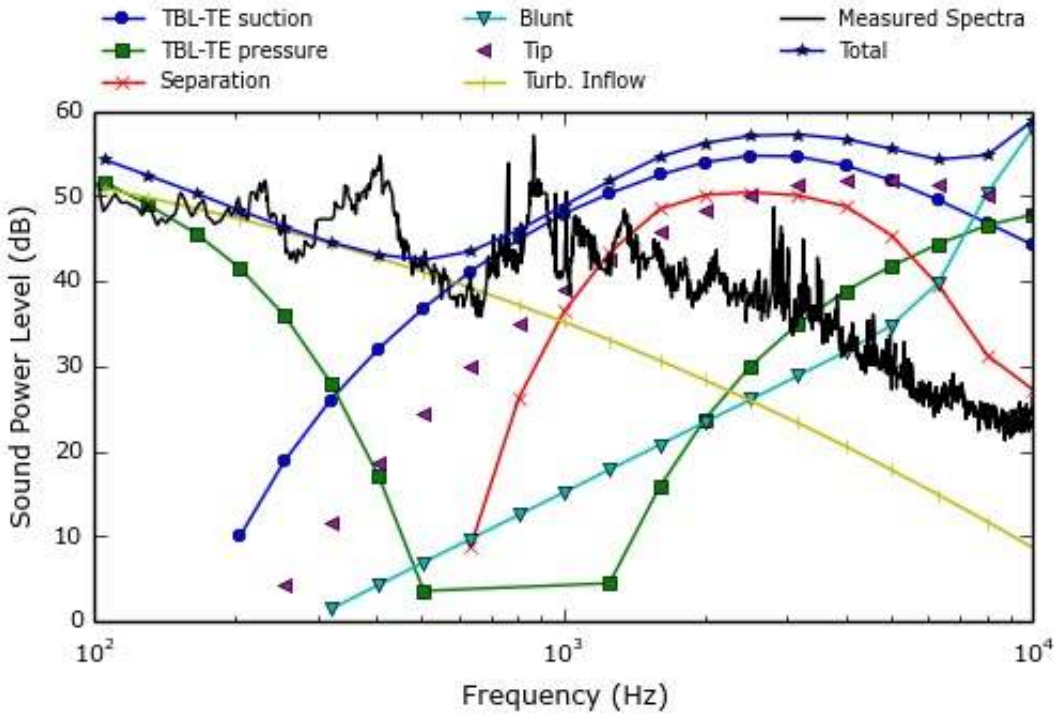

Figure 3.8: Comparison between experimental and tool computed sound power spectra, without LBL-VS noise mechanism.

It can be seen that the results in the high frequency range have improved, but there is still a noise overestimation, with differences of 10 to 20 dB. In the very high frequency zone, the Blunt and Tip noise mechanisms create a slight rise in the overall spectrum, but nonetheless it is the TBL-TE noise mechanism from the suction part of the blade that it is responsible for most of the discrepancy between the computed and experimental results in the high frequency range.

Again, the reason for this to happen might be due to the fact that the models assume free field conditions while the experimental results were measured on a fan inserted in a duct. Even so, while there is this discrepancy in high frequencies, the results are satisfactory for the initial range of frequencies, and this model can be used for comparison and optimization processes.

Nonetheless, an alternative model was tested, that includes just the turbulent inflow, turbulent boundary layer and trailing edge noise mechanisms and it accounts for wall pressure fluctuations, being suitable for ducted fans. The results are shown in figure 3.9, where the TBL and TE noise mechanisms were added and shown in a single curve.

The results are considerably better, such that the model under-predicts the noise in the mid-frequency range, but over-predicts in the high frequency range. On average, the overall prediction is satisfactory and since the main goal of this work is to minimize the overall produced noise, this is a good model to implement in the fan characterization.

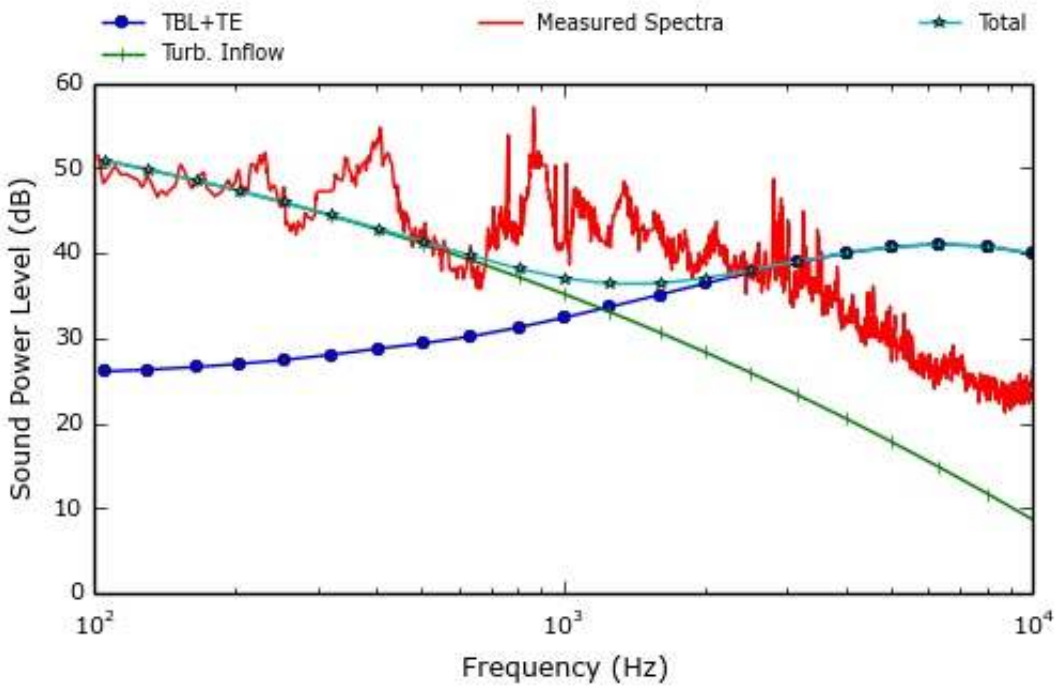

Figure 3.9: Comparison between experimental and tool computed sound power spectra.

However, since the behavior of the models studied in this chapter was compared to a fan in specific ducted conditions, both models will be used in Chapter 5 in order to choose which one has a better correlation with the baseline fan experimental data, by fine-tuning the custom tool.

Chapter 4

Blade Parametrization

In order to execute an aeroacoustic analysis of a fan, the geometry of the blades has to be properly defined. While there are varied methods to accomplish this, in this work, where the objective is to optimize the fan, there is an interest in describing the blades geometry with the least possible amount of input parameters, such that the optimizer running time is kept to a minimum and the optimization is done efficiently.

4.1 Airfoil Description

There are numerous methods available in the literature to parameterize an airfoil, such as PARSEC airfoils, B-splines, NURBS, Bézier curves, Bézier-PARSEC parameterization, among others. An extensive review of some of these methods is presented in [39] and [40].

As it was previously mentioned, the main criteria when choosing a parameterization method is to minimize the number of design variables. In the work developed in [37], the parameterization of a wind turbine blade profile was done using NURBS, leading to 20 as the chosen number of design variables to describe the profile. This number is not restrictive, it could be higher or lower, but since it produced successful results in the cited work, it will be used as a maximum threshold for the design variables used to describe the airfoils in this work.

In [41], [42] and [43], is described a method in which the blade profile is built using a camber line and a thickness curve, where the curvature and thickness distribution along the profile in the chord direction is specified, respectively, with the profile the result of the junction of these curves. Both of these curves are approximated by polynomials of a specified order, with the coefficients of the polynomials obtained by relating them to the proposed design variables. Some of these variables are the maximum camber and its location, the stagger angle, the maximum thickness and its location, among others. All of these variables are expressed in figure 4.1. Although it is stated that this method only requires 14 design parameters, due to the difficulty of measuring directly some of these parameters and the process of reconstruction from a set of Cartesian coordinates to a parameterized configuration not being too clear, this was not the chosen method.

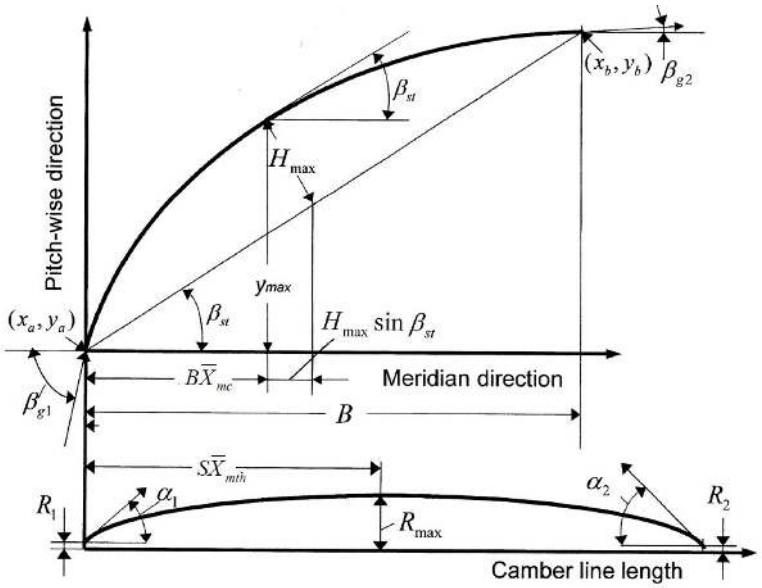

Figure 4.1: Design variables defined in [41], [42] and [43].

In [44], a parameterization method which consists in combining Bézier curves and PARSEC airfoils is presented. The driving principle behind this idea is to take advantage of the simplicity of implementation of Bézier curves and its broad use in the CAD industry and combine it with the more aerodynamic-oriented PARSEC parameterization scheme in order to avoid unrealistic or aerodynamic inefficient designs in the optimizing process. The airfoil is described by four curves, two for the leading and trailing edge camber lines and the other two for the leading and trailing edge thickness lines. These curves are determined by four Bézier points each, making up a total sum of 16 control points, some of which are fixed and the rest is a function of the defined aerodynamic parameters, namely the leading edge radius, trailing and leading edge angles and position and curvature of thickness crest some examples of these parameters. This method has a better convergence rate than most of the known methods, but it has a minimum of 25 design variables per airfoil, not meeting the criteria established in this work to use this method to parameterize the blade.

Following the method described before, the choice was made to test if Bézier curves were fit to parameterize the blade profiles.

A Bézier curve is a parametric curve defined by

$$\mathbf{B}(t) = \sum_{I=0}^{n} b_{i,n}(t)\mathbf{P}_i, \quad t \in [0,1] \quad , \tag{4.1}$$

where

$$b_{i,n}(t) = \binom{n}{i} t^i (1-t)^{n-i} \qquad \text{and} \qquad \binom{n}{i} t^i (1-t)^{n-i} = \frac{n!}{i!(n-i)!} \quad . \tag{4.2}$$

In equation (4.1), $\mathbf{P}_i$ is a vector containing the control points which define a Bézier curve, the polynomials represented by $b_{i,n}(t)$ are known as the Bernstein polynomials and t is the parametric variable which ”runs along” the curve, such that $t = 0$ and $t = 1$ refers to the beginning and end of the curve, respectively. The order of these curves is defined by the number of control points $n + 1$, such that the

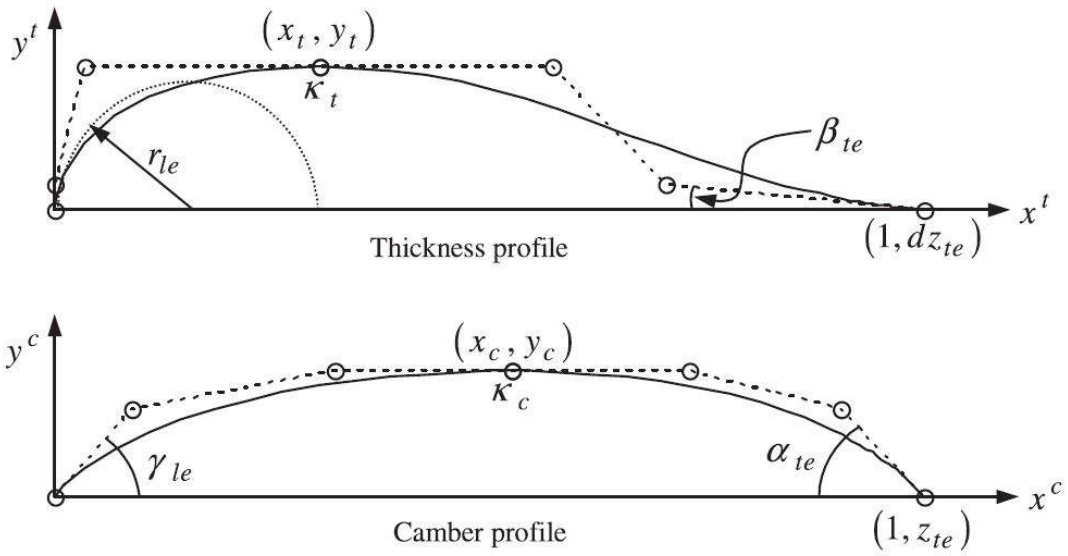

Figure 4.2: Design variables of the Bézier-PARSEC parameterization method [44].

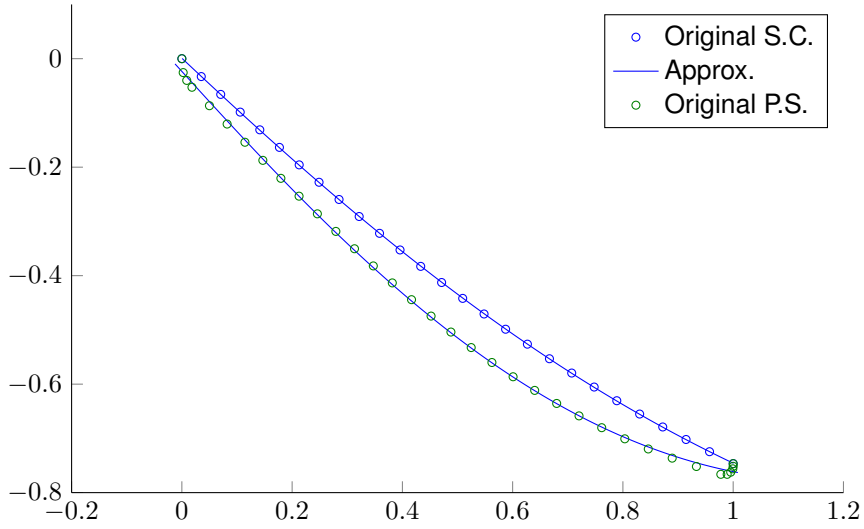

Figure 4.3: Failed test to fit 3rd order Bézier curves to one of the blade profiles.

order of the curve is always n. One of the properties of Bézier curves is that a given curve will always contain the first and last control points, with the curvature and topology of the curve a consequence of the location and number of the rest of the control points.

Given one of the blade profiles, obtained by sectioning it near the hub, it was attempted to fit the coordinates of said profile with two 3rd degree Bézier curves, one for the suction part and the other for the pressure part of the profile. This was done by minimizing the least-squares function between the profile and the interpolated coordinates, in order to minimize the overall distance between the curves and the original points. That fit was unsuccessful, as shown in figure 4.3, being that the leading and trailing edges do not connect maybe due to the low order of the curves and the high curvature of the pressure section trailing edge.

So, a second attempt was made by increasing the order of the Bézier curve which describes the pressure part of the profile, due to having the curvature referred previously, from a 3rd to a 6th order

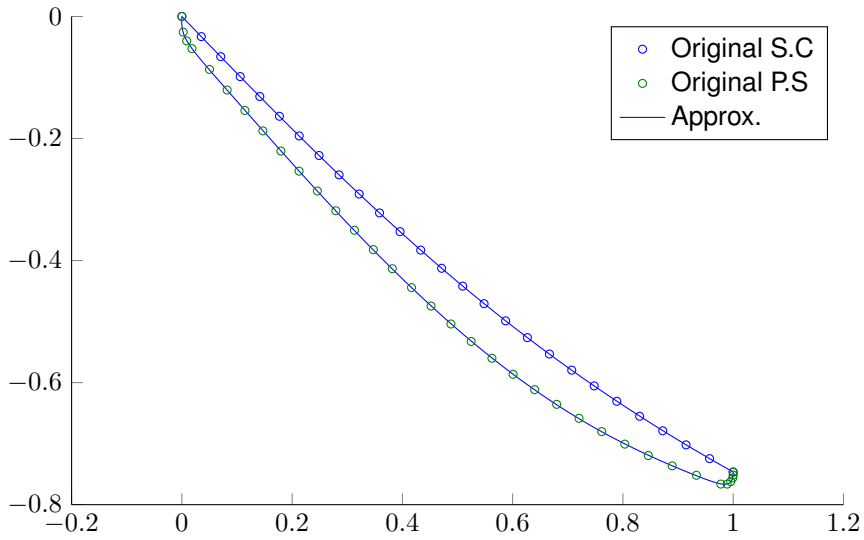

Figure 4.4: Successful fit of 3rd and 6th order Bézier to one of the blade profiles.

curve. Additionally, an algorithm, which is the result of the work developed in [45], was used to improve the results. This algorithm takes into account the ”bending” of the set of input data in order to achieve the set of control points which produce a curve that goes ”through” the given points, instead of just minimizing the mean distance between the approximation and the input data. Also, in this algorithm, the formulation presented in equation (4.1) is transformed to an equivalent matrix formulation, where the coefficients of the Bernstein polynomials, the control points and the different variables $t, t^2, t^3 \ldots, t^n$ are expressed in matrix form. This formulation is explained with more detail in [45]. Consequently from this formulation, instead of using the least-squares norm, also known as L_2 norm, to evaluate the fitness of the curve, it is used the Frobenius norm, which is the matrix norm between the interpolated and input data vectors,

$$\| \mathbf{B}(t) - P \|_F \quad . \tag{4.3}$$

As it can be seen from figure 4.4, this second fit attempt was successful, with Frobenius norms of 0.0004 and 0.0019 for the suction and pressure portions of the profile, respectively. Given the orders of the used curves and taking into account that there are two degrees of freedom for each control point, except the ones in the leading and trailing edges, where theres only the vertical degree of freedom, the number of design variables in each profile is 16.

In order to attest if this method and algorithm is really efficient, some tests to fit the Bézier curves to some airfoils were made. The results shown in figure 4.5, demonstrate that this airfoil parameterization is adequate.

4.2 3D Parametrization

With the airfoil parametrization method defined, the three-dimensional description of the blade is done by following four steps

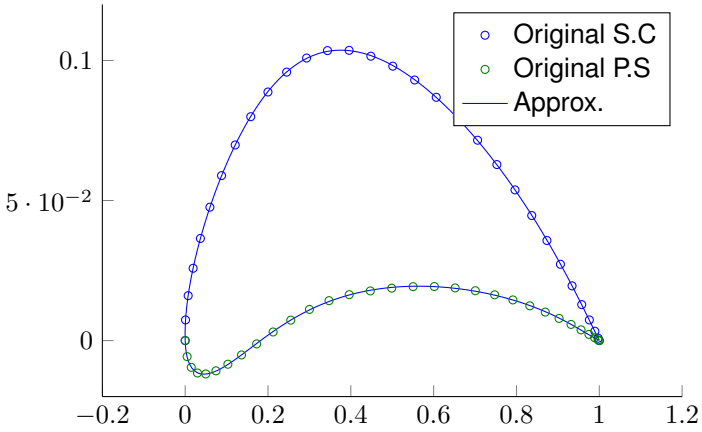

(a) NACA 6409

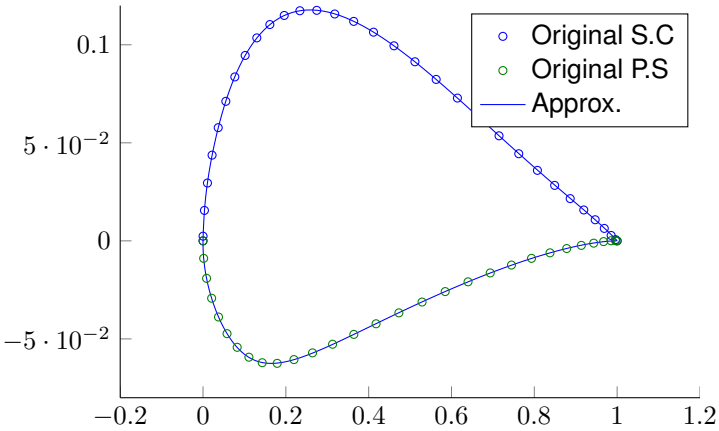

(b) Eppler E1212

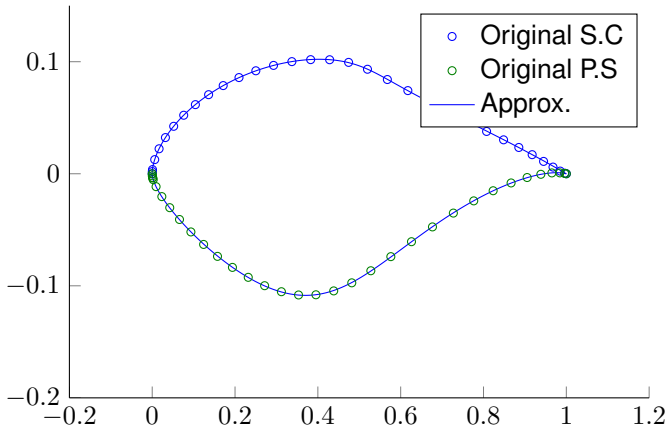

(c) NREL 809

Figure 4.5: Fitting of Bézier curves to some airfoils.

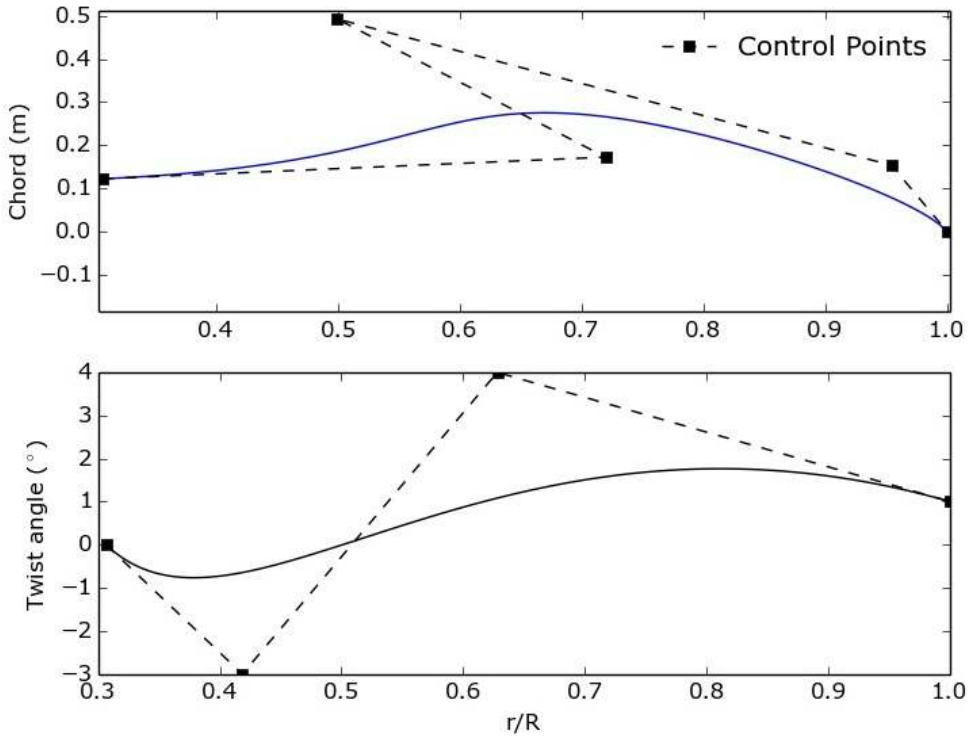

Figure 4.6: Twist and chord distribution example.

1. Obtain the radial distribution of airfoil shapes of the blade, with all of the airfoils having unit chord;
2. Connect these airfoils to form the blade basis;
3. Apply the chord distribution by scaling each airfoil according to their local chord value;
4. Apply the twist distribution by rotating each airfoil with respect to their aerodynamic center (located per default at $\frac{1}{4}$ chord, but it is customizable by the user).

The chord and twist distributions are obtained by linear interpolation between the airfoils or, if an higher order curve is needed to define the distribution, by creating control points to build a Bézier curve which will express them in a continuous function. Examples of these distributions are shown in figure 4.6.

With this approach, there is the advantage of the airfoil locations, twist and chord distributions being independent among themselves, allowing for their separate optimization in order to study the impact of each variable in the final results.

Chapter 5

Baseline Fan Characterization

In this chapter, the geometry of the baseline fan which will be optimized and the process to input it in the aeroacoustic code is presented. An aeroacoustic analysis of the fan is executed using two different methods, and an experimental correlation between the results obtained by the code and the experimental measures is done.

5.1 Blade Definition

The geometry of the fan was provided by an air conditioning manufacturer to the author in the form of a CAD file, which was edited in Solidworks. Figure 5.1 shows the different views of the 3D model of the fan. The hub and fan radius were measured in the model and are resumed in table 5.1.

Unlike a typical turbine blade, this fan blade is not defined by one or a set of previously known airfoils, such as the airfoil shape variable along the radius. Therefore, the number of airfoils to be extracted from the model along the radius has to be chosen in order to describe effectively the fan blade shape inside the aeroacoustic tool.

In a first approach, the intention was to gradually increase the number of extracted airfoils and compare the geometry produced by the tool with the original geometry by overlapping them, but since the formats of the information of both geometries are widely different, it was not possible to introduce them simultaneously in the same context.

An alternative method was chosen, where an image of the top view of the blade was scanned in such a way that a set of points for each edge of the blade was obtained, as shown in figure 5.2. A coordinate system was temporarily set, with the x axis coincident with the axis shown in the figure and the y axis being in the vertical direction. Then, the distance between points with the same x coordinate

	Radius (m)
Hub	0.0733
Fan	0.225

Table 5.1: Fan and hub radius.

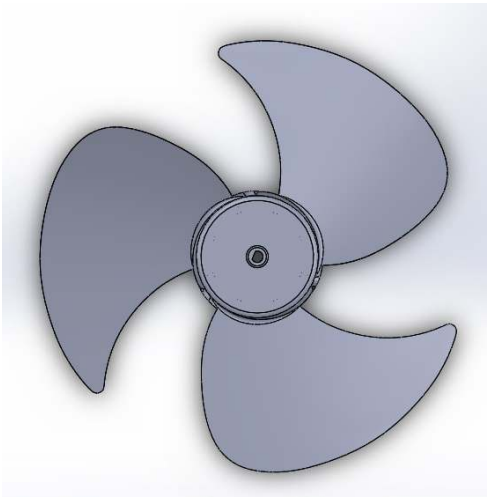

(a) Frontal view

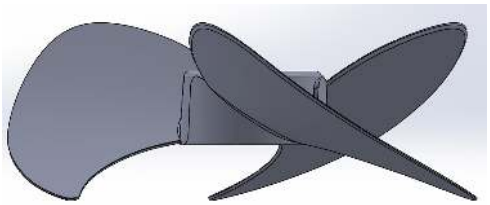

(b) Lateral view

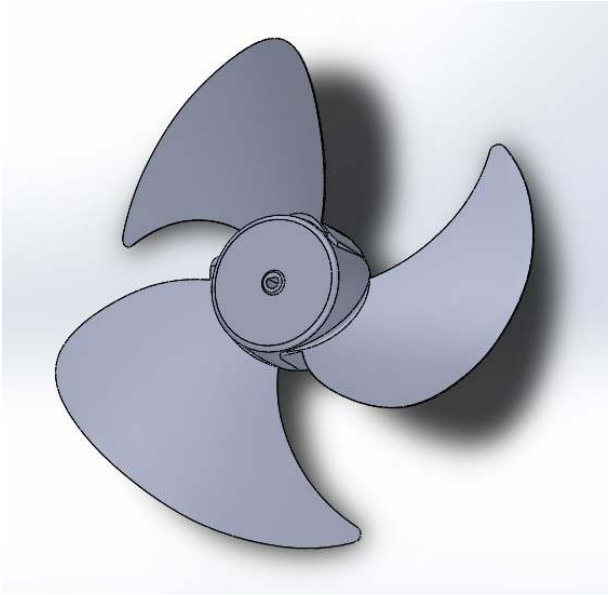

(c) 3D view

Figure 5.1: Views of the baseline fan model.

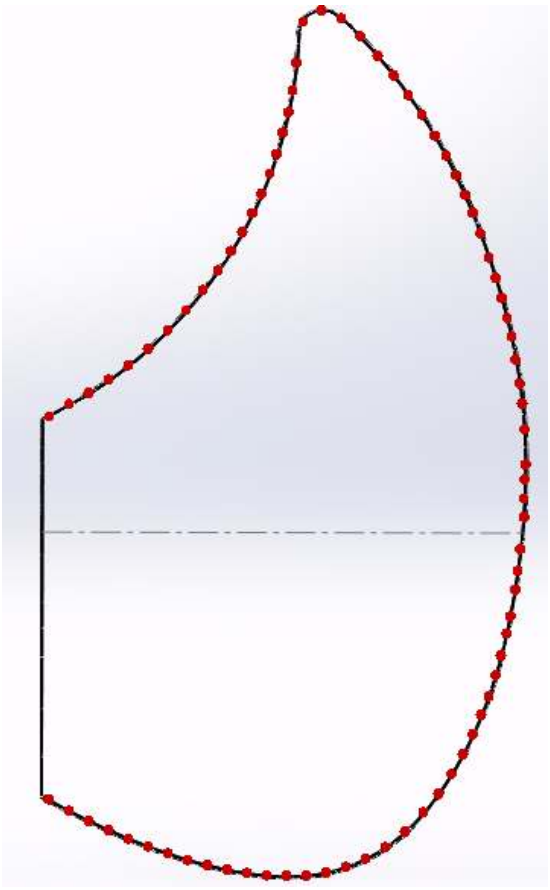

Figure 5.2: Set of points used to estimate the minimum number of extracted airfoils.

Bézier curve order	Frobenius Norm
2	0.0180
3	0.0111
4	3.5527E-15
5	3.4262E-14
6	2.5864E-14

Table 5.2: Results of Bézier curve fits to determine the number of extracted airfoil sections.

was computed in order to have a set of values which translate the distance between the two edges along the radial coordinate.

Using the algorithm referred in Chapter 4, a Bézier curve was fitted to these sets of points with the intent of finding the minimum order of the curve which has the best possible fit with the data. This way if, for example, a 2nd order Bézier curve has a satisfactory fit, it is only necessary 3 control points, or 3 airfoils, in this case, to describe the distance between the edges of the blade.

In table 5.2, the results of a series of tests to fit a Bézier curve to the data are shown. It can be seen that between the 3rd and 4th order, there is a considerable decrease in the Frobenius norm, while in the 5th and 6th order the norm increases, although having values of the same magnitude as the 4th order norm. Since the order with the lowest norm is the 4th, this Bézier curve order is the one which produces the best fit to the blade curvature, with 5 control points. Therefore, 5 airfoil shapes were extracted along the radial position and introduced into the aeroacoustic tool in order to replicate the original geometry.

(a) Airfoil 1 (r/R = 0.33)

(b) Airfoil 2 (r/R = 0.49)

(c) Airfoil 3 (r/R = 0.72)

(d) Airfoil 4 (r/R = 0.82)

(e) Airfoil 5 (r/R = 0.93)

Figure 5.3: Airfoil sections extracted from the blade.

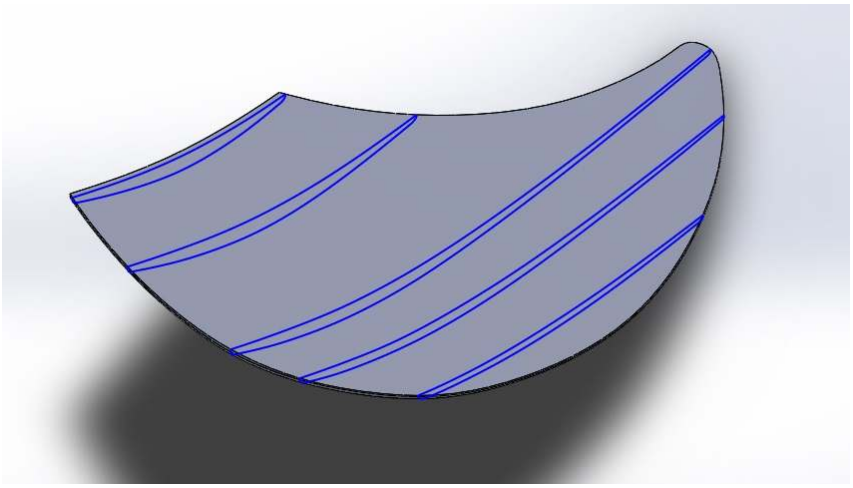

Figure 5.4: Location of extracted airfoils in the blade model.

Before the extraction of the airfoil sections, the leading edge of the blade had to be changed, by rounding it with a radius of 0.1 mm. The reason behind this is explained in Section 5.2. The sections were obtained by sectioning the model in Solidworks and by scanning the image in the same way as before and obtaining a set of points which described each section, being these points saved in a .dat file to input in the code. All of the airfoils are normalized to unit chord. The extracted airfoils and their location in the blade are shown in figures 5.3 and 5.4.

Since the tool has the option of inputing the chord and twist distributions as a Bézier curve, the chord and twist of each airfoil were measured and using once again the Bézier fitting algorithm used throughout this work, two Bézier curves were obtained which translate the blade chord and twist distributions.

The process of building the geometry of a blade includes the connection of the airfoil shapes using an invisible reference line that passes through a specified point on each of the airfoil shapes. Per default,

# of Airfoil	% chord
1	71.5
2	64.45
3	42.8
4	43.33
5	40.39

Table 5.3: Locations of the points in each airfoil upon which the reference line used to build the blade passes through.

Parameter	Value
Number of blades	3
Rotational speed (rpm)	850
Axial flow velocity (m/s)	10.55
Trailing edge angle (deg)	2
Turbulence intensity (%)	2
Turbulence length scale (m)	0.002

Table 5.4: Parameters used in baseline fan aeroacoustic analysis.

this point is located as 25% of the chord from the leading edge, but it can be defined as input from the user. In this case, these points were calculated and extracted from the model for each section. The locations of these points, expressed in percentage of chord, are presented in table 5.3.

With all of the geometric parameters defined and introduced in the code, the final blade geometry was produced by the program. A reproduction of the model with 30 control sections equally spaced is shown in figure 5.5. Two views from two different perspectives are presented.

5.2 Aeroacoustic Analysis

With the blade geometry defined, an aeroacoustic analysis was executed to characterize the nominal noise levels of the fan. The analysis parameters are shown in table 5.4. The turbulence parameters are merely indicative, being adjusted to correlate with the experimental data in Section 5.3.

Before the analysis could be executed, it was necessary to supply the aerodynamic polars for each extracted airfoil to the code in order for the BEM code to have the required data to compute the induced velocities along the blade radius. Since it is linked to this tool, XFOIL was used to obtain these aerodynamic polars.

In Section 5.1, it was referred that the blade leading edge had to be rounded. This is due to the fact that the original supplied geometry had a sharp-cornered leading edge, which implies airfoil sections with sharp-cornered leading edges. Since the panel code used in XFOIL to predict the aerodynamic coefficients of airfoils is highly sensible to the smoothness of the leading edge and the distribution of points (or panels) in this area, it was unable to analyze the original airfoils. Hence the change in the blade geometry, which, nonetheless, will not introduce an error factor when comparing the results with the experimental data since the curvature radius is very small when compared to the length scale of the airfoils, as it can be seen in figure 5.6, where a distance of 1 mm is presented for scale comparison.

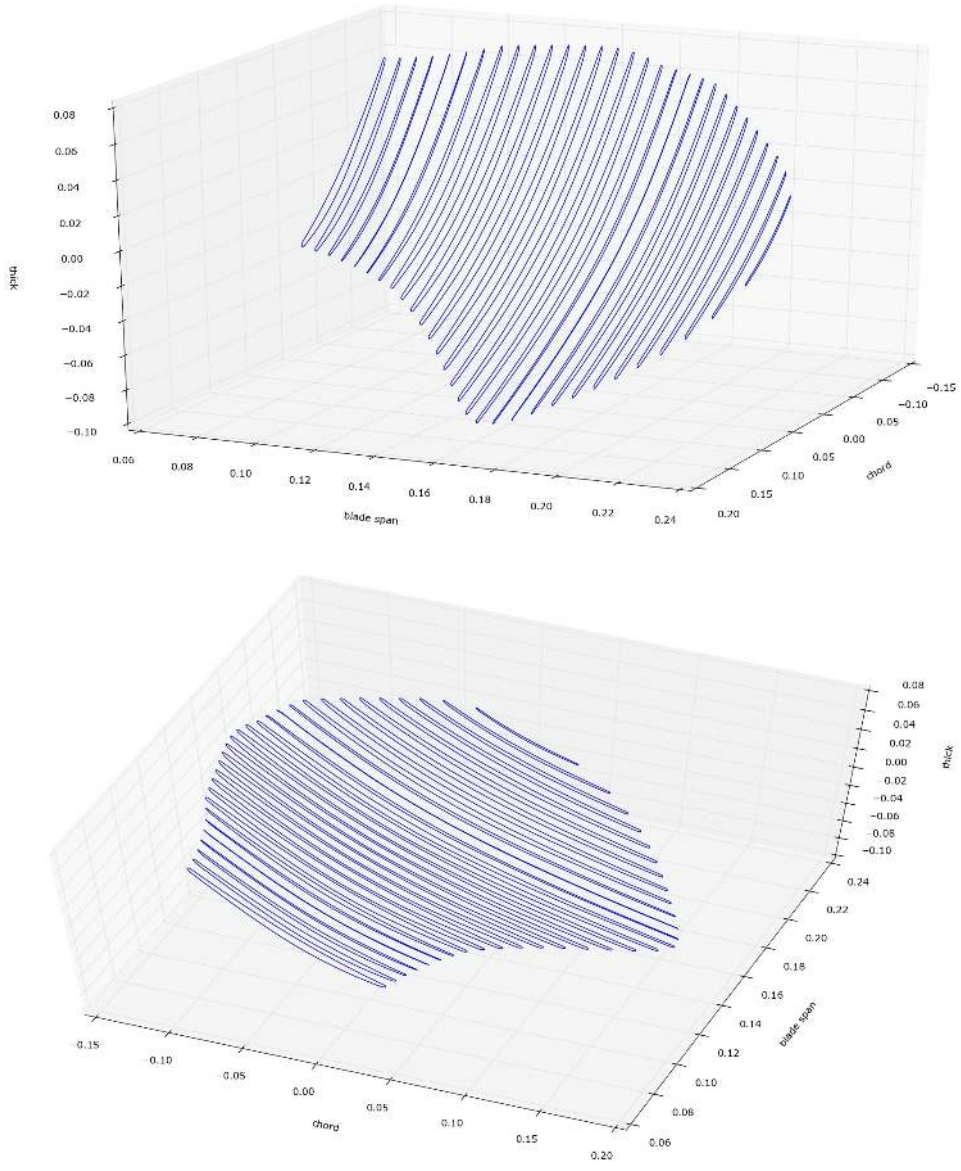

Figure 5.5: Blade geometry produced by the aeroacoustic tool.

(a) Airfoil full view

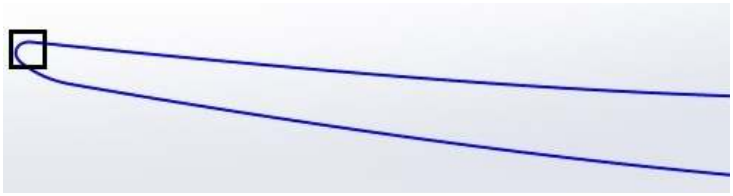

(b) Airfoil 1/4 chord view

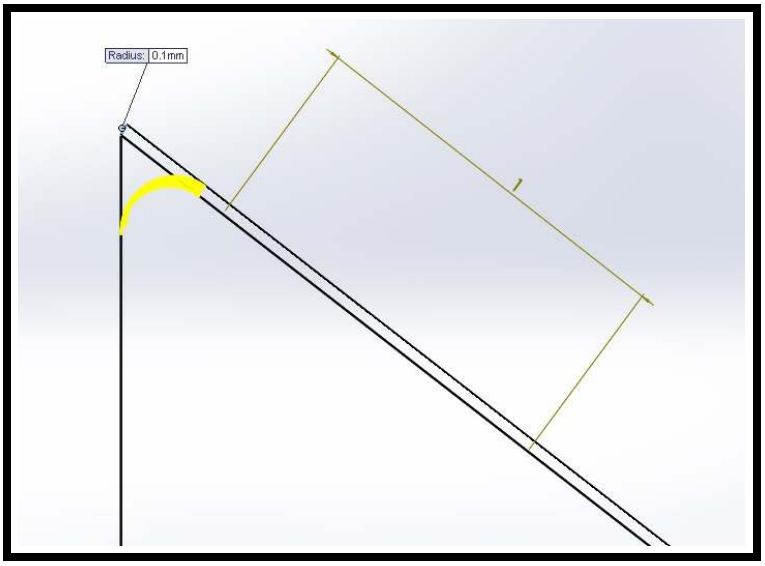

(c) Magnified view of the airfoil leading edge

Figure 5.6: Comparison between original and modified blade geometry.

With this new geometry, the required polars were computed and introduced in the code and the analysis was executed.

The two models referred in Chapter 3 were used in two different analysis in order to choose which one produces the results closest to the experimental data. The results obtained and the correlation is done in the following section.

5.3 Experimental Correlation

In this section, the experimental results to which the noise predictions are correlated were obtained from a floor standing AC unit with two fans, as the one shown in figure 5.7. The supplied experimental spectra were measured by three microphones with the layout presented in figure 5.8. Each microphone was labeled with a channel number, ranging from Channel 9 to Channel 12 and in this section, the measurements which will be taken as the baseline are the ones obtained by Channel 10.

It is assumed that the two fans are noise sources with a mutually incoherent sound radiation and have the same intensity, therefore the total noise produced by both fans can be obtained by adding 3 dB(A) to the results computed by the tool. Following this reasoning, all of the results presented in

Figure 5.7: Example of a floor standing AC unit (Copyrighted by LG).

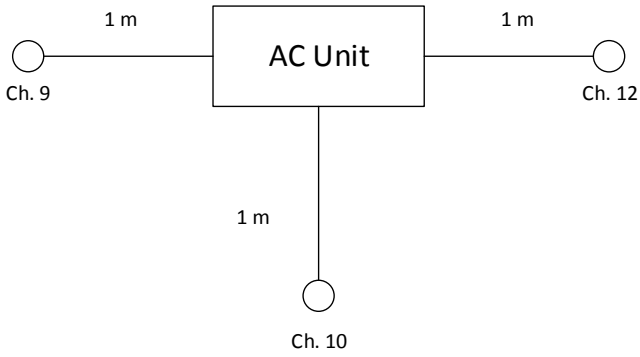

(a) Top view

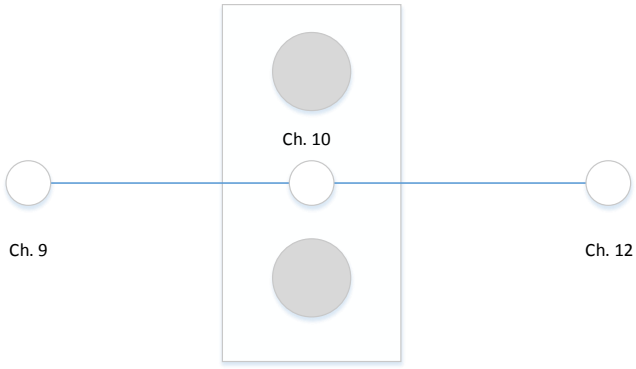

(b) Front view

Figure 5.8: Schematic of the experimental setup for the supplied data.

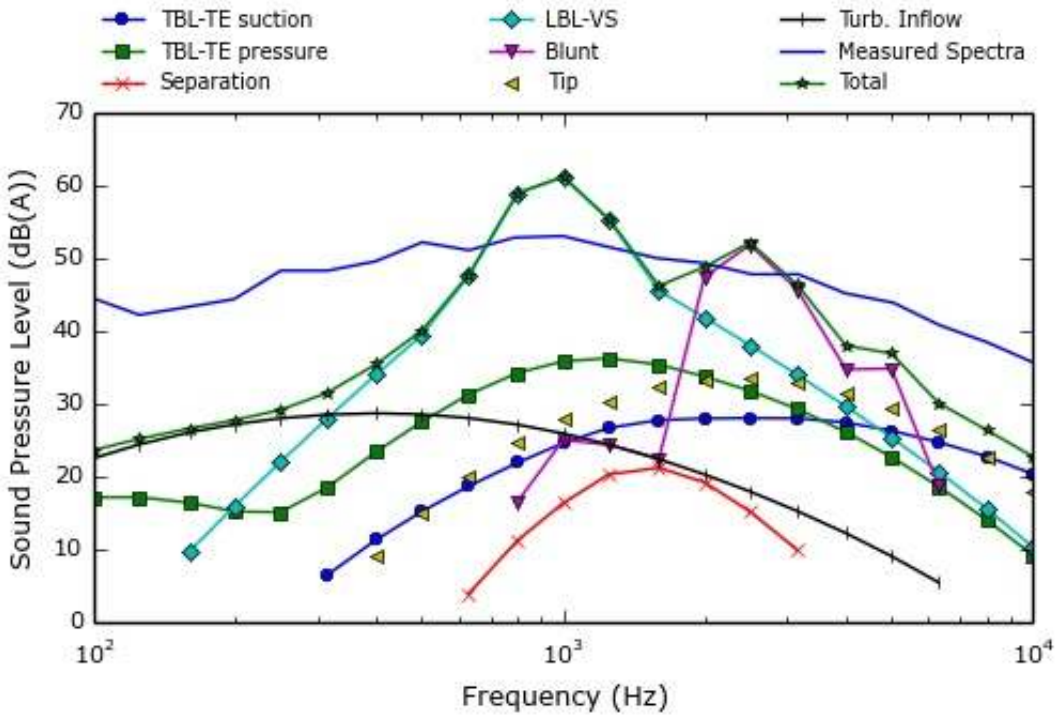

Figure 5.9: Sound power spectra of the fan using the first method from Chapter 3.

this section refer to the two fans combined, with the observer position being defined in the mid-plane between the two fans and 1 meter away from the AC unit, as represented by the Ch. 10 microphone in the experimental schematic.

The first method to be used is the one which includes an higher number of noise mechanisms and the results are shown in figure 5.9. Unlike the results presented in Chapter 3, the noise spectra shown in this section are in dB(A), to abide by the units in which the supplied experimental data are measured. Also, no data related to the turbulent conditions upon the experimental tests is provided. Therefore, the turbulent inflow noise will be used as one of tuning variables by changing the turbulent intensity and length according to the obtained correlation.

At a first glance, there are two visible spikes created by the LBL-VS and Blunt noise mechanisms in the mid-to-high frequency range. A possible explanation for the latter spike resides in the strong and sudden reduction of the blade chord towards the tip of the blade, which increases the thickness to chord ratio, contributing to the bluntness noise.

It can be seen that the noise is underpredicted until 600 Hz, with a slight overprediction due to the already referred spikes, and from 3000 to 10000 Hz it is again underpredicted. The main two reasons for these differences are the low turbulent inflow noise and the LBL-VS noise spike, with emphasis on the former. Therefore, a second analysis was executed where the turbulence parameters were changed to higher values, more specifically, 21.3% and 10 mm for turbulence intensity and length, respectively, in order for the noise prediction to become higher. These parameters are inside the range of values for the RPG2 grid configuration (refer to table 2.2), which is a typical configuration for outdoor AC units. The results of the new analysis are shown in figure 5.10.

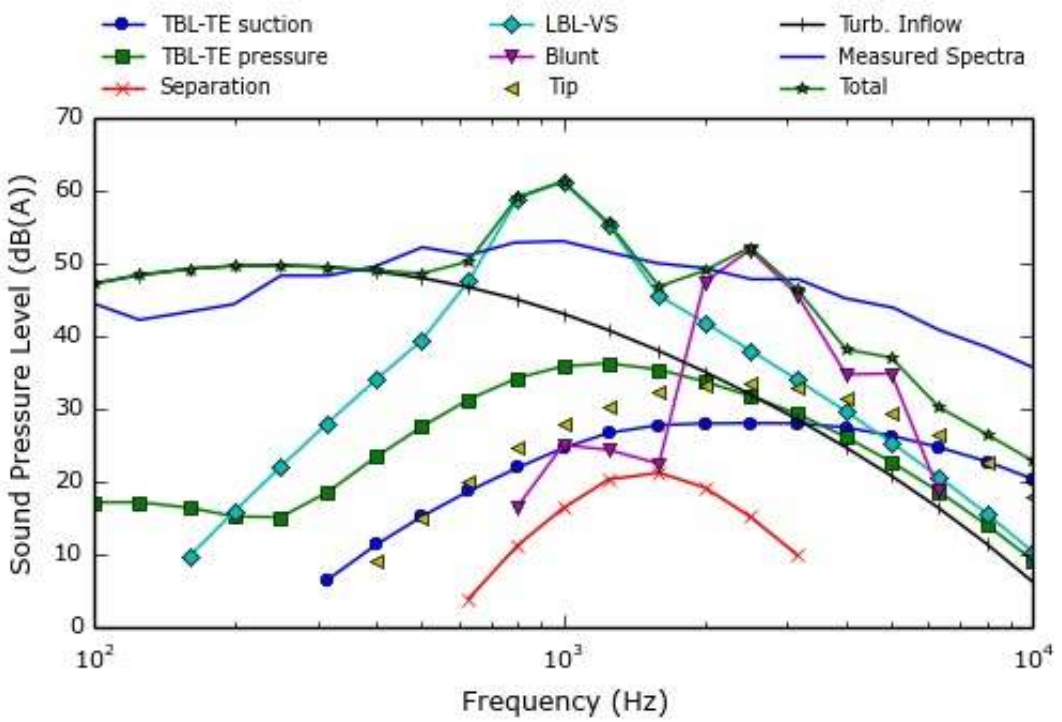

Figure 5.10: Sound power spectra of the fan using the first method with turbulence corrections.

The overall correlation with the experimental results is acceptable, although there are discrepancies in the mid and high frequency zone. In the latter case, there is nothing that can be done to improve the correlation, but in the mid-frequency case, it can be seen that the LBL-VS mechanism is responsible for the overprediction in this area. So, a third analysis where this mechanism is not considered is executed, being the results shown in figure 5.11.

Without the LBL-VS spike, the discrepancy between the noise prediction and the experimental results in the mid-frequency area is still visible, although in this case, the noise is underpredicted. Since the value of the discrepancy similar in both cases, the criteria to choose the method has to be the predicted OASPL and it has to be compared to the experimental. This comparison will be presented after the second method is tested.

In figure 5.12, the results of the second, simpler method are shown. The turbulence parameters from the last analysis were maintained.

Although the discrepancy in the low frequency zone is acceptable, the correlation in the remaining spectrum is not satisfactory, with differences of the order of 20 dB(A) between the predicted and the experimental results. Since the turbulent inflow noise is the only tuning parameter in this method and the turbulent parameters are already in its maximum, the correlation cannot be improved.

In table 5.5, the values of OASPL obtained by the two variations of the first method and the second method are presented, along with the error when compared to the OASPL supplied by the air conditioning manufacturer of 61.4 dB(A).

Since the first method, without the LBL-VS noise mechanism, has the lowest error and it takes into account an higher number of noise mechanisms, it will be the chosen method for the subsequent studies

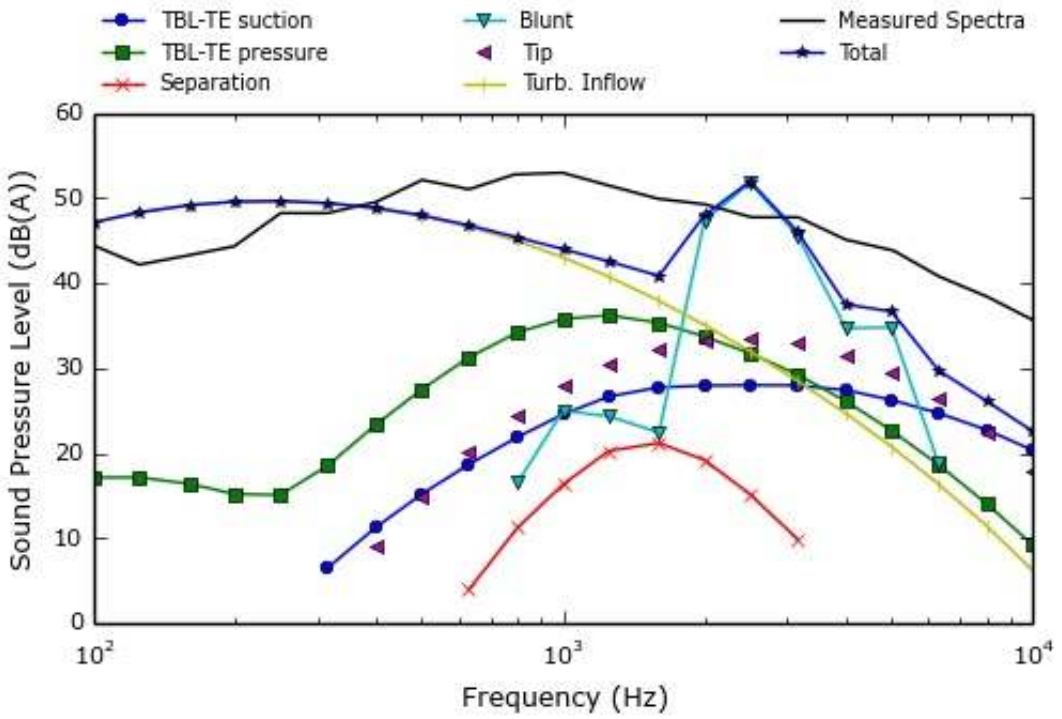

Figure 5.11: Sound power spectra of the fan using the first method without LBL-VS noise mechanism and with turbulence corrections.

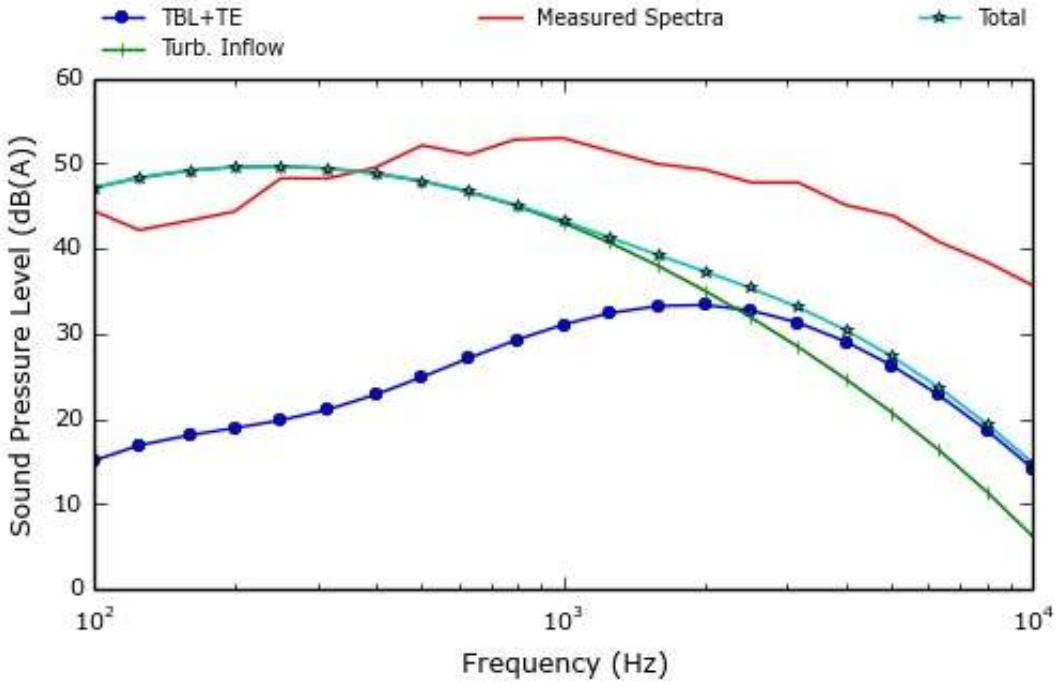

Figure 5.12: Sound power spectra of the fan using the second method from chapter 3.

Method	OASPL (dB(A))	Error (%)
First (with LBL-VS)	65.5	6.67
First (without LBL-VS)	60.1	2.12
Second	58.7	4.34

Table 5.5: OASPL calculated by the considered methods and comparison to nominal OASPL.

of the fan.

Chapter 6

Geometrical Parametric Study

With the noise model chosen and the baseline values defined, a study on the impact of the variation of the fan diameter and number of blades in the produced noise was conducted. Three cases were considered: one where the baseline number of blades is maintained and the diameter is changed, other with the baseline diameter unchanged and variation of number of blades and the last with a simultaneous change in both geometrical variables.

6.1 Fan Diameter

In order for the blades to be geometrically similar while changing the fan diameter, the hub and blade tip radius were changed by the same ratio, maintaining the distance between the two blade extremities. Also, the baseline twist and chord distributions were translated by the same factor applied in the hub and blade tip. Therefore, the relative distance between the control sections and points was kept unchanged along with the respective chord and twist values, being only their radial coordinate the parameter to be altered.

While changing the fan diameter, the volumetric air flow has to be constant. Therefore, an increase or decrease in the diameter translates in a decrease or increase in the axial velocity, according to

$$V = \frac{1.5}{\pi(R_{tip}^2 - R_{hub}^2)} \quad , \tag{6.1}$$

where V is the axial velocity,R_{tip} and R_{hub} are the tip and hub radius, respectively and the value of 1.5 is due to the design imposition of maintaining a volumetric flow of 1.5 m^3/s.

These changes also imply that the power consumed by the fan is unaltered, being the decrease of the fan rotational speed a consequence of the increase of the diameter. The relation between these two variables can be obtained using dimensional analysis, resulting in the relation of proportionality between the fan power and the following expression,

$$P \sim \rho N D^5 \Omega^3 \quad , \tag{6.2}$$

with ρ as the air density, N as the number of blades, D as the diameter and Ω as the rotational speed.

Therefore, for the same consumed power, the relation between the rotation speed of a fan 1 and a fan 2 is given by

$$\Omega_2 = \Omega_1 \left(\frac{N_1}{N_2} \frac{D_1^5}{D_2^5} \right)^{1/3} \quad . \tag{6.3}$$

Since in the present case, the number of blades stays the same, equation (6.3) reduces to

$$\Omega_2 = \Omega_1 \left(\frac{D_1}{D_2} \right)^{5/3} \quad . \tag{6.4}$$

Using the presented expressions, the rotational speeds and axial velocities used in the analysis for each diameter value were obtained and are presented in table 6.1. The diameter was changed in the range from 400 mm to 600 mm. The values for the baseline fan are shown in bold.

Diameter (mm)	**Axial velocity (m/s)**	**Rotational speed (RPM)**
400	12.68	1034
450	**10.55**	**850**
470	9.89	791
500	9.04	713
550	7.9	608
600	7.02	526

Table 6.1: Axial velocity and rotational speed values for different fan diameters.

After inputing these parameters and making the necessary geometrical changes in the aeroacoustic tool, the noise predictions were obtained and are shown in table 6.2. The noise spectra for each diameter are presented in figure 6.1. The values for the baseline fan are shown in bold.

Diameter (mm)	**Noise (dB(A))**
400	64.96
450	**60.09**
470	58.49
500	56.91
550	55.34
600	54.16

Table 6.2: Noise predictions for various diameters.

The increase in diameter translates into a decrease in the produced noise and a reduction of 5.9 dB(A), which equals 9.6 %, is obtained for a diameter of 600 mm when compared to the baseline case of 450 mm.

When analyzing the spectra comparison, it can be seen that the peak observed originally at around 2500 Hz for the 450 mm diameter, descends to lower frequencies with the increase of diameter. This can be explained by the fact that the wavelength of the fundamental vibration mode of a body is proportional to its dimensions, therefore for a bigger fan, the wavelength is higher and the frequency is lower.

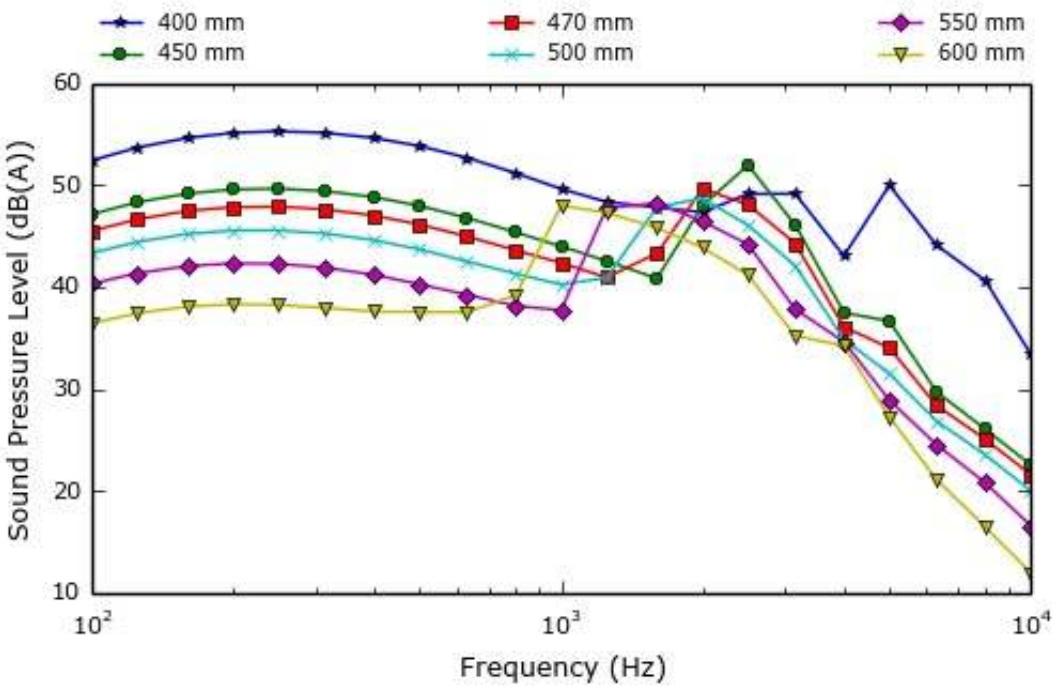

Figure 6.1: Sound pressure level spectra for each fan diameter.

6.2 Blade Number

When the number of blades is changed, the equivalent blade area has to remain the same in order for the comparison to be valid or else it would be added additional area that was not in the fan initially. This implies that for an increase in the number of blades while maintaining the diameter, the mean blade chord has to decrease.

Therefore, the following relation between the blade chord c and the number of blades N of two fans 1 and 2 was used:

$$c_2 = c_1 \frac{N_1}{N_2} \quad . \tag{6.5}$$

From equation (6.5), the chord values of the 5 control sections for each fan with different number of blades were obtained. A Bézier curve was fitted in these values, in order to obtain the new chord distribution of the new blades, following the same procedure used in the baseline fan.

Similarly to the fan diameter, a change in the number of blades also affects the rotational speed if the consumed power is to be the same, as shown by equation (6.3). For a constant diameter, the equation used is

$$\Omega_2 = \Omega_1 \left(\frac{N_1}{N_2} \right)^{1/3} \quad . \tag{6.6}$$

The range of study for the number of blades was from 3 to 6 blades and the baseline diameter of 450 mm was used. The rotational speeds used in each analysis are presented in table 6.3, the predicted noise is shown in table 6.4 and the noise spectra for each number of blades are present in figure 6.2. The baseline values are shown in bold.

Number of blades	Rotational speed (RPM)
3	**850**
4	772
5	717
6	675

Table 6.3: Rotational speeds for different number of blades.

Number of blades	Noise (dB(A))
3	**60.1**
4	60.1
5	58.9
6	58.4

Table 6.4: Noise predictions for different number of blades.

Similarly to the effect of the increase of diameter, the increase of blade number reduces the produced noise, although the magnitude of the reduction is lower than the observed when increasing the diameter. With 6 blades, a noise reduction of 1.7 dB(A) was obtained, which translates into a variation of 2.8%.

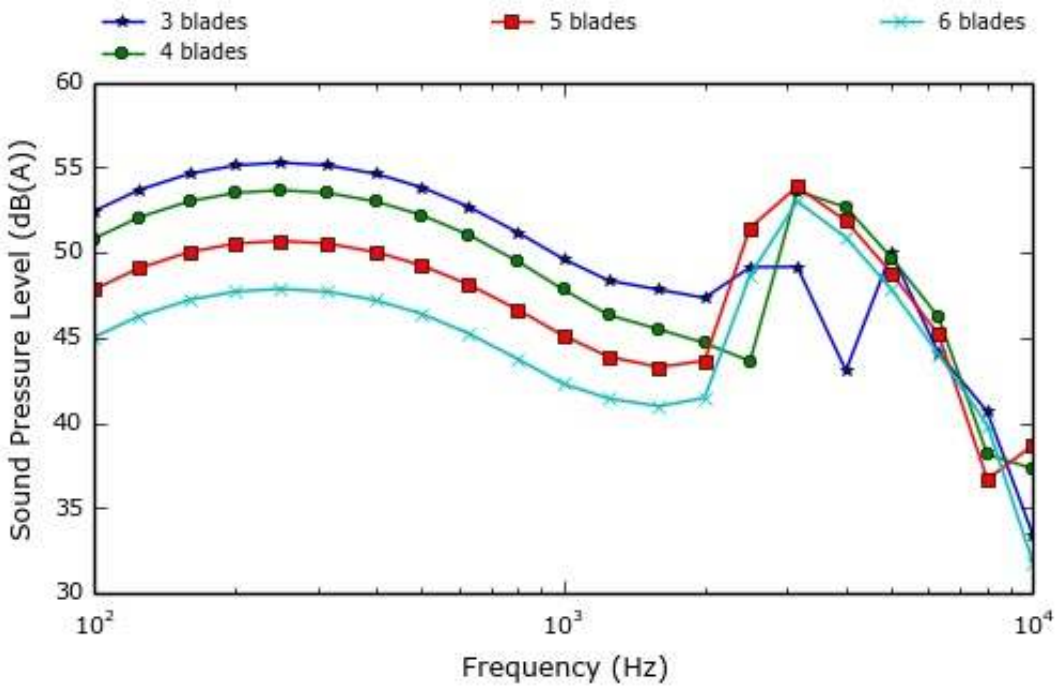

Figure 6.2: Sound pressure level spectra for each blade number.

When comparing the noise spectra, it can be noted that the peak observed around 3000 Hz stays relatively unchanged, with the exception of the 3 blades case. This can be explained following the same reasoning presented in Section 6.1, since only the number of blades is altered, hence the characteristic dimensions of the fan are unchanged and the frequency where the peak manifests itself is the same. Therefore, the main reason for the noise reduction is found in the low-to-mid frequency zone, where the dominant noise mechanism, the turbulent inflow noise, is decreased along with the increase in the

number of blades.

6.3 Fan Diameter and Blade Number

Using all of the relations presented in the previous sections, a parametric study where the two variables present in this chapter are changed simultaneously was conducted. The rotational speeds used for each pair of variables are shown in table 6.5 and the respective noise predictions are presented in table 6.6. Also, the baseline values are shown in bold.

Diameter (mm) \ **Blade number**	3	4	5	6
400	1034	940	872	821
450	**850**	772	717	675
470	791	718	667	628
500	713	648	602	566
550	608	553	513	483
600	526	478	444	418

Table 6.5: Rotational speeds (RPM) for different number of blades and diameters.

Diameter (mm) \ **Blade number**	3	4	5	6
400	65.0	64.0	62.1	60.0
450	**60.1**	60.1	58.9	58.4
470	58.5	57.1	59.1	58.6
500	56.9	58.1	57.6	57.2
550	55.3	54.8	53.8	52.3
600	54.2	52.5	51.1	50.2

Table 6.6: Noise predictions (dB(A)) for different number of blades and diameters.

The conclusions inferred from the previous sections agree with the presented values, although there are some exceptions. For the 470 mm diameter, there is an increase of noise from 4 to 5 blades and the same is verified for the 500 mm diameter and from 3 to 4 blades. However, it can be seen that in a general sense, the increase in fan diameter and number of blades results in a reduction of the produced noise, being possible to reduce it up to 16.5%.

Along with the noise, it was also possible to compute the fan efficiency for each case, being the results presented in table 6.7.

Diameter (mm) \ Blade number	3	4	5	6
400	14.4	9.8	4.7	3.6
450	**22.2**	13.2	27.2	3
470	22.7	10	5.6	2.1
500	25.5	30.5	11.3	1.8
550	24.7	33.1	3	1.7
600	29.5	18.2	3.1	2

Table 6.7: Fan efficiency (%) for different number of blades and diameters.

In a general sense, an increase in diameter results in an increase on efficiency, while an increase in blade number impacts it negatively, although there are some inconsistencies, as in the noise predictions. There is a raise in efficiency when the blades increase from 4 to 5, in the 450 mm diameter case, and from 3 to 4, in the 500 and 550 mm diameter cases. These deviations can be explained by reduction in rotational speed and chord when the blade number increases and by the reduction in axial flow velocity when the diameter increases, because lower chords and lower speeds lead to stall being achieved more quickly, which introduces imprecisions in the calculations. Nonetheless, the final results refer to the averaged sum of all blade elements and therefore, they are trustworthy.

The low efficiency values are explained by the following logic; both diameter and blade number changes are applied with the assumption that the power consumed by the fan stays the same, which coupled to the reduction of rotational speed, implies that the torque increases. Also, with the blade number increase, the blade chord decreases. From equation (2.59), it can be seen that with the reduction in rotational speed and chord, while maintaining the axial flow velocity, the inflow angle has to decrease in order for the torque to increase. Referring to equation (2.55), the only way to decrease the inflow angle, with decreasing rotational speed, is to decrease both the axial and radial induction factors. It can be seen that this decreases the produced thrust, by inspecting equation (2.58), which in turn decreases efficiency, with constant power and axial flow velocity (see equation (2.70)).

Combining tables 6.6 and 6.7, it is visible that the best trade-off solution lies between the 500 and 550 mm diameter and 3 and 4 blades.

Chapter 7

Aeroacoustic Fan Optimization

In this chapter, the final optimization of the fan will be performed. An overview of the existing optimization techniques and the choice of the method used in this work will be presented. The aeroacoustic optimization problem is defined in terms of constraints and design variables and finally, several optimization cases are set up and the respective results will be presented.

7.1 Numerical Optimization Techniques

Contrary to diameter and number of blades, the blade chord, twist and curvature are continuous variables and change with the radial coordinate, which turns a parametric study similar to the ones in chapter 6 a difficult task to perform. Therefore, a numerical optimization algorithm had to be chosen and applied to these variables in order to obtain a final solution.

In the field of numerical optimization, the available methods can be divided in two categories: deterministic and heuristic. Deterministic methods rely upon an analytical definition of the problem to generate a set of points which converge towards a local optimal solution, while heuristic methods mimic some of the phenomena found in nature to find the global optimal solution. Some examples of deterministic methods are Linear Programming, Nonlinear Programming or Sequential Quadratic Programming (SQP). The heuristic category includes methods such as Genetic Algorithms, Ant Colonies, Differential Evolution, Particle Swarm, etc. A thorough review of optimization methods can be found in [46].

Generally, heuristic methods are more powerful and flexible than deterministic methods and have the advantage of being iterative, not requiring an analytical definition of the objective function. However, they have an higher computational cost, the quality of the solution cannot be guaranteed and the probability of finding a global optimum solution decreases with the increase in design variables. Nonetheless, when a relation between the objective and the design variables cannot be analytically defined, an heuristic method is the best choice.

Given the advantages of genetic algorithms and their presence in many engineering single and multi-objective optimization problems [47], the NSGA-II [48] (Non-Dominated Sorting Genetic Algorithm) was the optimization algorithm chosen for the optimizations present in this chapter. It solves non-convex

and non-smooth single and multi-objective optimization problems. This algorithm was already used in multi-objective aeroacoustic optimization of wind turbine blades [49].

The NSGA-II is already included in pyOpt, a Python-based optimization framework used for formulating and solving nonlinear constrained (and unconstrained) optimization problems [50]. The advantage of using pyOpt is the fact that the process of establishing an optimization problem is as simple as defining a function which takes as input a vector with the design variables and outputs the objective functions(s) and constraint(s) to the optimizer. After the function is defined, the optimization problem can be initialized with the naming of the design variables and defining their constraints.

Convergence of the solution One of the input parameters in an optimization using genetic algorithms is the size of the population that is created in each generation. Another input is the number of generations, which functions as the stopping criteria for the optimizer. These two parameters influence the convergence of the solution, since if they are too low, the solution might not converge and there is still more leeway in the design space to achieve a better solution. However, if these numbers are too high, there can be a waste of computational resources, since the solution might already have converged, but the optimizer is still running until it reaches the maximum number of generations. Therefore, a convergence study was conducted for each optimization case in Section 7.3.

In [37], it was studied the impact of the population size in the convergence and on the running time. As expected, with the increase of the population size, the number of generations required to achieve convergence is lower, but the necessary number of function calls is higher. Since the CPU time is directly proportional to the number of function calls, it was concluded that a population size between n and $2n$ (with n as the number of design variables) can guarantee a converged solution with an efficient use of computational resources for a shorter runtime. Given that the basis of the work which led to this conclusion is similar to the basis of this work, this rule of thumb will also be applied in the subsequent optimizations.

7.2 Problem Definition

Every optimization problem consists on minimizing (or maximizing) an objective function, which is dependent of a set of design variables subject to a series of constraints. A typical mathematical formulation for these problems is

$$\begin{aligned} \underset{x}{\text{minimize}} \quad & f(x) \\ \text{subject to} \quad & g(x) \leq a_i,\ i = 1, \ldots, m \\ & h(x) = b_j,\ j = 1, \ldots, n \\ & x_k^L < x_k < x_k^U,\ k = 1, \ldots, p \end{aligned}$$

where $f(x)$ is the objective function, x is the design vector, $g(x)$ are the inequality constraints and $h(x)$ are the equality constraints. Each variable x_k in the design vector is constrained by a lower value x_k^L and by an upper value x_k^U. These are referred to as side constraints.

In the several optimization cases presented in the next section, there will be performed single and multi-objective optimizations of two objective functions: the overall produced noise (OASPL) and the fan efficiency (see Section 2.6.2). The design variables will be the location of the control points which compose the Bézier curves of the chord and twist distributions and the locations of the 5 control sections in terms of chord percentage in order to change the blade curvature. There will be no inequality and equality constraints and the side constraints for each design variable will be stated for each optimization case.

7.3 Optimization Cases

The optimization simulations were conducted on two fans: the baseline fan and an improved fan from the results obtained in Chapter 6, more specifically, the 550 mm diameter fan with 6 blades.

For each fan, the impact of the chord and twist design variables in minimizing the produced noise, maximizing the efficiency and in the trade-off between these two objective functions was studied separately. In the case of the curvature, only the impact in the noise was addressed, since one of the disadvantages of the BEM implementation is that each blade element is considered independent of the neighboring elements and thus the fan efficiency is unaffected by the change in the blade curvature.

Afterwards, it was assessed the effect of optimizing simultaneously the blade chord and twist for the two objectives, both mutually and exclusively. Finally, the chord, twist and curvature were optimized for minimizing the noise. The efficiency was not considered for the reasons already stated above.

The parameters for each analysis were the same as the ones used in Chapter 5, including the turbulence parameters and the observer position.

7.3.1 Baseline Fan

The noise and efficiency values of the baseline fan are presented in table 7.1 as reference for the comparison with the results.

Noise(dB(A))	**Efficiency (%)**
60.1	22.2

Table 7.1: Noise and efficiency values for baseline fan.

Chord The first optimization to be considered is the optimization of the blade chord. The chord distribution is defined by a 6^{th} order Bézier curve and since the locations of the curve control points are the design variables, except for the radial coordinates of endpoints, the total number of design variables for the chord optimization is 10.

In all analysis, the chord values and radial positions were constrained between 90% and 110% of

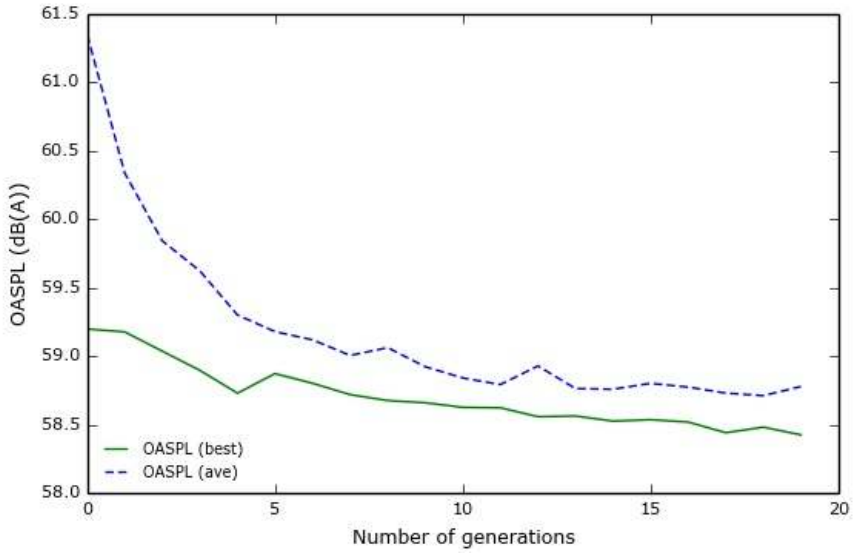

Figure 7.1: Variation of population average and best OASPL with the number of generations with chord as the design variable.

their initial values:

$$\begin{aligned} 0.9\ c_i^{initial} < y_i^{cp} < 1.1\ c_i^{initial} \\ 0.9\ \frac{r_i}{R_{max}} < x_i^{cp} < 1.1\ \frac{r_i}{R_{max}} \end{aligned} \tag{7.1}$$

The first objective was the OASPL and the optimization resulted in a decrease of the noise down to 58.42 dB(A). The convergence study is presented in figure 7.1 and it can be considered that the solution converges. The optimized chord distribution is shown in figure 7.2.

The new chord distribution translates into a blade with a lower chord, which was expected as the noise production for each element is a function of the boundary thickness parameters, which are proportional to the element chord. It is interesting to note that while up until the maximum chord at r/R = 0.77, the chord increase rate is the same as in the initial distribution, from the maximum until the end, the chord decreases in a more linear rate than the initial, with the reduction towards the end less sudden. This indicates that a smooth transition in the chord at the tip area is a factor to take into account when minimizing the noise.

Although this optimization did only account for the noise, the efficiency of the optimized fan was computed in order to assess the trade-off between the impact on noise and the aerodynamic impact. This optimization resulted in an efficiency decrease of 1.6%, with the optimized fan having an efficiency of 20.6%.

A second optimization was conducted, with the efficiency as the objective function. The optimization converged, as seen in figure 7.3, and resulted in an increase up to 26.1%. The optimized chord distribution is presented in figure 7.4. The optimized chord distribution is similar to the initial, although the maximum chord is lower, indicating that the original geometry is already near the optimal aerodynamic design. The overall reduction of the chord is explained by the fact that the chord is proportional to the consumed power by the fan, so that a reduction of chord implies an increase in efficiency. This increase

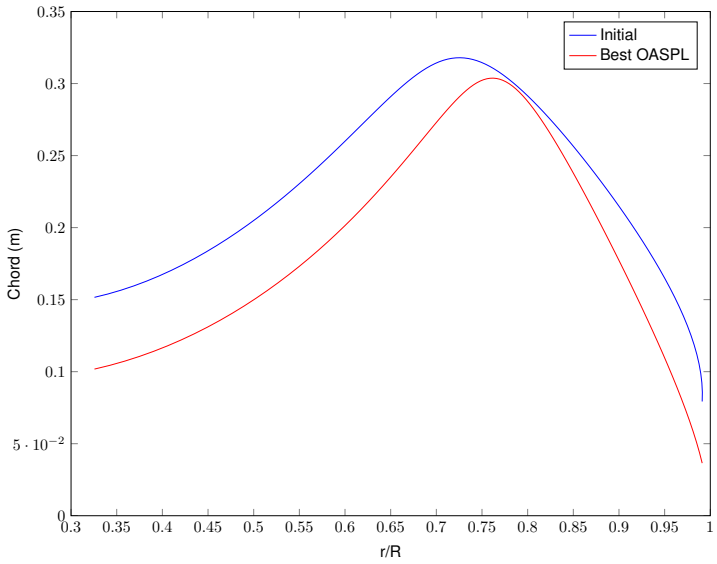

Figure 7.2: Comparison between the initial and the best OASPL chord distribution.

in efficiency also incurred into a decrease of 0.6 dB(A) to 59.5 dB(A).

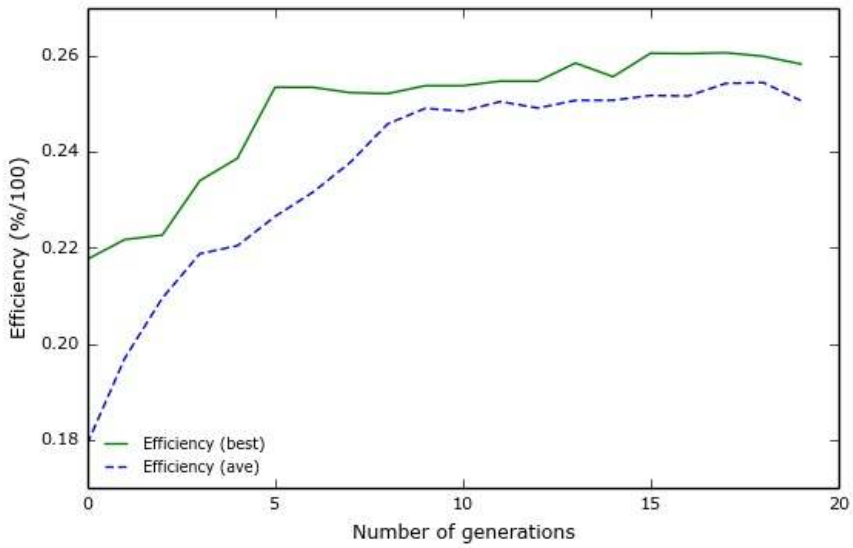

Figure 7.3: Variation of population average and best efficiency with the number of generations with chord as the design variable.

The final chord optimization had both the OASPL and efficiency as objective functions. The optimizer provided a set of solutions from a dispersed set and the resulting Pareto front is presented in figure 7.5. It is visible from the figure that there is room for improvement in minimizing the noise, even in the solution for the maximum efficiency. The trade-off solution results in an OASPL of 58.25 dB(A) and an efficiency of 26.4% and the respective chord distribution is shown in figure 7.6. The trade-off chord distribution is a combination of the previous distributions, with a lower maximum (and overall) chord value and a similar growth rate than the initial distribution.

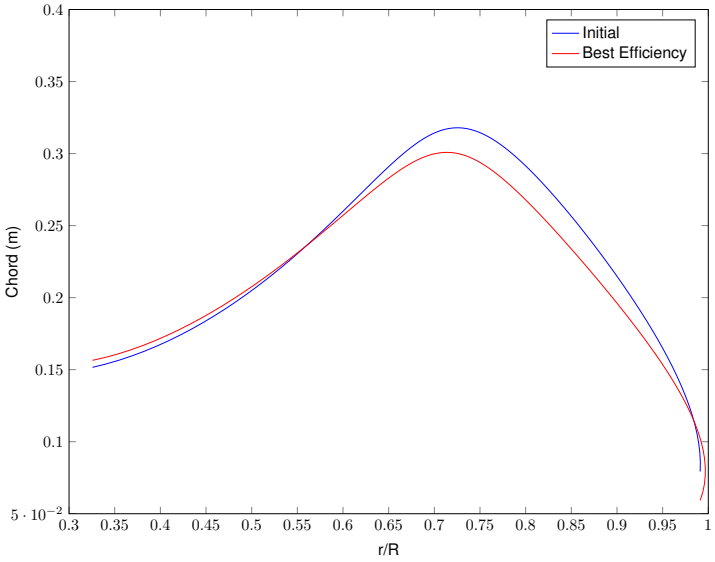

Figure 7.4: Comparison between the initial and the best efficiency chord distribution.

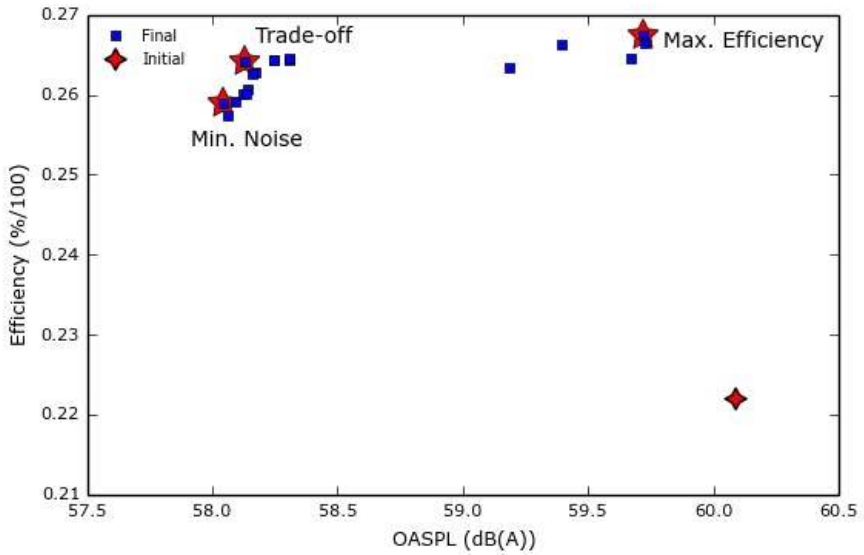

Figure 7.5: Pareto front in chord multi-objective optimization case.

Twist The second main design variable is the blade twist. The twist distribution is defined by a 5th order Bézier curve and the design variable procedure is the same as the one in the chord optimization, which results in a total number of 8 design variables.

In all twist optimizations, the twist values were constrained between 85% and 115% of their initial values, being the radial positions constraints the same as the ones in the chord optimization:

$$\begin{aligned} 0.85\ \theta_i^{initial} < y_i^{cp} < 1.15\ \theta_i^{initial} \\ 0.9\ \frac{r_i}{R_{max}} < x_i^{cp} < 1.1\ \frac{r_i}{R_{max}} \end{aligned} \tag{7.2}$$

Following the same procedure as in the chord section, the first objective function was the OASPL, being the convergence study shown in figure 7.7, resulting in a noise reduction down to 59.25 dB(A)

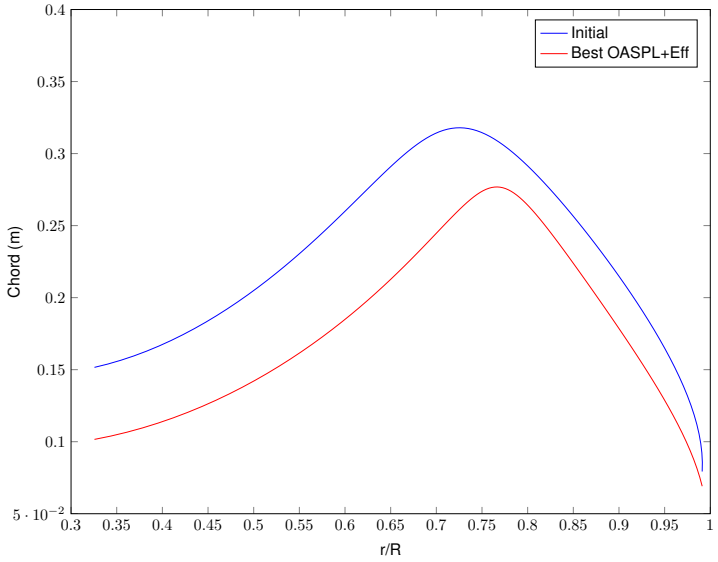

Figure 7.6: Comparison between the initial and the trade-off solution chord distribution.

and, consequently, in an increase of efficiency to 22.8%. The optimal twist distribution is presented in figure 7.8. It is visible that both distributions have a similar shape, with the optimized twist distribution having lower twist values than the initial distribution. The reduction in the twist also reduces the effective angle of attack along the blade radius, which explains the impact of minimizing the overall noise.

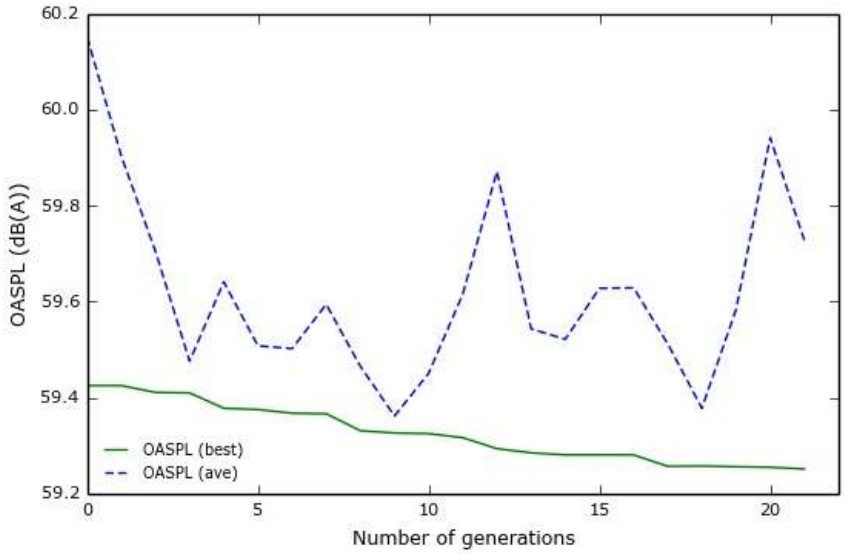

Figure 7.7: Variation of population average and best OASPL with the number of generations with twist as the design variable.

In the optimization for the efficiency objective function, the obtained results showed an increase of 2.3% to 24.5%, with the convergence study being presented in figure 7.9. The optimized twist distribution is shown in figure 7.10. There is an abrupt change in the twist around r/R = 0.7, from where it increases up to 34 degrees at the tip of the blade. The fact that this change happens around the tip area increases the torque, since it is proportional to the element radius, but the impact it has in thrust is higher than

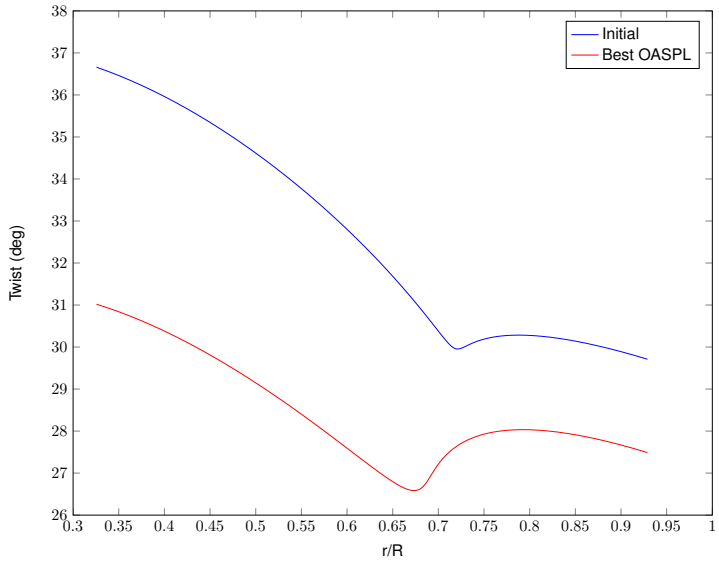

Figure 7.8: Comparison between the initial and the best OASPL twist distribution.

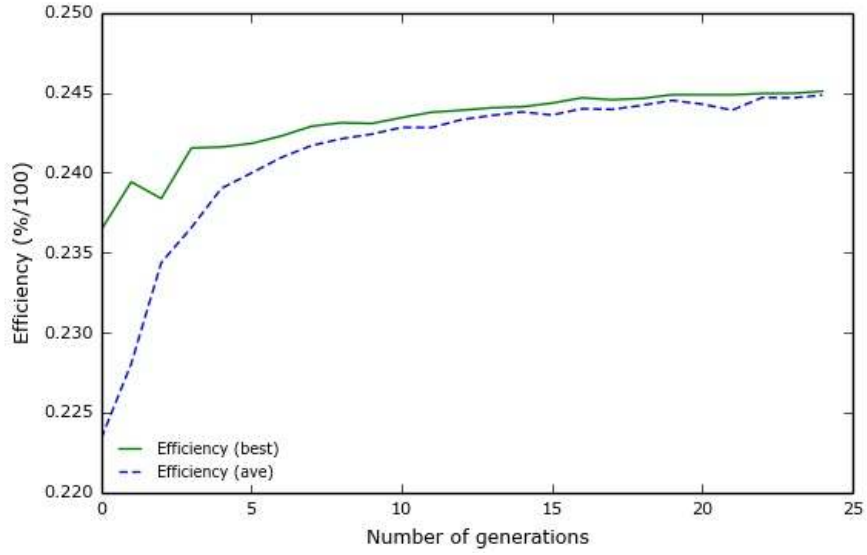

Figure 7.9: Variation of population average and best efficiency with the number of generations with twist as the design variable.

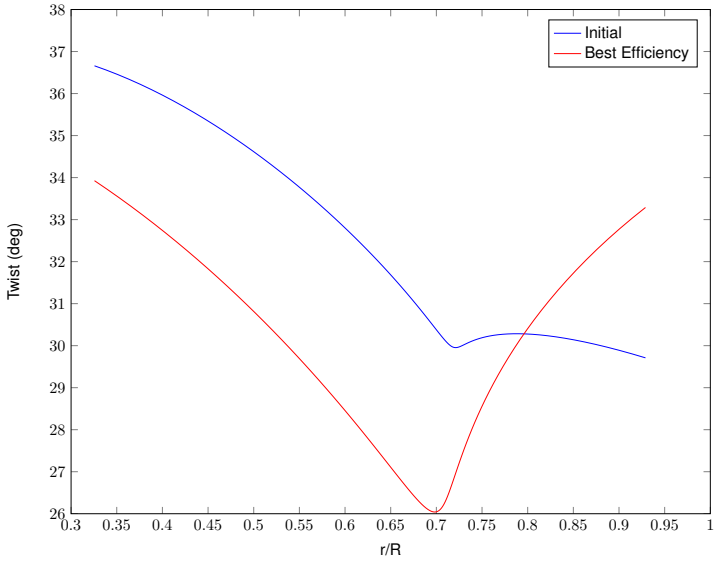

Figure 7.10: Comparison between the initial and the best efficiency twist distribution.

the increase found in the torque due to the increase in the effective angle of attack. Therefore, the ratio between thrust and torque is higher as well as the efficiency. However, since the highest levels of noise production are found in the tip area, this twist increase impacts negatively the noise, which is balanced by the lower twist around the hub area. In this case, the effect of the lower twist prevails since the overall noise was reduced to 59.76 dB(A).

In the twist optimization of both objective functions, OASPL and Efficiency, the optimizer produced a Pareto front which is shown in figure 7.11. As in the chord optimization case, it can be seen that even for the case of maximum efficiency, there is potential to improve the fan noise levels, although it only translates in a reduction of 0.3 dB(A). A greater reduction of almost 1 dB(A) is possible, with a penalty in the efficiency, although it is still observed an increase compared to the initial case.

The twist distribution for the trade-off solution is presented in figure 7.12. Since the trade-off solution is similar to the maximum efficiency solution, as seen in figure 7.11, it was expected that the twist distribution was similar as well, being observed a sudden increase in the twist at the tip area.

Curvature Curvature is the third and last design variable to use in the optimization process. For the reasons mentioned in the beginning of this section, the only objective function to be considered is the OASPL. The curvature is defined by the locations of the control sections, which are constrained between -10% and +10% of their initial positions expressed in chord percentage. The obtained results by the optimizer showed a minimal decrease to 60.03 dB(A) and the respective control sections locations are presented in table 7.2. In figure 7.13, the control sections are graphically represented, including the temporary axis upon which the section locations are measured. From the three main design variables, curvature is the one with a lesser impact in noise reduction, reducing it only by 0.1%. Adding that to the fact the difficulty of changing the manufacturing process when changing the blade curvature surpasses the minimal benefit in noise reduction, turning curvature into the less important of the three design variables.

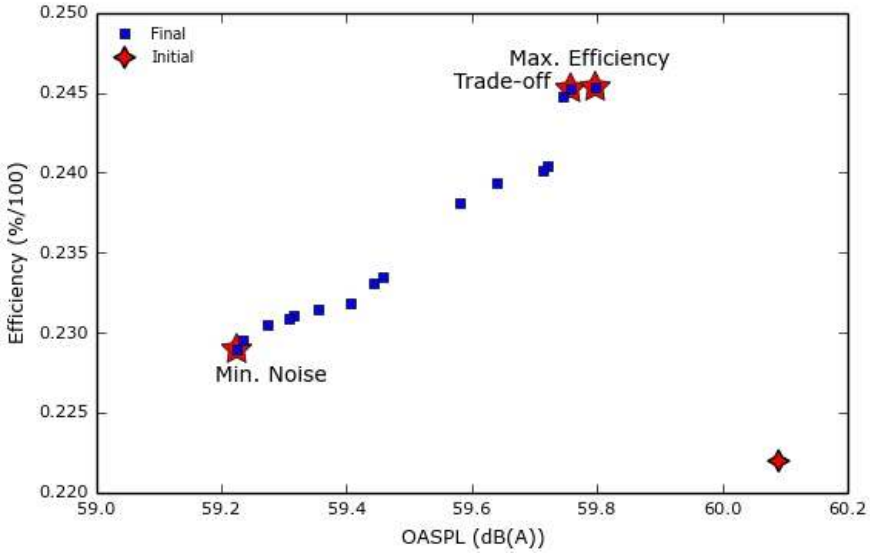

Figure 7.11: Pareto front in twist multi-objective optimization case.

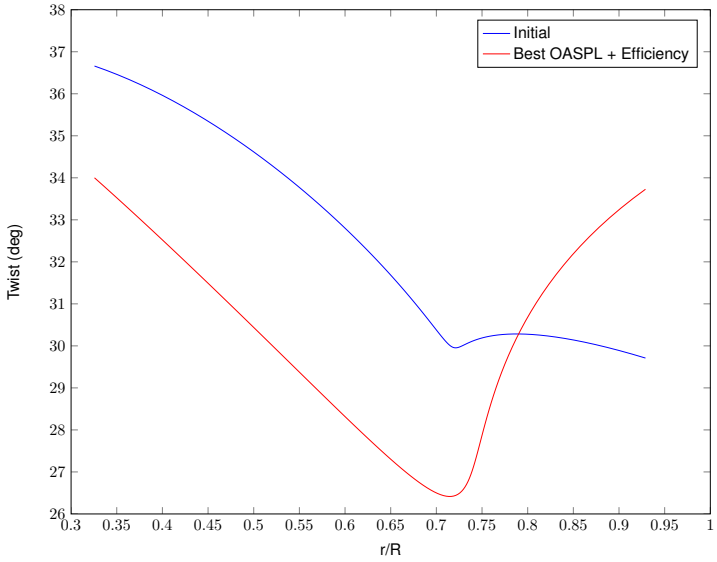

Figure 7.12: Comparison between the initial and the trade-off twist distribution.

# of Airfoil	Baseline % chord	Optimized % chord
1	71.5	79.54
2	64.5	72.3
3	42.8	43.06
4	43.33	37
5	40.39	34

Table 7.2: Curvature optimization results.

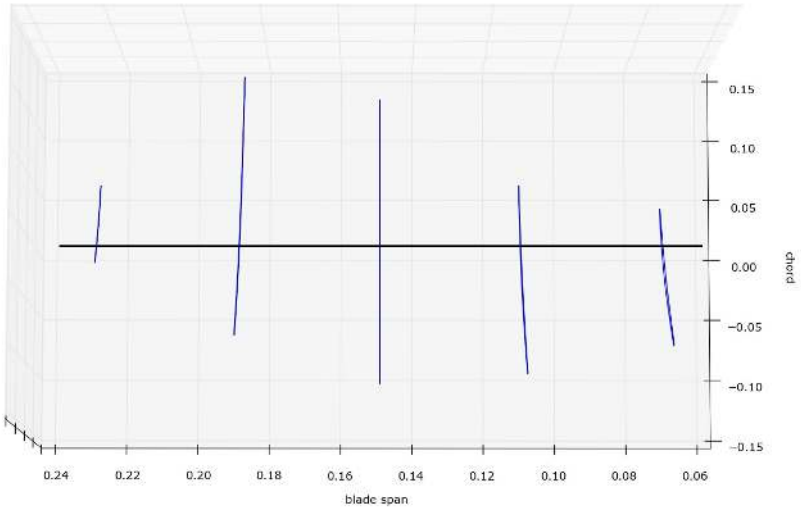

Figure 7.13: Optimized locations of the control airfoil sections.

Chord and Twist With the chord and twist being considered simultaneously as design variables, the solutions obtained by the optimizer for each objective function, separately, resulted in a decrease in OASPL of 4.1% to 57.61 dB(A) and in an increase in efficiency of 5.3% to 27.5%. The respective chord and twist distributions for each case are presented in figures 7.14 and 7.15.

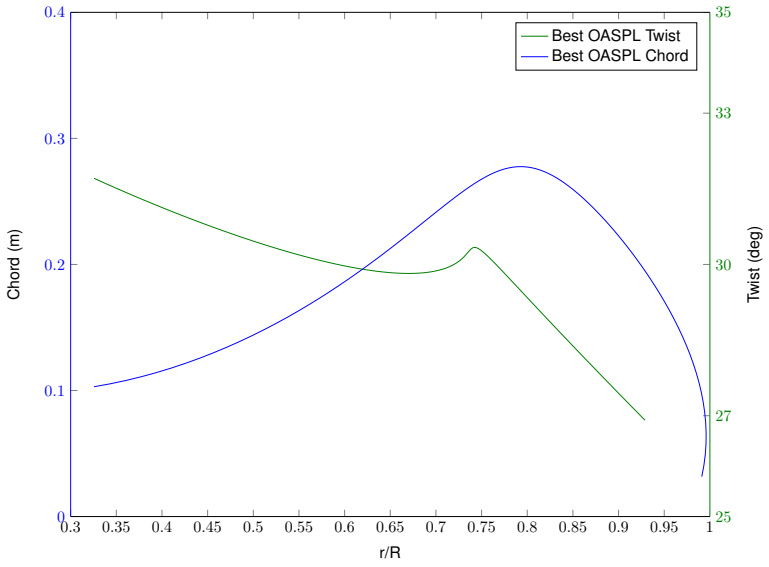

Figure 7.14: Chord and twist distribution for best OASPL.

The best OASPL distributions are similar to the best OASPL distributions for each separate design variable, with a slight increase in twist between r/R = 0.7 and 0.75, which proves that their combination takes advantage of their separate impact in minimizing noise.

In the best efficiency distributions, it can be seen that the tendency to increase twist towards the tip area is again present, like in the twist-only case, although there is a slight reduction in the proximity of the tip. The difference in the chord distribution in this case lies in the decrease rate between the maximum chord and the tip, being that in all other chord optimization results decreased slowly from the maximum and changed abruptly towards, while in this case the tip transition is smooth. The decrease in

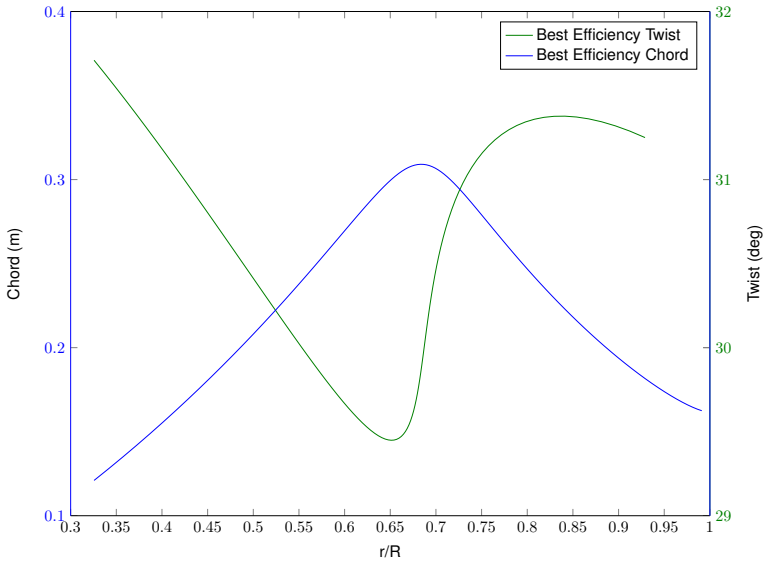

Figure 7.15: Chord and twist distribution for best efficiency.

twist coupled with this transition results in less torque when compared to the baseline case and although the thrust is also diminished, the torque reduction is of higher proportions than the thrust and therefore the efficiency is higher.

Chord, Twist and Curvature In the optimization with the combination of all design variables, it was expected that the combined effect would produce the best results. However, it was observed that by coupling the curvature with the twist and chord, the noise improvement brought by the latter combination was diminished, being the final result a reduction to 57.85 dB(A). The resulting chord and twist distribution will not be presented, due to fact that it is similar to the one shown in figure 7.14, proving the negative impact the curvature has when combined with chord and twist changes.

Summary of the Results

A summary of all the presented optimization results is shown in table 7.3, where it can be seen that the solution involving the change of the chord and twist simultaneously produces the best overall results. It presents the minimum noise, with 57.61 dB(A), which equals a 4.1% reduction, the maximum efficiency, for an increase of 5.3% to 27.5% and the best trade-off, if the criteria is the minimum ratio between the noise and efficiency.

Design Variable	OASPL (dB(A))	Efficiency (%)	OASPL + Efficiency
Chord	58.42	26.1	58.25/26.4
Twist	59.25	24.5	59.79/24.5
Chord+Twist	57.61	27.5	59.33/27.9
Curvature	60.03	-	-
Chord+Twist+Curvature	57.85	-	-

Table 7.3: Summary of the optimization results for the baseline fan.

7.3.2 Improved Fan

After optimizing the baseline fan, the fan with the best noise results from Chapter 6, which is the 500 mm diameter and 6 blade fan, was also subjected to the optimization process. Since all of the process was followed exactly like in the baseline fan optimization, only a summary of the obtained results is presented in table 7.4. For reference, the noise and efficiency baseline values for this fan are 52.3 dB(A) and 1.7%, respectively. The low efficiency value is explained in Chapter 6.

Design Variable	OASPL (dB(A))	Efficiency (%)	OASPL + Efficiency
Chord	50.08	2.2	50.56/1.7
Twist	51.78	1.9	51.75/1.7
Chord+Twist	49.64	4.1	51.15/2.6
Curvature	52.19	-	-
Chord+Twist+Curvature	49.60	-	-

Table 7.4: Summary of the optimization results for the 500 mm diameter/6 blades fan.

Similarly to the baseline fan optimization, the combination of design variables, chord and twist, produced the best overall results, with a decrease of 5.2% in the noise for the minimum OASPL case, an increase of 2.4% in efficiency in the maximum efficiency case and with the best trade-off solution.

In figure 7.16, the radial distribution of noise for the baseline fan and the two optimized fans is presented. In each image, the frontal view of the fan is shown, being the hub depicted by the white circle in the center. The azimuthal angles are shown outside the outer circle, with the fan radius scale being set up along the circle radius. The noise reduction towards the optimized improved fan can be seen by the difference in scales in each figure. It is visible in the baseline and optimized improved fan that there is an annular strip before the tip which produces the maximum noise. This can be explained by the slow change in chord between the maximum chord and the tip, which does not compensate for the increase in the effective velocity due to radius increase and therefore the produced noise is higher. However, in the tip, there is a sudden decrease in the chord, which explains the lower noise levels relatively to the neighboring area.

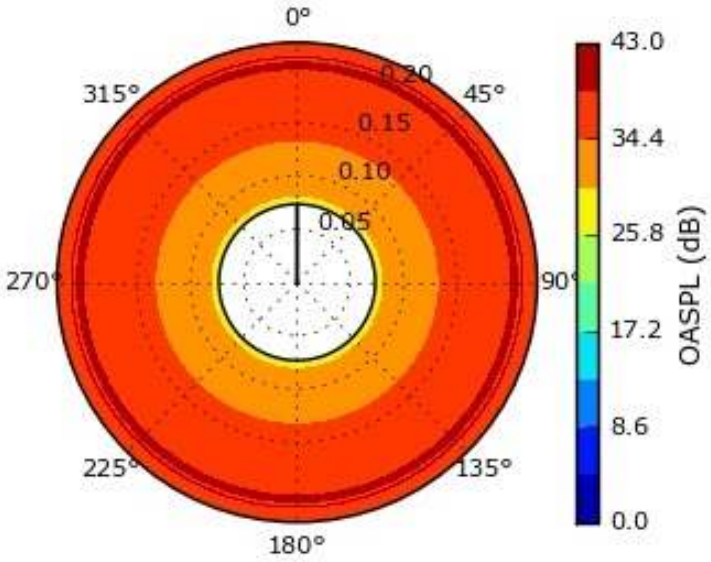

(a) Baseline fan

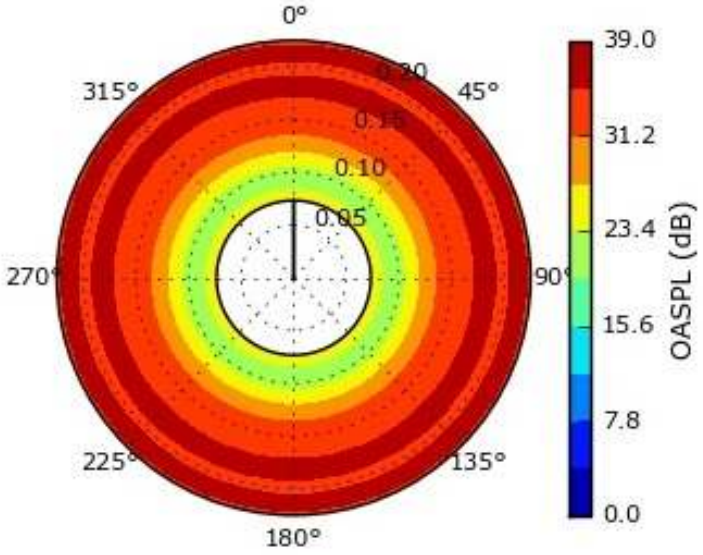

(b) Optimized baseline fan

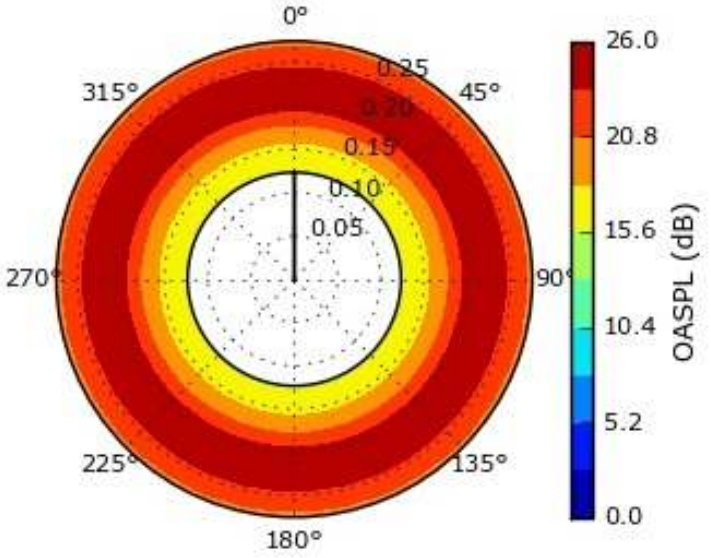

(c) Optimized improved fan

Figure 7.16: Overall sound pressure level across the rotor for different optimization cases.

Chapter 8

Conclusions

In this chapter, the main achievements of this work and some remarks regarding the future work that can be done in improving the aeroacoustic prediction and framework are presented.

8.1 Achievements

In the developed work, a custom wind turbine aerodynamic and aeroacoustic prediction code was successfully adapted for axial flow fans, by adding functionalities specific of these types of fans, while maintaining the original features. These adaptations were also validated against experimental data of a known axial fan.

An existing fan geometrical model of a world leading air conditioning manufacturer was parameterized and introduced into the aeroacoustic tool, using Bézier curves to describe the chord and twist distributions and to define more efficiently the cross sectional airfoil shapes. A curve fitting algorithm was used to effectively describe each airfoil shape with a minimum number of control points. This approach is flexible, since some of typical fan airfoil shape were successfully fitted with Bézier curves.

Using the capabilities of the developed aeroacoustic framework, the air conditioning fan was aerodynamically and aeroacoustically characterized, being defined the baseline noise values of the fan. A parametric study was conducted, where the impact of the fan diameter and blade number on the produced noise was assessed. From this study, it was concluded that an increase in both diameter and blade number results in a noise reduction up to 16.5%. Regarding the efficiency, the diameter increase improves it, while the increase in blade number has a severe negative impact in the aerodynamic performance, reaching values as low as 1.7%.

The aeroacoustic code was successfully integrated into an optimization framework, which allows for optimal solutions to be found for various optimization problems. The blade chord, twist and curvature were optimized in single and multi-objective optimization problems in order to find the minimum noise, maximum efficiency and trade-off solutions. The optimization algorithm was applied to two fans: the baseline fan and the fan which produced less noise from the parametric study. In the baseline fan, a maximum reduction of 4.1% in OASPL and a maximum increase of 5.3% in efficiency was achieved,

while in the second fan, the OASPL was reduced by 5.2% and the efficiency increased 2.4%. In both cases, the combination of design variables which produce these results is the blade chord and twist.

When comparing the new fan with the baseline fan, a total reduction of 17.5% in the OASPL is obtained, but at a cost of decreasing the efficiency by 18.1%. Given the conclusions obtained in this work, the most realistic approach in obtaining the best trade-off solution would be to increase the diameter to 550 mm, maintain the number of blades and change the chord and twist to reach an optimal solution.

With computational advances, the emphasis on improving the efficiency of the preliminary design stage of most engineering projects has increased. This is why this tool has value because it allows to analyze and optimize, with little computational effort, any axial fan preliminary design in order to improve its performance to the maximum possible extent.

8.2 Future Work

One of the major issues found in this work was the adaptability of XFOIL to airfoils that are not typical or common in literature, like the NACA or Eppler airfoils. The airfoil sections found in the studied fans had originally uncommon geometries, with abrupt changes in the curvature and very blunt trailing edges, which brought some difficulties in the boundary layer analysis and the airfoils polar definition. To overcome this challenge, the airfoil geometries had to be refined locally in order for the pressure distribution simulations in XFOIL to be well behaved. In the future, a more robust two dimensional aerodynamic prediction code could be implemented, either from commercial options or custom built, along with an algorithm with the purpose to refine any airfoil geometry. This would increase the flexibility and adaptability to any blade and airfoil geometry.

Regarding the code itself, the BEM method could be replaced with a more rigorous aerodynamic prediction code, such as vortex wake model or an unsteady implementation of BEM. Also, a structural prediction model could be added to the code, which would allow for aerodynamic, aeroacoustic and structural optimization in a preliminary design stage of axial fans, therefore increasing the potential value of the framework.

On a computational level, the optimization algorithms could be improved or changed to faster, more efficient algorithms, in order to reduce the time spent in each optimization. The use of parallel processing could be introduced in the code to reduce the CPU-time required for each optimization, allowing the implementation of more complex models and an higher number of optimization problems with more design variables.

Bibliography

[1] L. Day and I. McNeil. *Biographical Dictionary of the History of Technology*. Routledge, 1998. ISBN 9781134650200.

[2] *The New Book of Knowledge*. 1997.

[3] M. Khattar. Air conditioner fan speed controller for comfort and dehumidification. Technical Report FSEC-FS-31-85, Florida Solar Energy Center, University of Central Florida.

[4] M. Isaac; D. P. van Vuuren. Modeling global residential sector energy demand for heating and air conditioning in the context of climate change. *Energy Policy*, (37):507–521, 2009. doi:10.1016/j.enpol.2008.09.051.

[5] M. Sivak. Potential energy demand for cooling in the 50 largest metropolitan areas of the world: Implications for developing countries. *Energy Policy*, (37):1382–1384, 2009. doi:10.1016/j.enpol.2008.11.031.

[6] B. Berglund; P. Hassmén. Sources and effects of low-frequency noise. *Acoustical Society of America*, 99(5):2985–3002, May 1996.

[7] Ministério do Ambiente do Ordenamento do Território e do Desenvolvimento Regional. Decreto-lei nº 9/2007. DR 12, Série I de 2007-01-17, January 2007.

[8] NYC Environmental Protection. A guide to New York City's noise code, June 2014.

[9] Canada Occupational Safety and Health Regulations. Canada labour code, part ii, 1985. Section 7.4(1)(b).

[10] F. Lau. Elementos de aeroacústica. Class notes, Instituto Superior Técnico, 2013.

[11] J. N. Denenberg and J. M. Charry. *Energy Savings Through the Use of Active Noise Cancellation*. The Guide To The Energy Policy Act of 1992. Fairmont Press, 1992.

[12] M. H. B. A. Rasid. Noise source identification of split unit air conditioner system. Master's thesis, Faculty of Mechanical Engineering, Universiti Malaysia Pahang, November 2008.

[13] J. Pan, M.H. Sun, B. S. Walsh, K. D. Do, P O'Neill., and J. Ranasinghe. Analysis and reduction of blade passing noise of the entecho mupod. *Acoustics Australia*, 38(1):7–12, April 2010.

[14] T. von Kármán. *Aerodynamics*. McGraw-Hill, 1963. ISBN 9780070676022.

[15] T. F. Brooks; D. S. Pope; M. A. Marcolini. Airfoil self-noise and prediction. Technical report, National Aeronautics and Space Administration, 1989.

[16] M. V. Lowson. Assessment and prediction of wind turbine noise. Technical report, Flow Solutions Ltd., 1993.

[17] T. Carolus; M. Schneider. Review of noise prediction methods for axial flow fans. In *The 29th International Congress and Exhibition on Noise Control Engineering*, August 2000.

[18] C. L. Morfey; H. K. Tanna. Sound radiation from a point force in circular motion. *Journal of Sound and Vibration*, 15:325–351, 1971.

[19] T. F. Brooks; T. H. Hodgson. Trailing edge noise prediction from measured surface pressures. *Journal of Sound and Vibration*, 78(1):69–117, September 1981.

[20] J. E. Ffowcs Williams; L. H. Hall. Aerodynamic sound generation by turbulent flow in the vicinity of a scattering half plane. *Journal of Fluid Mechanics*, 40:657–670, March 1970.

[21] T. Carolus; M. Schneider; H. Reese. Axial flow fan broad-band noise and prediction. *Journal of Sound and Vibration*, 300:50–70, July 2007.

[22] L. Bommes; J. Fricke; R. Grundmann. *Ventilatoren*, pages 352–377. Vulkan Verlag, 2. auflage edition, 2003.

[23] I. J. Sharland. Sources of noise in axial flow fans. *Journal of Sound and Vibration*, 1(3):302–322, 1964.

[24] W. L. Keith; D. A. Hurdis; B. M. Abraham. A comparison of the turbulent wall-pressure spectra. *Journal of Fluids Engineering*, (114):338–347, 1992.

[25] R. K. Amiet. Acoustic radiation from an airfoil in a turbulent stream. *Journal of Sound and Vibration*, 41(4):407–420, 1975.

[26] M. Drela. Xfoil: An analysis and design system for low reynolds number airfoils. Technical report, MIT Dept. of Aeronautics and Astronautics, 1989.

[27] B. O. G. Montgomerie; A. J. Brand; J. Bosschers; R. P. J. O. M. van Rooij. Three-dimensional effects in stall. Technical report, Energy Research Center of the Netherlands, 1997.

[28] M. Drela; M. Giles. Viscous-inviscid analysis of transonic and low reynolds number airfoils. *AIAA Journal*, 25(10):1347–1355, 1987.

[29] B. O. G. Montgomerie; A. J. Brand; J. Bosschers; R. P. J. O. M. van Rooij. Integral solution of compressible turbulent boundary layers using improved velocity profiles. Technical report, DTIC Document, 1978.

[30] T. Burton; D. Sharpe; N. Jenkins; E. Bossanyi. *Aerodynamics of Wind Turbines*. John Wiley & Sons, 2001. ISBN 9780471489979.

[31] M. O. L. Hansen. *Aerodynamics of Wind Turbines*. Taylor & Francis, 2012. ISBN 9781844074389.

[32] H. Glauert. Airplane propellers. In *Aerodynamic Theory*, pages 169–360. Springer Berlin Heidelberg, 1935.

[33] A. B. Phillips; S. R. Turnock; M. Furlong. Evaluation of manoeuvring coefficients of a self-propelled ship using blade element momentum propeller model coupled to a reynolds averaged navier stokes flow solver. *Journal of Ocean Engineering*, 36(15-16):1217–1225, November 2009. doi:10.1016/j.oceaneng.2009.07.019.

[34] E. Benini. Significance of blade element theory in performance prediction of marine propellers. *Journal of Ocean Engineering*, 31:957–974, 2004.

[35] L. Prandtl. Tragflügeltheorie. *Göttinger Klassiker der Strömungsmechanik*, (3), 1918.

[36] L. Prandtl. Schraubenpropeller mit geringstem energieverlust - mit einem zusatz von l.prandtl. *Göttinger Klassiker der Strömungsmechanik*, (3):89–92, 1919.

[37] S. S. Rodrigues. Aeroacoustic optimization of wind turbine blades. Master's thesis, Instituto Superior Técnico, November 2012.

[38] D. M. Beazley. Swig: An easy to use tool for integrating scripting languages with C and C++. *Proceedings of the 4th conference on USENIX Tcl/Tk Workshop*, 4:15–15, 1996.

[39] N. P. Salunke; Juned Ahamad R. A.; S. A. Channiwala. Airfoil parameterization techniques: A review. *American Journal of Mechanical Engineering*, 2(4):99–102, August 2014. doi: 10.12691/ajme-2-4-1.

[40] A. Sóbester; T. Barrett. The quest for a truly parsimonious airfoil parameterization scheme. *American Institute of Aeronautics and Astronautics*.

[41] N. Chen; H. Zhang; Y. Xu; W. Huang. Blade parameterization and aerodynamic design optimization for a 3d transonic compressor rotor. *Journal of Thermal Science*, 16(2):105–114, March 2007. doi:10.1007/s11630-007-0105-3.

[42] N. Chen; H. Zhang; Y. Xu; W. Huang. Geometry effects on aerodynamics performance of a low aspect ratio turbine nozzle. *Journal of Thermal Science*, 13(4), October 2004.

[43] N. Chen; H. Zhang; Y. Xu; W. Huang. Study on aerodynamic design optimization of turbomachinery blades. *Journal of Thermal Science*, 14(4), August 2005.

[44] R. W. Derksen; T. Rogalsky. Bezier-PARSEC: An optimized aerofoil parameterization for design. *Advances in Engineering Software*, 41:923–930, June 2010.

[45] T. A. Pastva. Bézier curve fitting. Master's thesis, Naval Postgraduate School, Monterey, California, September 1998.

[46] A. Marta. Multidisciplinary Design Optimization of Aircrafts. Class notes, Instituto Superior Técnico, 2014.

[47] R. T. Marler; J. S. Arora. Survey of multi-objective optimization methods for engineering. *Structures and Multidisciplinary Optimization*, 26:369–395, 2004. DOI: 10.1007/s00158-003-0368-6.

[48] K. Deb; A. Pratap; S. Agarwal; T. Meyarivan. A fast and elitist multiobjective genetic algorithm: Nsga-ii. *IEEE Transactions on Evolutionary Computation*, 6(2):182–197, 2002.

[49] L. Wang; T. Wang; Y. Luo. Improved non-dominated sorting genetic algorithm (nsga)-ii in multi-objective optimization studies of wind turbine blades. *Applied Mathematics and Mechanics*, 32(6): 739–748, 2011.

[50] R. E. Perez; P. W. Jansen; J. R. R. A. Martins. pyopt: A python-based object-oriented framework for nonlinear constrained optimization. *Structures and Multidisciplinary Optimization*, 45(1):101–118, 2012. doi: 10.1007/s00158-011-0666-3.

[51] P. Moriarty; P. Migliore. Semi-empirical aeroacoustic noise prediction code for wind turbines. Technical Report NREL/TP-500-34478, National Renewable Energy Laboratory, December 2003.

Appendix A

Noise Prediction Models Equations

In this appendix, all of the equations that complete the models presented in chapter 2 are here defined, as in [15].

A.1 TEB-VS

The spectral function G_2 and all the required variables are defined as:

$$(G_2)_{\Psi=14^\circ} = \begin{cases} m\eta + k & (\eta < \eta_0) \\ 2.5\sqrt{1-(\eta/\mu)^2} - 2.5 & (\eta_0 \leq \eta < 0) \\ \sqrt{1.5625 - 1194.99\eta^2} - 1.25 & (0 \leq \eta < 0.03616) \\ -155.543\eta + 4.375 & (0.03616 \leq \eta) \end{cases} \tag{A.1}$$

$$\eta = \log\left(St'''/St'''_{peak}\right) \tag{A.2}$$

$$\mu = \begin{cases} 0.1221 & (h/\delta^*_{avg} < 0.25) \\ -0.2175\,(h/\delta^*_{avg}) + 0.1755 & (0.25 \leq h/\delta^*_{avg} < 0.62) \\ -0.0308\,(h/\delta^*_{avg}) + 0.0596 & (0.62 \leq h/\delta^*_{avg} < 1.15) \\ 0.0242 & (h/\delta^*_{avg} \geq 1.15) \end{cases} \tag{A.3}$$

$$m = \begin{cases} 0 & (h/\delta^*_{avg} \leq 0.02) \\ 68.724\,(h/\delta^*_{avg}) - 1.35 & (0.02 < h/\delta^*_{avg} \leq 0.5) \\ 308.475\,(h/\delta^*_{avg}) - 121.23 & (0.5 < h/\delta^*_{avg} \leq 0.62) \\ 224.811\,(h/\delta^*_{avg}) - 69.35 & (0.62 < h/\delta^*_{avg} \leq 1.15) \\ 1583.28\,(h/\delta^*_{avg}) - 1631.59 & (1.15 < h/\delta^*_{avg} < 1.2) \\ 268.344 & (h/\delta^*_{avg} > 1.2) \end{cases} \tag{A.4}$$

$$\eta_0 = -\sqrt{\frac{m^2\mu^4}{6.25 + m^2\mu^2}} \tag{A.5}$$

$$k = 2.5\sqrt{1 - \left(\frac{\eta_0}{\mu}\right)^2} - 2.5 - m\eta_0 \tag{A.6}$$

The spectrum function $(G_2)_{\Psi=0^\circ}$ is obtained by computing equations (A.1) through (A.6) whilst replacing (h/δ^*_{avg}) by $(h/\delta^*_{avg})'$ where

$$\left(\frac{h}{\delta^*_{avg}}\right)' = 6.724\left(\frac{h}{\delta^*_{avg}}\right)^2 - 4.019\left(\frac{h}{\delta^*_{avg}}\right) + 1.107 \tag{A.7}$$

A.2 LBL-VS

The spectral shape function G_3 is defined in terms of the ratio between the Strouhal number and its peak,

$$G_3(e) = \begin{cases} 39.8\log(e) - 11.12 & (e \leq 0.5974) \\ 98.409\log(e) + 2 & (0.5974 < e \leq 0.8545) \\ -5.076 + \sqrt{2.484 - 506.25[\log(e)]^2} & (0.8545 < e \leq 1.17) \\ -98.409\log(e) + 2 & (1.17 < e \leq 1.674) \\ -39.8\log(e) - 11.12 & (e > 1.674) \end{cases} \tag{A.8}$$

where $e = St'/St'_{peak}$. The peak scaled level shape curve G_4 is a function of the Reynolds number and it is defined by

$$G_4(e) = \begin{cases} 77.852\log(d) + 15.328 & (d \leq 0.3237) \\ 65.188\log(d) + 9.125 & (0.3237 < d \leq 0.5689) \\ -114.052[\log(d)]^2 & (0.5689 < d \leq 1.7579) \\ -65.188\log(d) + 9.125 & (1.7579 < d \leq 3.0889) \\ -77.852\log(d) + 15.328 & (d > 3.0889) \end{cases} \tag{A.9}$$

where $d = {}^{R_c}/_{(R_c)_0}$ and the reference Reynolds number is

$$(R_c)_0 = \begin{cases} 10^{0.215\alpha_* + 4.978} & (\alpha_* \leq 3) \\ 10^{0.12\alpha_* + 5.263} & (\alpha_* > 3) \end{cases} \tag{A.10}$$

The shape function G_5 is dependent of the angle of attack α_*

$$G_5(\alpha_*) = 171.04 - 3.03\alpha_* \tag{A.11}$$

A.3 TBL-TE

The spectral shape function A is defined as

$$A(a) = A_{min}(a) + A_R(a_0)[A_{max}(a) - A_{min}(a)] \tag{A.12}$$

where

$$A_{min}(a) = \begin{cases} \sqrt{67.552 - 886.788a^2} - 8.219 & (a < 0.204) \\ -32.665a + 3.981 & (0.204 \leq a \leq 0.244) \\ -142.795a^3 + 103.656a^2 - 57.757a + 6.006 & (a > 0.244) \end{cases} \tag{A.13}$$

$$A_{max}(a) = \begin{cases} \sqrt{67.552 - 886.788a^2} - 8.219 & (a < 0.13) \\ -15.901a + 1.098 & (0.13 \leq a \leq 0.321) \\ -4.669a^3 + 3.491a^2 - 16.699a + 1.149 & (a > 0.321) \end{cases} \tag{A.14}$$

and

$$A_r(a_0) = \frac{-20 - A_{min}(a_0)}{A_{max}(a_0) - A_{min}(a_0)} \tag{A.15}$$

The variables a and a_0 are defined as

$$a = |\log({}^{St}/_{St_{peak}})| \tag{A.16}$$

and

$$a_0(R_c) = \begin{cases} 0.57 & (R_c < 9.52 \times 10^4) \\ (-9.57 \times 10^{-13})(R_c - 8.57 \times 10^5)^2 + 1.13 & (9.52 \times 10^4 \leq R_c \leq 8.57 \times 10^5) \\ 1.13 & (R_c > 8.57 \times 10^5) \end{cases} \tag{A.17}$$

In the same molds as A, the spectral shape function B is defined as

$$B(b) = B_{min}(b) + B_R(b_0)[B_{max}(b) - B_{min}(b)] \tag{A.18}$$

where

$$B_{min}(b) = \begin{cases} \sqrt{16.888 - 886.788b^2} - 4.109 & (b < 0.13) \\ -83.607b + 8.138 & (0.13 \leq b \leq 0.145) \\ -817.81b^3 + 355.21b^2 - 135.024b + 10.619 & (a > 0.145) \end{cases} \tag{A.19}$$

$$B_{max}(b) = \begin{cases} \sqrt{16.888 - 886.788b^2} - 4.109 & (b < 0.1) \\ -31.33b + 1.854 & (0.1 \leq b \leq 0.187) \\ -80.541b^3 + 44.174b^2 - 39.381b + 2.344 & (b > 0.187) \end{cases} \tag{A.20}$$

and

$$B_r(b_0) = \frac{-20 - B_{min}(b_0)}{B_{max}(b_0) - B_{min}(b_0)} \tag{A.21}$$

The variables b and b_0 are defined as

$$a = |\log(St/St_2)| \tag{A.22}$$

and

$$b_0(R_c) = \begin{cases} 0.3 & (R_c < 9.52 \times 10^4) \\ (-4.48 \times 10^{-13})(R_c - 8.57 \times 10^5)^2 + 0.56 & (9.52 \times 10^4 \leq R_c \leq 8.57 \times 10^5) \\ 0.56 & (R_c > 8.57 \times 10^5) \end{cases} \tag{A.23}$$

The amplitude function K_1 is defined as

$$K_1 = \begin{cases} -4.31\log(R_c) + 156.3 & (R_c < 2.47 \times 10^5) \\ -9\log(R_c) + 181.6 & (2.47 \times 10^5 \leq R_c \leq 8 \times 10^5) \\ 128.5 & (R_c > 8 \times 10^5) \end{cases} \tag{A.24}$$

and the correction for the pressure side contribution in nonzero angles of attack cases ΔK_1 is given by

$$\Delta K_1 = \begin{cases} \alpha_*[1.43\log(R_{\delta_p^*})] - 5.29 & (R_{\delta_p^*} \leq 5000) \\ 0 & (R_{\delta_p^*} > 5000) \end{cases} \tag{A.25}$$

The amplitude function K_2 is defined as

$$K_2 = K_1 + \begin{cases} -1000 & (\alpha_* < \gamma_0 - \gamma) \\ \sqrt{\beta^2 - (\beta/\gamma)^2(\alpha_* - \gamma_0)^2} + \beta_0 & (\gamma_0 - \gamma \leq \alpha_* \leq \gamma_0 + \gamma) \\ -12 & (\alpha_* > \gamma_0 + \gamma) \end{cases} \tag{A.26}$$

with

$$\begin{aligned} \gamma &= 27.094M + 3.31 \\ \gamma_0 &= 23.43M + 4.561 \\ \beta &= 72.65M + 10.74 \\ \beta_0 &= -34.19M - 13.82 \end{aligned} \tag{A.27}$$

Appendix B

Coordinate Systems

In this appendix, the transformation matrices between the various coordinate systems used in the aeroacoustic tool are defined.

Systems 1 and 2 are identical, being that the only difference between them is the position of their origins, such that the distance between them equals the height of the location of the fan.

Since the shaft is assumed to be stiff, the transformation between system 2 and 3, given by transformation matrix $\mathbf{a_{23}}$, consists only in a rotation about the z-axis with a magnitude of θ_{rot}, which is the angle of rotation of the shaft:

$$\mathbf{a_{23}} = \begin{bmatrix} \cos\theta_{rot} & \sin\theta_{rot} & 0 \\ -\sin\theta_{rot} & \cos\theta_{rot} & 0 \\ 0 & 0 & 1 \end{bmatrix} \tag{B.1}$$

System 4 has its origin in the hub of the rotor, and it is rotated about system 3 x-axis with the angle θ_{twist}, to account for the twist along the blade:

$$\mathbf{a_{34}} = \begin{bmatrix} 1 & 0 & 0 \\ 0 & \cos\theta_{twist} & \sin\theta_{twist} \\ 0 & -\sin\theta_{twist} & \cos\theta_{twist} \end{bmatrix} \tag{B.2}$$

Therefore, to transform a vector in system 4 to system 1, the following transformation is applied, along with the origin translations:

$$\mathbf{r_1} = \mathbf{a_{32}} \cdot \mathbf{a_{43}} \cdot \mathbf{r_5} \tag{B.3}$$

or:

$$\mathbf{r_1} = \mathbf{a_{23}}^{\mathbf{T}} \cdot \mathbf{a_{43}}^{\mathbf{T}} \cdot \mathbf{r_5} \tag{B.4}$$